The generation and breaking of internal waves on a lutocline in the Ems estuary (Germany), their hydro-acoustic detectability and their contribution to sediment transport dynamics

Dissertation
zur Erlangung des Doktorgrades
der Mathematisch-Naturwissenschaftlichen Fakultät
der Christian-Albrechts Universität
zu Kiel

vorgelegt von
Philipp Held

Kiel, 2013

Erste Gutachterin:	Prof. Dr. Kerstin Schrottke
Zweiter Gutachter:	Prof. Dr. Karl Statteger

Tag der mündlichen Prüfung:	05.02.2014
Zum Druck genehmigt:	05.02.2014

gez. (Prof. Dr. Wolfgang J. Duschl), Dekan

Ich versichere an Eides statt, dass:

1. Ich bis zum heutigen Tage weder an der Christian-Albrechts-Universität zu Kiel noch an einer anderen Hochschule ein Promotionsverfahren endgültig nicht bestanden habe oder mich in einem entsprechenden Verfahren befinde oder befunden habe.

2. Ich die Inanspruchnahme fremder Hilfen aufgeführt habe, sowie, dass ich die wörtlich oder inhaltlich aus anderen Quellen entnommenen Stellen als solche gekennzeichnet habe.

3. Die Arbeit unter Einhaltung der Regeln guter wissenschaftlicher Praxis der Deutschen Forschungsgemeinschaft entstanden ist.

Kiel, Unterschrift:

Abstract

River estuaries are of great importance for social and ecological purposes and underlie strongly anthropogenic influences. Estuaries provide sheltered areas for the construction of harbours and the adjacent rivers are inland transport routes. Fluid Mud layers (a mixture of water, sand, silt and organic matter) are potentially problematic for the operation of such facilities and for the maintenance of navigational channel. Such layers are often topmost bounded by a strong concentration gradient of suspended particles, the so-called lutocline, which also is a strong density gradient. Vertical exchange and resuspension of sediment are hindered because of this strong density stratification.
This thesis deals with internal waves propagating along this interface and their influence on the local sediment transport dynamics in the German Ems estuary. Additionally, the operability of oceanographic instruments in highly turbid waters, which is the case in the Ems estuary, is verified.
Laboratory studies showed, that a determination of salinity via the electrical conductivity doesn't provide useful results in highly turbid waters. More accurate salinity values will be obtainable if salinity is measured in water samples after the suspended particle matter has been settled. Measurements of the sound velocity under laboratory conditions and in the field showed that the velocity of sound in water depends on, amongst others, the suspended matter concentration. However, different linear correlation coefficients are derived from laboratory and field measurements. It is likely, that the correlation coefficients depends on the structure, the density and the size of the suspended particles. Therefore, it is not possible to calculate the velocity of sound in sediment suspension, because not all of the required parameters are known. Two different mathematical approaches provide different values for the sound velocity, which do not match the measurements. Further investigations on the influence of suspended particulate matter on the sound velocity and on their acoustic properties are hence suggested. The velocity of sound is, amongst others, required to simulate the acoustic reflectivity of lutoclines with a weak-scattering model. Such simulations show a general increase of the echo strength of the lutocline with decreasing sound frequency. The depth of the most prominent echo of an extended lutocline fluctuates by several decimeter, depending on the sound frequency. This frequency dependence of the strongest echo must be taken into account when comparing records of a lutocline, recorded with different sound frequencies.
The Ems estuary has an extend turbidity maximum zone with high suspended particulate matter concentration, in which a strong lutocline develops during high water slacks.

The fluid mud and the overlaying water layer are differently accelerated by the tides. This causes the upper water body to flow faster than the lower fluid mud layer during ebb tide. In contrary, both layers move with a similar speed during flood tide. The different current velocities lead to shear stress and the appearance of Kelvin-Helmholtz instabilities during ebb tide. These instabilities are further stimulated by rising ebb current, causing waves to arise on the lutocline. This internal waves reach their maximal heights of up to 2 m, after the ebb current has peaked and already decelerates. Internal wave breaking also occurs during that time. Fluid mud will be resuspended and mixed into the upper water body by breaking internal waves. Wave breaking during ebb tide supports seaward sediment transports because the upper water layer flows faster than the fluid mud layer. In contrast to this, only a few waves break during flood tide. Additionally, both layers have similar flow speeds during flood tide, therefore sediment, which was upward mixed by breaking waves, settles at the same position in the co-moving reference frame. Thus, internal wave breaking has no influence on the horizontal sediment transport during flood tide.
Internal wave breaking leads hence to an erosion of the fluid mud layer, which is manifested by an increase of the lutocline width and by a decline of the lutocline during ebb tide. Additionally, wave breaking causes a decrease of the vertical stratification, shown by the Brunt-Väisälä frequency which reaches its minimum during the second half of the ebb tide.

Zusammenfassung

Flussästuare sind von großer sozialer und wirtschaftlicher Bedeutung und daher starken anthropogenen Einflüssen unterworfen. Ästuare bieten geschützte Bereiche für den Bau von Seehäfen und die angrenzenden Flüsse stellen zudem geeignete Transportwege ins Binnenland dar. Fluid Mud Schichten (eine Mischung aus Wasser, Sand, Schlick und organischem Material) können zu einem Problem für den Betrieb solcher Anlagen und für die Unterhaltung von Fahrwassern werden. Solche Schichten werden meist nach oben hin durch einen starken Schwebstoff-Konzentrationsgradienten, die Lutokline, welche gleichzeitig ein starker Dichtegradient ist, begrenzt. Aufgrund der starken Dichteschichtung werden vertikale Austauschprozesse und Resuspendierung von Sediment unterdrückt.
Diese Arbeit beschäftigt sich mit internen Wellen die sich entlang einer solchen Grenzfläche ausbreiten, und deren Einfluss auf die lokalen Sedimenttransportdynamiken im deutschen Emsästuar. Zusätzlich wird die Einsatzfähigkeit von ozeanographischen Mess-

instrumenten in Gewässern mit hoher Schwebstoffkonzentration, wie sie in der Ems vorherrschen, untersucht.
Laboruntersuchungen zeigen, dass eine Bestimmung der Salinität über die elektrische Leitfähigkeit keine brauchbaren Ergebnisse in hochkonzentrierten Wasserschichten liefert. Genauere Salinitätswerte von solchen Schichten erhält man, wenn man die elektrische Leitfähigkeit in Wasserproben misst, nachdem sich die Schwebstoffe abgesetzt haben. Messungen der Schallgeschwindigkeit im Labor und im Feld zeigen, dass auch die Schallgeschwindigkeit von der Schwebstoffkonzentration abhängt. Allerdings werden bei den Messungen im Labor und im Feld jeweils andere Werte für den linearen Proportionalitätskoeffizienten ermittelt. Wahrscheinlich hängt dieser vom inneren Aufbau, der Dichte und Größe der Flocken der suspendierten Partikel ab. Nicht alle dieser Parameter sind bekannt, daher ist es nicht möglich die Schallgeschwindigkeit in Sedimentsuspensionen theoretisch zu berechnen. Zwei unterschiedliche mathematische Ansätze ergeben jeweils andere Werte die nicht mit den Messungen übereinstimmen. Hier werden weitere Untersuchungen über die Beeinflussung der Schallgeschwindigkeit von Wasser durch Schwebstoffe und über die akustischen Eigenschaften der Schwebstoffe empfohlen. Die Schallgeschwindigkeit wird unter anderem dazu benötigt um die akustische Reflexion von Lutoklinen mit einem "weak-scattering" Modell zu berechnen. Solche Simulationen zeigen eine grundsätzliche Zunahme der Echostärke der Lutokline mit abnehmender Schallfrequenz. Die Tiefe der stärksten Reflexion einer ausgedehnten Lutokline schwankt in Abhängigkeit der Schallfrequenz um mehrere Dezimeter. Diese Frequenzabhängigkeit der Tiefe des stärksten Reflektors muss berücksichtigt werden, wenn Aufnahmen mit unterschiedlicher Frequenz der Lutokline miteinander verglichen werden sollen.
Das Emsästuar besitzt eine ausgedehnte Trübungszone mit hohem Schwebstoffgehalt, in welcher sich eine deutliche Lutokline während Hochwasser ausbildet. Fluid Mud und der darüber liegende Wasserkörper werden durch die Gezeiten unterschiedlich stark beschleunigt. Dies führt dazu, dass während Ebbstrom der obere Wasserkörper schneller fließt als der darunterliegende Fluid Mud. Bei Flut hingegen bewegen sich beide Schichten nahezu gleich schnell. Aufgrund der unterschiedlichen Strömungsgeschwindigkeiten kommt es zu Reibung zwischen den beiden Schichten und zur Entstehung von Kelvin-Helmholtz Instabilitäten während Ebbe. Diese Instabilitäten werden durch zunehmenden Ebbstrom weiter angeregt so dass sich Wellen auf der Lutokline bilden. Diese internen Wellen erreichen ihre maximale Höhe von bis zu 2 m nachdem der Ebbstrom seine maximale Strömungsgeschwindigkeit überschritten hat und wieder abnimmt. Zu dieser Zeit kommt es auch zum Wellenbrechen. Durch die brechenden internen Wellen

wird Fluid Mud resuspendiert und in den oberen Wasserkörper gemischt. Da die obere Wasserschicht schneller flussabwärts strömt als der Fluid Mud, trägt das Wellenbrechen während Ebbe zum seewärts gerichteten Sedimenttransport bei. Dem hingegen brechen nur wenige Wellen bei Flut. Zudem bewegen sich nun beide Schichten gleich schnell, durch das Wellenbrechen aufgewirbelter Fluid Mud sinkt dadurch an der gleichen Stelle im mitbewegten Bezugssystem ab. Das Brechen interner Wellen hat somit keinen Einfluss auf den horizontalen Sedimenttransport während Flut.
Internes Wellenbrechen führt somit zu einer Erosion der Fluid Mud Schicht, das zeigt sich durch eine Zunahme der Lutoklinenbreite und einem Absinken der Lutokline während Ebbe. Zusätzlich verursacht Wellenbrechen eine Abnahme der vertikalen Schichtungsstabilität, was durch ein Minimum der Brunt-Väisälä Frequenz während der zweiten Ebbhälfte angezeigt wird.

Contents

1 Introduction

1.1 General introduction

Estuaries are funnel-shaped inlets of coasts, which are of great importance for social, economical and ecological purposes. In opposition to bights, estuaries have adjacent discharging rivers leading to complex salinity distributions (Dean and Dalrymple, 2001). The inflowing seawater is situated underneath the river discharge due to its greater density. The salt water intrusion near the bottom is sometimes also referred to as salt wedge. This stratification depends on the hydrodynamic conditions, i.e. the river discharge and tidal range, and provides an opportunity for the classification of estuaries. In areas with low tidal range (i.e. < 2 m) and low river discharge, estuaries are highly stratified with a prominent salt wedge (Brown et al., 2006). On the opposite, they are partial-mixed or well-mixed at coasts with moderate or high tidal range (i.e. > 2 m; Brown et al., 2006). More than 50 % of the worlds population lives within a range of 200 km of the coasts, using them for recreational and economical purposes. Estuaries provide shielded and calm areas for the construction of harbours and the adjacent rivers can be used as inland transport routes (Prandle, 2009). Transhipment in harbours and sea transport are of great importance for the world trade. Germany, as one of the largest exporting nations in the world, shipped 63 % of its exports to non-EU countries by sea in 2011 (Statistisches Bundesamt (Federal Statistical Office), Wiesbaden). The largest and most important harbours in Germany, e.g. Hamburg and Bremerhaven, and shipping yards are located in estuaries. This position has not only advantages, but also disadvantages: Sediment input is a big problem because silting causes a decrease of the local water depth.

Sediments can enter the estuary either from the adjacent river or from the sea side. Rivers can transport high amounts of sediment, depending on the geological settings of their catchment areas. The increasing salinity in the estuary leads to changed chemical conditions for the suspended particles. An increasing amount of positive ions in the water counteracts with the electrical repulsion between the particles, normally having a

weak negative surface charge-distribution (Huang et al., 2012), and enables the aggregation of the transported minerals and primary particles (Thill et al., 2001). Thus a region of enhanced aggregation and flocculation, the turbidity maximum zone (TMZ), essentially occurs at the upper end of the salt intrusion (Kirby, 1988). Van der Waal forces and organic slime are hereby responsible for the cohesion of the particles. Flocculation refers to a difficult interaction between growth and breakup, involving the processes of Brownian motion, different settling velocities, turbulence and shear stress (Papenmeier et al., 2014). Although the resulting flocs have lower densities than the primary particles, their settling velocity is higher, increasing the downward mass flux (Manning and Dyer, 2007; Eisma, 1986). The upward flux of water hindered when a certain suspended particle matter (SPM) concentration is exceeded and the settling velocity decreases (Hayter and Mehta, 1986). Such conditions are described as hindered settling conditions and lead to the occurrence of mobile, highly concentrated bottom layers. These layers are a mixture of water, silt, clay, fine sand and organic matter, and are referred to as fluid mud if their SPM concentration exceeds 10 g l^{-1} (Manning et al., 2010; McAnally et al., 2007; Kineke and Sternberg, 1995; Ross and Mehta, 1989; Kirby, 1988). Fluid mud is often differentiated from the upper less turbid water layer by a strong SPM gradient, also denoted as lutocline.

Besides rivers, muddy coasts in the vicinity of estuaries are another sediment source. Breaking surface waves erode beaches and the fine eroded material is subsequently transported by near bed flows into estuaries (Baldock et al., 2010). Non-breaking surface waves can also destabilise the bed and liquefy the consolidated sediments, forming up fluid mud layers (Mehta, 1989; Maa and Mehta, 1987). Therefore, fluid mud layers occur frequently in highly energetic coastal waters and estuaries.

Resuspension of fluid mud and vertical exchange is hindered by the strong density gradient of the lutolcine. However, even in strongly stratified systems, vertical mixing is enabled through turbulent movements (Bouruet-Aubertot et al., 2001). A possible source for turbulences within the water column as well as at interfaces are breaking waves. Waves are usually not linked to mass transport or mixing since the fluid particles move on closed orbitals. This situation changes during wave breaking. Internal wave (IW) breaking is known to be the main source for turbulence and diapycnal mixing in the oceans (Leichter et al., 2005). Turbulences induced by breaking IWs are also important for diapycnal mixing in estuaries. New et al. (1987, 1986) observed strong salinity variations near the surface linked to IW breaking in the Tee estuary (England). Breaking surface waves are, amongst others, important for the exchange of CO_2 between the

atmosphere and the oceans and are, hence important for the understanding of global warming (Banner and Peregrine, 1993).
In a stable water column fluid mud will consolidate, resulting in the siltation of navigational channels and harbours. Therefore, a continuous monitoring combined with repeated dredging is necessary to maintain navigational depths. These operations are expensive and time consuming. Dredging also means a severe environmental impact, because it destroys the local benthic flora and fauna. The dredged material has to be dumped at sites, where it shifts the equilibrium between accretion and erosion (Dean and Dalrymple, 2001). Consequently, it could be eroded again and transported by the local hydro-dynamic conditions at the dumping side. Additionally, the presence of fluid mud layers can cause problems in detecting the real nautical bottom, since sound waves can be reflected by strong lutoclines (Kirby, 2013).
The improved knowledge of fluid mud dynamics led to a better and more effective management of dredging activities at the port of Emden. Fluid mud is not completely removed from the harbour to maintain an equilibrium between the harbour and the river (Wurpts, 2005). This concept reduces the amount of dredging activities and saves about 8.5 million Euro per year (Kirby, 2013).

1.2 Motivation

A better understanding of the complex sediment dynamics in estuarine systems could help to increase the economic usage of estuaries and to reduce environmental impacts caused by dredging. This thesis investigates mainly IWs propagating on a lutocline, and their role for estuarine sediment dynamics. Therefore, it was investigated how IWs are generated in the estuary, which hydro-dynamic conditions lead to IW breaking and last but not least the influence of IW breaking on the sediment transport. Several mechanism of IW generation are known, whereas the processes leading to wave breaking are not yet fully understood, even though there has been a lot of effort in the last century (Oh et al., 2005; Banner and Peregrine, 1993). Similar to surface waves IWs can break at sloping beaches, causing an erosion of the bed (Nagashima, 1971). However, IWs must not necessarily break to enable sediment transport. Offshore currents induced by near-inertial waves (IWs which the phase velocity is perpendicular to the group velocity) are associated with sediment transports in the Adriatic Sea (Urgeles et al., 2011). To sum it up, the influence of IWs on the sediment transport is still poorly documented (Pomar et al., 2012). This thesis aims to improve the knowledge of processes leading to

IW breaking and to estimate the contribution of IW breaking to sediment transport. Since most of the used devices and methods were developed for clear water usage, special attention on the quality of the measurements must be paid when employing them in turbid waters. Therefore, validation studies have been carried out to ensure the usability and the performance of the devices in turbid waters, such as fluid mud layers. Such validation studies were carried out for salinity measurements and for the hydro-acoustic detectability of lutoclines.

Salinity is one of the most important water parameters in oceanography and coastal geosciences, because of its significant influence on the water density and hence stratification. Density stratification is also a key factor for the mathematical description of IWs (see section 5). Some observations described in literature indicate that salinity measurements could be influenced by SPM. A lower salinity in fluid mud than in the upper water column was repeatedly measured in the Amazon during the AmasSeds project (Kineke et al., 1996; Kineke and Sternberg, 1995). Additionally, Traykovski et al. (2000) observed low conductivities in the fluid mud layers on the Eel River continental shelf (California, USA). However, investigations dealing with this subject have not been published yet. Hence, it was investigated how much SPM influences conductivity-based salinity measurements in the frame of a laboratory study.

The influence of SPM on the sound propagation and, hence on the detectability of sediment induced interfaces within the water column was also investigated. A better understanding of this would enhance the interpretation of hydro-acoustic records of turbid water layers. Additionally, a mathematical relation between the sound velocity and SPM concentrations would yield the possibility to determine the latter by measuring the first one. Such an approach for the determination of SPM concentrations would have advantages over conventional methods. It could deliver SPM concentrations continuously over the water column in realtime, whereas values derived from water samples are only available at discrete depth and after laboratory analyses. Optical backscatter methods are disadvantageous, since they can become saturated in highly turbid layers (see e.g. Traykovski et al., 2000). Another frequently used method is to derive SPM concentration from the backscatter strength measured with an acoustic Doppler current profiler (ADCP). This method also delivers continuous measurements over the water column, but requires a calibration with water samples (Hoitink and Hoekstra, 2005). Ultrasonic methods are used for concentration measurements in two-phase suspensions in industry (Langlois et al., 2011).

Acoustic reflections occur at boundaries between regions differing in acoustic impedance,

which is proportional to the density and sound velocity. Echos created by sediment induced stratifications have been repeatedly recognised since the installation of echo-sounders on board ships in the 1930's (Kirby, 2013). A contribution of SPM to the water density is obvious, whereas its influence on the sound velocity is not as clear. One possibility to estimate the sound velocity in turbid suspension is to use Urick's equation (Eq. 4.12). Satisfying results were yielded when using this approach to model the seismogram of an air-gun experiment in the Farore-Shetland Channel (Vsemirnova et al., 2012). However, this approach is only valid for long wave lengths and small particle sizes.
Another approach is to regard the scattering of the sound wave at each particle. Such a consideration is especially necessary for great particles compared to the wave length. Mobley et al. (1999) achieved good agreements between their sound velocity measurements in polystyrene water suspensions and values calculated with this approach. Both described approaches indicate that the sound velocity in suspensions depends not only on the particle concentration, but also on the particle size distribution. The concentrations and particle size distributions of natural turbid water layers are very diverse. Therefore, both approaches have been used to calculate the sound velocity in natural sediment suspensions and the results were compared with measurements recorded in the laboratory and in the field. Additionally, the sound velocity profiles recorded during the Ems survey 2012 were used to simulate the reflectivity of natural lutoclines with a weak-scattering model published by Ross and Lavery (2012).

This thesis is arranged as follows: Background information on IWs and sound propagation in fluids are given in chapter 2. The used methods informations are described in chapter 3. The results of the investigations are split in two parts. First, the findings of the validation studies are presented in chapter 4. This chapter contains the manuscript "Influence of suspended particulate matter on salinity measurements", which is submitted to *Continental Shelf Research*. Second, the results of the studies concerning the IWs in the Ems estuary are presented in chapter 5, containing the paper "Generation and evolution of high-frequency internal waves in the Ems estuary, Germany" which have already been published in *Journal of Sea Research*. Each result chapter summarizes and concludes the respective findings.

1.3 Geological settings of the study site

The study area is the German Ems estuary, which is an example for a highly turbid and strongly anthropogenically influenced estuary. It is located at the coastal-plain of the Southern North Sea, close to the border between Germany and the Netherlands. The lower part downstream of Pogum is funnel-shaped with the adjoining Dollart, a tidal basin, whereas the upper part between Herbrum and Pogum is channelized. The tidal influenced area stretches from the island Borkum to the weir at Herbrum, and has a length of approximately 100 km (Spingat and Oumeraci, 2000). A moderate tidal range and a mean river-discharge between 25 and 380 m^3s^{-1} lead to a partially mixed estuary (van Leussen, 1999). However, the river-discharge underlies strong seasonal variations (de Jonge, 1992) and the current velocities are accordingly variable and highly site-specific. They generally decrease slightly downstream and reach a maximum values of 1 m s^{-1} during high river discharge (Spingat and Oumeraci, 2000).
The estuary is flood dominated meaning that the current velocities are higher during flood tide than during ebb tide. However, the ebb phases are, in contrast, longer than the flood phases. The tidal wave increases while it propagates upward the estuary from a height of 2.25 m near the island of Borkum to a height of 3.1 m at the port of Emden (de Jonge, 1992; van Leussen, 1999).
The salinity normally decreases from approximately 30 near Borkum to 1 near Leer (de Jonge, 1992). Brackish conditions can found upstream of Leer only during low river-discharge and low water slacks (Spingat and Oumeraci, 2000).
The Ems estuary has an extended TMZ stretching over 60 km (de Kreeke et al., 1997). Its suspension loads can reach several tens kg m^{-3}, forming a 1 - 2 m thick fluid mud layer (Talke et al., 2009; Schrottke et al., 2006). An analysis of bacteria showed that the origin of fluid mud in the port of Emden is the upper Ems river (Wurpts, 2005). The impact of mankind on the estuary is obviously: The deepening of the navigational channel led to an increase of the tidal range by 1.5 m (Talke and de Swart, 2006), shifting the TMZ upstream (Becker, 2011). Additionally, de Jonge (1983) observed an increase of SPM concentrations over the recent decades. The sustained navigable depth currently amounts to 5.7 m at low-water spring (Schuchardt et al., 2007).

2 Background information

Some background information about IWs, sound propagation in fluids and the hydroacoustic reflectivity of interfaces within the water column are presented in this chapter.

2.1 Internal waves

In general, waves are propagating periodic disturbances or moving oscillations. Several different kinds of waves exist, distinguishable by their type of oscillation (i.e. longitudinal or transversal waves), their supporting medium (if there is any) or their restoring forces.
IWs are waves propagating through the interior of fluids. They might propagate throughout the complete fluid or be bound at interfaces between fluid layers differing in density. The most prominent waves are water surface waves that are familiar to everyone ever standing on a beach and looking out to the sea. They are a special case of interfacial waves.
A fluid parcel is normally situated in a position where its buoyancy counteracts its weight. If it is moved from its equilibrium position it will be forced back by imbalance between buoyancy and weight. It does not stop moving when it reaches its equilibrium positions again because of its inertia. The fluid parcel starts to oscillate. The maximum frequency, with which the fluid parcel can oscillate, is the corresponding buoyancy frequency or Brunt-Väisälä-frequency N. Its square is proportional to the background density gradient:

$$N^2 = -\frac{g}{\rho}\frac{d\rho}{dz} \tag{2.1}$$

where ρ is the density, z is the vertical coordinate and g is the acceleration due to gravity. If such an oscillation moves away from its origin it will be termed as IW.
The local density distribution strongly influences the oscillation behaviour of disturbances, as it can be seen from Eq. 2.1. Depending on the ratio of the exciter to the buoyancy frequency, IWs propagate at specific angles to the horizontal (LeBlond, 2002).

Inhomogeneities of the stratification like pycnoclines (interfaces between layers differing in density) can guide waves. Disturbances on or in the vicinity of a pycnocline propagate along it. At a sharp pycnocline, the local density gradient and thus the buoyancy frequency go toward infinity. Consequently, there is no theoretical upper limit for the frequency of IWs propagating along a pycnocline. Such waves are characterized by a dispersion relation, describing the relation between wave period and wave length or between frequency and energy. The dispersion relation incompressible fluids can be derived from the Laplace equation:

$$\nabla^2\Phi = 0 \tag{2.2}$$

where Φ is the velocity potential, and the Bernoulli equation:

$$\rho\partial_t\Phi + \frac{1}{2}\rho u^2 + p + \rho g z = 0 \tag{2.3}$$

where u is the current velocity and p is the pressure. In order to solve this problem suitable boundary conditions have to be specified. For finite layer thicknesses, the linear dispersion relation for interfacial waves reads:

$$\omega^2 = gk\frac{\rho_2 - \rho_1}{\rho_2\coth(kd_2) - \rho_1\coth(kd_1)} \tag{2.4}$$

where ω is the angular frequency, k is the wave number ($k = \frac{2\pi}{\lambda}$), ρ_1, ρ_2, d_1 and d_2 are the densities and thicknesses of the upper and lower layer, respectively. For a detailed derivation see Apel (1987).
The water surface can be regarded as interface between an infinite extended layer of negligible density (air) and a dense layer of finite thickness (water). Therefore, setting ρ_1 to zero and d_1 to infinity yields the dispersion relation of surface gravity waves:

$$\omega^2 = gk\tanh(kd) \tag{2.5}$$

here d is the water depth. This illustrates that surface waves are a special case of IWs. Several processes are known to be able to initiate wave generation in fluids. Interactions between currents and topographic obstacles are the main reasons for the IW generation in coastal waters as well as in the deeper ocean. Such obstacles could be continental shelf edges (e.g D'Asaro et al., 2007; Huthnance, 1989), straits (e.g. Brandt et al., 1996) and deep ocean ridges (e.g Konyaev et al., 1995). Air streams over mountains are also the main generation process for IWs in the atmosphere (Nastrom and Fritts, 1992).

Topographic induced IWs are not continuous waves but solitons consisting of a small number of crests. They can be bound as stationary lee-waves behind the obstacles, as long as the current velocity is higher than their phase speed (Wang, 2006). IWs can also be generated by resonant flow conditions or decelerating river plumes (e.g Baines, 1984). Both processes are usually also controlled by the topography. Besides changes of the current velocity, variations of the flow cross section can lead to resonant flow conditions. If a fast flowing river encounters a basin, the current will be decelerated. Other sources for IW generation are for example wind (e.g Vilibić et al., 2004; Kantha, 1979) and surface waves (e.g Maxeiner and Dalrymple, 2011; Traykovski et al., 2000).
Systems consisting of two layers of different flow speed are subject to instabilities. Shear stress between both layers enables the onset of Kelvin-Helmholtz instabilities. The generation of wind waves is an example for this mechanism. The air flow over the water surface creates shear stress and small ripple waves occur (Miles, 1957). The stability of horizontal sheared currents can be analysed by the Richardson number, which denotes the ratio of the potential to the kinetic energy:

$$\mathrm{Ri} = \frac{g}{\rho} \frac{d\rho/dz}{(du/dz)^2} \tag{2.6}$$

where u is the horizontal current velocity. A necessary (but not sufficient) criteria for the onset of Kelvin-Helmholtz-instabilities is a Richardson number below 0.25 (Apel, 1987).
Under suitable conditions, instabilities can be further stimulated and develop into waves. Instabilities lead to disturbances and wave-like undulations on the boundary layer. The disturbances in turn deform the streamlines, leading to a complex pressure distribution around the undulations. These pressure patterns causing the further growth of the undulations (Otten, 2008; Ott, 1996). The relation between streamline density and pressure is described by the Bernoulli effect.
In general, waves are not linked to mass transport or mixing because fluid particles move on closed orbitals, at least in a first order approximation. This changes if waves break. Breaking waves create strong turbulences leading to mixing events. Several criteria have been suggested to describe the circumstances leading to wave breaking. A classical geometrical criterion is the wave steepness:

$$\eta = \frac{H}{\lambda} \tag{2.7}$$

where H is the wave height. Limits for the wave steepness have been gained during laboratory and field measurements and show a strong variance (Oh et al., 2005). The ratio between the crest speed and the trough speed is a kinetic criteria. It is obvious that a wave will collapse if the crest overturns the through. However, even this criterion has not been yet validated by field observations. Some researchers reported on waves with crest velocities higher than the one predicted by the linear dispersion relation (Oh et al., 2005). Oh et al. (2005) suggested that a dynamic criterion, which is defined as the ratio between the surface acceleration and the gravity, is most suitable as breaking criterion. Unfortunately, the necessary parameters for this criterion are difficult to obtain.
The main opinion in literature is that growing instabilities, which are ubiquitous on waves, induce wave breaking in deep water. For example, small capillary waves will be superimposed on greater waves if wind blows. These capillaries could be focused on a certain part of a wave by non-linear wave-wave interaction, and destabilise the wave. Therefore, even small ripple waves can cause a high wave to collapse (Banner and Peregrine, 1993). It is difficult to specify a widely accepted breaking criterion since these instabilities are difficult to handle, especially with respect to IWs. Eiff et al. (2005) found that the stability of orographic lee-waves is given by the vertical Froude-number. For a Froude-number below one, lee-waves become unstable and could break. However, a valid and universally accepted breaking criterion for IWs has not yet been found.
The situation is a little bit easier for wave breaking at beaches, where it is induced by an increasing influence of the bottom. In shallow water, which means that the water depth is less than half the wave length, waves are dispersionless and the wave speed depends only on the water depth (Apel, 1987). A widely accepted breaking criterion for shallow water waves is the ratio of water D depth to wave height H D/H 1.1...1.3 (Peregrine, 1983). Even IWs could break at sloping beaches (Nagashima, 1971).

2.2 Hydro-acoustics and sound propagation in fluids

Electromagnetic waves, e.g. light, have no big propagation range in water because of the electrical conductivity of water. Sound is much less attenuated, especially at low frequencies (Apel, 1987). Therefore, hydro-acoustic methods are mainly used for most remote sensing purposes in oceanography, even though they have a reasonably lower resolution than optical methods.
In general, sound is a pressure wave and propagates through elastic media. The local density is temporally changed by the passing pressure wave. Sound propagates as pure

longitudinal wave in fluids, whereas it can have transversal components in solids or at boundaries.
In fluids, the sound velocity c is a function of the density ρ and the bulk modulus K:

$$c = \sqrt{\frac{K}{\rho}} \tag{2.8}$$

The density and the bulk modulus of sea water depend on temperature, salinity and pressure. These three parameters are easier to obtain than the density or the bulk modulus. Therefore, a lot of effort has been undertaken to deduce an empirical equation for the sound velocity in dependence of the temperature, salinity and pressure (depth) in the first part of the last century. The result is nowadays used by default to compute the sound velocity from CTD measurements and is given in the International Oceanographic Tables of the UNESCO.
In 1937, it was observed that the propagation of a sound wave is affected by a layer of warm water. This discovery led to a new research field: The acoustical oceanography (Bjørnø, 2003). In general, the propagation of a sound wave will be affected if it enters a region of different acoustical impedance. The acoustic impedance Z denotes the resistance a sound wave experiences by the medium, it reads:

$$Z = \rho \cdot c \tag{2.9}$$

Water masses are generated by different rates of solar heating, evaporation, precipitation and river discharge. The amount of SPM also influences the density and the sound velocity (latter will be shown in this thesis) and therefore the acoustical impedance. If two water masses have the same acoustical impedance the direction of a sound wave will not be altered if it passes the interface between them. Otherwise, reflections and refractions occur. The acoustic reflectivity of an interface, which is defined as the ratio of the incident to the reflected sound pressure, can hence also be expressed in terms of the acoustic impedance:

$$R = \frac{Z_2 - Z_1}{Z_1 + Z_2} \tag{2.10}$$

where Z_1 and Z_2 are the acoustic impedance of the first and second water mass, respectively. Eq. 2.10 is valid for sound scattering at infinitely sharp interfaces. However, natural interfaces are not infinitely sharp, but have a transition zone because of diffusion processes. Penrose and Beer (1981) showed that an initially sharp interface broadens by

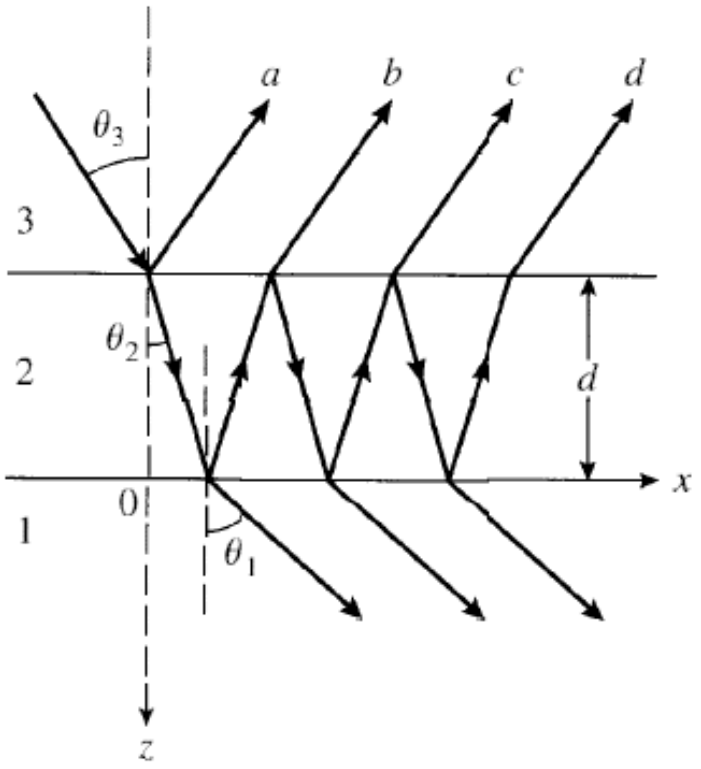

Figure 2.1: Multiple Reflections of a sound wave in a three layer system, adopted from Brekhovskikh and Lysanov (2003)

diffusion and hence its echo becomes too weak for detection within several hours. In order to simulate the reflections at natural interfaces, they have to be divided into several sublayers of constant sound velocity and density. Reflections occur at both sides of a sublayer (Fig. 2.1, resulting in different path length for both reflected waves. Therefore, the reflections of each sublayer have to be coherently added to take into account interference effects between the part waves. An example calculation for a three layer system is given in Brekhovskikh and Lysanov (2003). Based on this multilayer approach, Ross and Lavery (2012) developed a weak-scattering model for oceanographic pycnoclines.

3 Methods

In this chapter the most important deployed devices and their underlying physical processes will be briefly described.

3.1 SES - Sediment Echo-Sounder

Interfaces within the water column, especially the lutoclines, were recorded with a high resolution parametric echo sounder of type 'SES-2000® standard' of Innomar Technology GmbH (Rostock, Germany). This device has a primary frequency of about 100 kHz and a adjustable secondary frequency. The vertical resolution was up to 6 cm (Wunderlich et al., 2005) and the accuracy for depth measurement was 0.02 + 0.02 % of the water depth (Wunderlich and Müller, 2003). The secondary frequency was adjusted to be 12 kHz. A Seatex MRU-6 motion sensor was used to correct for heave, roll and pitch movements.
The depth of the lutocline was extracted from the records with the SES software ISE 2.9 and exported as xyz-ASCII files. These ASCII files were further processed, e.g. in form of spectral analyses, significant wave heights and fluid mud layer thicknesses, with self-developed C++-routines.
The advantages of parametric systems are to generate low frequent signals with narrow beam widths and without significant side lobes (Wunderlich et al., 2005). These benefits combined with a high band width yields the possibility to detect weak acoustical impedance variations even at low signal-to-noise (SNR) ratios (Wunderlich and Müller, 2003). The ability to detect internal acoustical layering with a the frequency channel of this system was already proven by Schrottke et al. (2006).
In general, the directivity of an emitted signal depends on the ratio between the signal wave length and the transducer dimensions. Long wave lengths, corresponding to low frequencies require huge transducers to generate a narrow beam signal with weak side lobes, at least if the signals will be directly generated by a linear system. Nonlinear systems use the parametric effect to generate a low frequency signal by simultaneous

transmitting at least two slightly different high frequencies (primary frequencies) at very high sound pressures (Kozaczka et al., 2009; Wunderlich et al., 2005). An upper limit for the intensity of the primary frequencies is set by the onset of cavitation. Both primary sound waves interact nonlinear with each other in front of the transducer. The sound velocity superimposes with the sound particle velocity, caused by the interaction of high sound pressures and medium density. This in turn, leads to a distortion and interaction of the primary waves and new frequencies arise (Fig. 3.1). The new frequencies correspond to the harmonics, the sum and the difference of the primary frequencies (Wunderlich et al., 2005). The latter one is also referred to as secondary frequency. The secondary frequencies are low and have nonetheless directivities similar to that of the high primary frequency. Thus, it is possible to transmit a low frequent narrow beam signal without side lobes with compact transducers.

3.2 Flow speed measurements

Flow velocities in water column were recorded with an RDI-Teledyne™ 1200 kHz Workhorse ADCP (Acoustic Doppler Current Profiler). This device delivered mean flow speeds for 2.33 s long measuring intervals with a standard deviation of 0.129 m s^{-1}. The cell size for the measurements was adjusted to be 0.25 m and the blancing zone was 0.5 m at 1200 kHz. The ADCP was installed downward-looking in a rigid frame on the side of the research vessel 'RV Senckenberg' during the measurements.
Hydro-acoustic current measurements based on the Doppler-shift, expired by a transmitted sound wave when it is reflected by moving scatterers. The essential assumption for this technique is that the scatters move on average with the mean current velocity (Gordon, 1996). Scatterers can be plankton or small dissolved particles, zooplankton with a size in the order of 1 mm are the dominant scatterers in the oceans Gordon (1996).
The Doppler effect describes the change of a wave frequency if the source, the observer or both of them move relatively to each other. If the source and the observer move towards each other, the wave length will be compressed, i.e. the observer measures a higher frequency than the source transmits. The opposite, an expanded wave length, will be the case if source and observer move away from each other. Only the relative radial movement components contribute to the Doppler effect, tangential velocity components have no influence. For sound waves, the cases of a moving source and a moving observer have to be separately considered, because sound requires a supporting medium

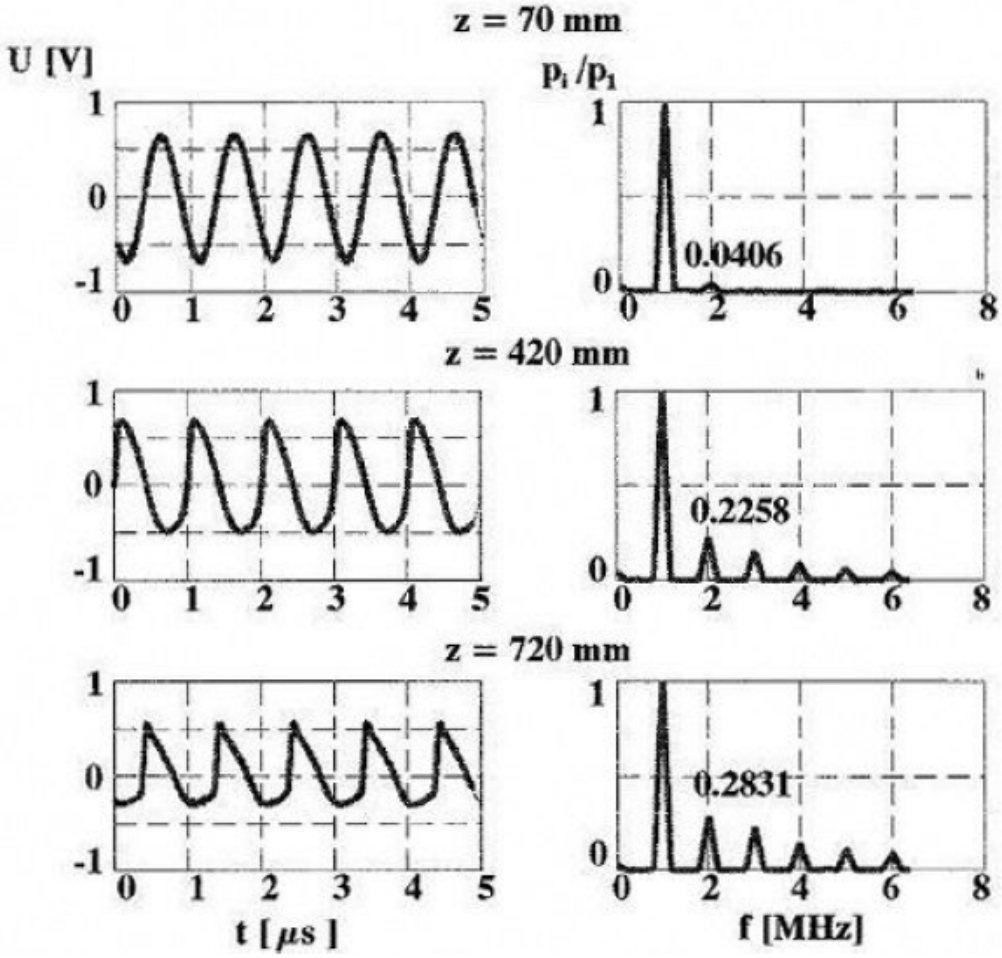

Figure 3.1: The shape and spectrum of nonlinear generated sound beams for different distances from the source, adopted from Kozaczka et al. (2009).

(Demtröder, 2013). In the first case, the source is moving while the observer is at rest, the observer then measures a frequency f_R of:

$$f_R = f_S \cdot \frac{1}{1 - \frac{v}{c}} \tag{3.1}$$

where f_S is the frequency of the emitted signal, c is the phase speed of the sound wave and v is the velocity of the source in direction to the receiver. v is positive for an approaching and negative for a distancing source. In the other case, the source is at rest and the moving observer measures a frequency of:

$$f_R = f_S \cdot (1 + \frac{v}{c}). \tag{3.2}$$

Again, v will be positive if the source moves towards the receiver and otherwise be negative.
When considering the echo of a moving scatterer, both cases have to be combined. The scatterer is a moving receiver in the reference system of the transducer. Accordingly, Eq. 3.2 must be applied to determine the frequency of the sound signal, approaching the scatterer. When backscattering the signal, the scatterer behaves like a moving source in the reference system of the transducer. The frequency of the received echo f_{echo} than becomes (Demtröder, 2013):

$$f_{\text{echo}} = f_0 \cdot \frac{1 + \frac{v}{c}}{1 - \frac{v}{c}} \tag{3.3}$$

where f_0 is the frequency of the transmitted sound puls.
Since only the radial velocity components contribute to the Doppler effect, it requires at least three differently orientated sound beams to determine a 3 dimensional current velocity vector. The used workhorse ADCP has a total of four beams, which are cross-shaped arranged with two in a line (Fig. 3.2). Assuming that the horizontal flow conditions are homogeneous (each beam measures the flow field at a different position), one horizontal and the vertical component can be retrieved by trigonometrical calculations from one beam-pair (Fig. 3.2).

3.3 Salinity measurements

Profiling salinity measurements in the Ems estuary were carried out with a CTD (Conductivity Temperature and Depth - Probe) of type CTD90 by Sea & Sun technology. The conductivity sensor of this CTD had 7 platinum coated electrodes which were sym-

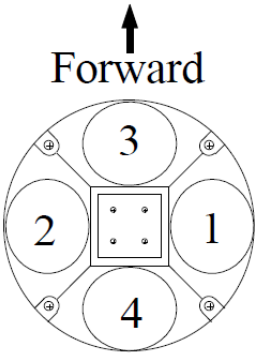

Figure 3.2: Schematic view of thex arrangement of the four transducers of a workhorse ADCP, adopted from Gordon (1996).

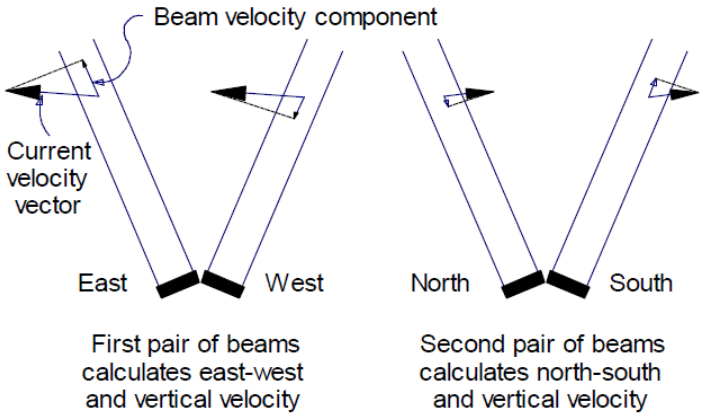

Figure 3.3: Determination of the vertical and one horizontal velocity component from a sound beam pair, adopted from Gordon (1996).

metrically arranged in a quartz cylinder. The accuracy of the conductivity measurements was 20 µS cm^{-}1. Salinity values were calculated from the conductivity measurements in terms of the Practical Salinity Scale (PSS-78) by the operating software SST-SDA (Standard Data Acquisition Program).
For laboratory studies (chapter 4.1) as well as for the determination of the salinity of water samples, a multimeter of type CON3310 by WTW® was used. This multimeter was connected with a conductivity sensor of type TETRACON 325, which was a four electrode sensor with graphite electrodes. Salinity values were also displayed in terms of the practical salinity unit. It had a salinity accuracy of 0.1 as stated by the manufacturer.
The electrical conductivity is proportional to the current and inverse proportional to the voltage. Salinometers determine the conductivity by measuring the electrical current flow between two immersed electrodes while the voltage between them is adjusted or vice versa. The polarisation of the electrical field between the electrodes is continuously altered, to avoid a shielding of the electrodes by an agglomeration of ions. The water volume between the immersed electrodes can be considered as electrical conductor. The conductivity of a electrical conductor is given by (Stöcker, 2000):

$$\kappa = \frac{I}{U} \cdot \frac{l}{A} \tag{3.4}$$

where I is the current, U is the voltage, l is the length and A is the cross section of the conductor. The last term in Eq. 3.4 only depends on the cell geometry and is determined by a cell calibration. Modern salinometers use more than two electrodes to achieve more accurate conductivity measurements and to reduce disturbances by surrounding electrical fields.
Salinity specifies the amount of dissolved ions in water. Different methods were developed in the past to determine salinity, e.g. vaporisation and titration. Nowadays, salinity is determined by the electrical conductivity of water, because this method is more accurate than chlorinity measurements (Gerold, 1963). However, pure water should generally be electrical non-conductive due to the absence of charge carriers. Nevertheless, protons are exchanged between water molecules causing the occurrence of H_3O^+ and OH^- -ions and thus the occurrence of charge carriers:

$$2\mathrm{H_2O} \rightleftharpoons \mathrm{H_3O^+ + OH^-}$$

This process is referred to as the autoprotolyse of water. The chemical reaction equilibria is on the left side meaning that only a few ions are produced by the autoprotolyse. Thus, pure water has a low electrical conductivity. The electrical conductivity of water mainly depends on the amount of dissolved salt ions (Pawlowicz et al., 2011). In order to determine the salinity by the electrical conductivity it is necessary to assume that each water sample with the same conductivity has the same salinity (Millero, 2010). Based on this assumption, an empirical equation was derived, which defines the salinity as the conductivity ratio of a sea water sample to a standard potassium chloride (KCl) solution (UNESCO, 1981). This equation is known as the Practical Salinity Scale (PSS-78). The standard KCl solution has a concentration of 32.4356 g KCl l^{-1} and the same conductivity as standard sea water clearly defined with a salinity of 35 (Pawlowicz, 2010). The relative ion composition in the world oceans is constant which was already assumed by Alexander Marcet about 1820 (Millero et al., 2008). A good and comprehensive review of the development of the PSS-78 is given in Millero (2010).

3.4 Water samples and Suspended Particulate Matter (SPM) concentration

Water samples of different water depths were collect to determine SPM concentration. Therefore, a horizontal water sampler by Hydrobios© with an approximate volume of 2 l was used. An attached fin allowed the sampler to align with the current. The alignment of the sampler minimized the turbulences around the sampler and hence enabled the collection of almost undisturbed water samples. The sampler was connected with a rope, which was tagged every meter and used for the manual operation. After the sampler was positioned at the desired depth, it was closed with a plummet, sliding along the control rope.

The SPM concentration was recorded as dry-weight. Therefore, an aliquot of each water samples was vacuum-filtrated through a glass fibre filter with 1.2 µm pore diameter. The respective aliquot volumes were chosen in dependence on the sample consistencies. The organic content of the water samples was determined by ignition loss. For this, the dried filters were heated in a muffle furnace at 550 °C for 2 hours and weighed again afterwards. The difference in weight before and after ignition corresponded to the organic contents of the samples.

4 Validation studies

The preliminary validation studies are presented in this chapter. The first study dealt with the usability of conductivity sensors to measure salinity in turbid waters. Therefore, the influence of SPM on the conductivity measurements and hence on the obtained salinity values was investigated. The corresponding experiments and results are presented in section 4.1, which is submitted to *Continental Shelf Research*. The second validation study examined the ability of hydro-acoustic devices to detect sediment-induced interfaces within the water column. In the frame of these investigations, the influence of SPM on the sound velocity was of particular interest. This study is presented in section 4.2.

4.1 Influence of suspended particular matter on salinity measurements[1]

P. Held[a], P. Kegler[b] K. Schrottke[a]

[a] Cluster of Excellence "The Future Ocean", Institute of Geosciences at Kiel University, Otto-Hahn-Platz 1, 24118 Kiel, Germany

[b] Mineralogy Department, Institute of Geosciences at Kiel University, Ludewig-Meyn-Str. 10, 24118 Kiel, Germany

4.1.1 Abstract

Salinity is a very important parameter in marine science, normally measured by electrical conductivity. So far no investigations have been accomplished to examine how electrical conductivity, is influenced by Suspended Particulate Matter (SPM). Even though there are hints in literature that SPM can affect salinity measurements significantly.
In this paper is a new laboratory study about the influence of SPM on conductivity based salinity measurements presented. Different sensor types were deployed to investigate the influence of the conductivity sensor design on the observed salinity deviations. The role of clay minerals was additionally analysed. Two natural mud samples of different origins were used to set up various SPM concentrations. The results have shown that high suspended sediment concentrations (of up to 300 g l^{-1}) can distort salinity measurements up to 30 percent. Only 22 percent on average of the observed salinity deviation could be explained by the adsorption of ions by clay minerals. The cell geometry had no verifiable effect.
The observed salinity deviations were caused by a "blinding effect" of the sensor due to the dissolved particles which was proved in a mathematical manner.

Keywords: Electrical conductivity of sea water, conductivity measurements, CTD, fluid mud, flocculation, estuaries

4.1.2 Introduction

Salinity is a common and important parameter for the classification of water masses (Le Menn, 2011) and is essential for the calculation of other water parameters like density and sound velocity. Salinity of sea water has been measured via its electrical conduc-

[1] This article was submitted to Continental Shelf Research

tivity due to it's higher accuracy than with chlorinity measurements after commercial salinometers had become available in the late 1960's (Gerold, 1963). The electrical conductivity of water depends on the amount of dissolved ions (Pawlowicz et al., 2011). Salinity can be calculated in terms of the practical salinity scale, which is defined as the conductivity ratio of a sea water sample to a standard potassium chloride (KCl) solution (UNESCO, 1981). This solution contains 32.4356 g of KCl per litre and has the same conductivity standard sea water has. Standard sea water has per definition a salinity of 35 (Pawlowicz, 2010). A comprehensive review of the development and the history of the practical salinity scale (PSS-78) is given by Millero (2010).

Problems can occur while trying to determine the salinity of water layers with high amounts of suspended particulate matter (SPM). These layers frequently form in energetic coastal areas and estuaries. Those with Suspended Sediment Concentrations (SSC) $>$ 10 g l^{-1} are termed fluid mud in the following. Salinity values in fluid mud seemed to be different from the ones in the water body above, as repeatedly recorded in fluid mud layers on the Amazon shelf during the AmasSeds study (Kineke et al., 1996; Kineke and Sternberg, 1995). Traykovski et al. (2000) also measured low conductivities in fluid mud layers on the Eel River continental shelf (California, USA). Similar observations were made during a survey in the Ems estuary (Germany) in 2008, with lower salinity values in the fluid mud than in the upper water column. The SSC of fluid mud layers in the Ems estuary varied between 23.2 +/- 0.8 g l^{-1} and 88.2 +/- 3.0 g l^{-1} (Held et al., 2013). There are different explanations for the reduced salinity values in fluid mud layers. Based on their observations that in fluid mud salinity is lower and the temperature is higher than in the upper water body, Kineke and Sternberg (1995) assumed that the fluid mud layer was formed somewhere else on the Amazon shelf and was afterwards advected to the position where it was found. Submarine groundwater discharge is another explanation. In this explanation the stratification of heavier seawater on lighter freshwater is supported by suspended sediment.

Water-saturated formations have a lower electrical resistivity than unsaturated ones, as found out by Archie, G. E. (1942). The so-called "Archie's Law" describes the relation between the resistivity of sand when all pores are filled with brine R_0 and the resistivity of brine R_W:

$$R_0 = F R_W \tag{4.1}$$

where F is the formation resistivity factor, which is linked with the porosity of sand via $F = \Theta^{-m}$, where m must be determined experimentally and ranges between 1.2 and 2.0 (Archie, G. E., 1942). Since conductivity is the inverse of the resistivity, Eq. 4.1

can also be applied to calculate the ratio of the conductivity of fluid mud and the conductivity of clear water with the same salinity. Traykovski et al. (2000) used "Archie's Law" to calculate the porosity of fluid mud with the measured salinities in water and fluid mud, but this method yielded implausible results. They assumed that the salinity measurements themselves were influenced by SPM and therefore falsified salinity values were obtained.
So far, no experimental studies to validate and quantify this assumption have been published. Such studies could clarify the reliability of salinity measurements in highly turbid waters and would give a chance to quantify the effect of SPM on CTD (Conductivity temperature and depth probe) measurements.
In this study the influence of SPM on salinity measurements was determined experimentally. For this, salinity and SPM amounts were varied systematically in different experimental runs. The adsorption of ions by clay minerals and its contribution to the observed salinity deviations was additionally investigated.

4.1.3 Methods

In order to determine the influence of SPM on conductivity-based salinity measurements, the differences between real and measured salinity values were recorded in dependence of the SPM concentrations. For this, suspensions of different salinity and SPM concentration were set up in the laboratory. The salinities of the solutions were known, because they were controlled with sodium chloride (NaCl). The SPM concentrations were adjusted with natural mud samples from two different places of origin. Two different sampling locations were chosen to verify any dependency on the mineral composition of the mud. The first mud sample was collected in the main navigation channel of the Ems Estuary (North Sea coast, Germany) in June 2007. The second mud sample was collected in a tideway near the island of Nordstrand (North Frisian Wadden Sea, Germany) in July 2011. The compositions of the mud samples had to be determined before they could have been used to adjust the SPM concentrations of the test solutions.

Salinity measurements

Salinity measurements were performed with a CTD of type CTD90 by Sea & Sun Technology and a multimeter of type CON 3310 by WTW®. The CTD was equipped with a Keller pressure transducer, a temperature sensor consisting of a platinum transistor Pt 100 and a conductivity sensor by ADM. The conductivity sensor had 7 platinum coated

electrodes which were symmetrically arranged in a quartz glass cylinder. The accuracy of measurement was 0.1 % for pressure, 0.005 °C for temperature and 20 µS cm^{-1} for conductivity measurements. Salinity values were computed by the operating software SST-SDA (Standard Data Acquisition Program) in terms of the PSS-78.
The multimeter was connected with a conductivity sensor of type TETRACON 325. It was a four electrode sensor with graphite electrodes. Salinity values were again recorded in terms of PSS-78. An accuracy for salinity measurements of 0.1 was stated by the manufacturer.
Salinity is nowadays determined via the electrical conductivity of water. The electrical conductivity, κ, is the reciprocal value of the specific resistance. It is proportional to the current I and the length l of the conductor and inversely proportional to the voltage U and the cross section A of the conductor, and reads (Stöcker, 2000):

$$\kappa = \frac{I}{U} \cdot \frac{l}{A} \tag{4.2}$$

In a salinometer, the volume between the measuring electrodes corresponds to an electrical conductor. Modern conductivity cells either adjust the voltage between the electrodes while the current gets measured, or they are working in the other way around: the current is adjusted while the voltage drop gets measured. This corresponds to the first part of the equation ($I\ U^{-1}$). The second term $l\ A^{-1}$ is the cell constant, which depends on the cell geometry and is determined during cell calibration.

Data analysis

Data analysis was based on the discrepancy between the adjusted and the measured salinity, which was defined as the difference ΔS_i between the measured salinities of the test solutions $S_{mud,i}$ and of the reference run $S_{ref,i}$. The measured salinity had to be corrected for a potentially remained salinity in the prepared mud samples. The required correction factors were determined in the first salinity measurement of the test solutions, before any NaCl had been added. These salinity values were labelled as $S_{mud,0}$ and than the salinity-difference reads:

$$\Delta S_i = S_{mud,i} - S_{mud,0} - S_{ref,I} \tag{4.3}$$

The relative difference was calculated in percent of the adjusted salinity $S_{ref,i}$:

$$\Delta S_{rel,i} = \frac{|\Delta S_i|}{S_{ref,i}} \cdot 100\% \tag{4.4}$$

Preparation of the mud samples

Although it was tried to keep the mud samples in their natural state, they got desalinated to avoid a salt contamination of the experimental setup. No further modifications were done on the mud samples apart from the desalination. For the desalination, mixtures of mud and distilled water were filled into membrane tubes also used for dialysis. The tube membrane material allows the exchange of dissolved ions and nutrients, triggered by the osmotic effect. The tubes were subsequently transferred into a bath of distilled and continuously renewing flowing water. Consolidation of mud was prevented by shaking the tubes periodically. The tubes were kept in the water bath until the diluted mud reached a salinity of zero. Afterwards, the contents of all tubes with mud from the same origin were mixed together. The mud samples rested for some time, the mud settled down and it was possible to remove the excess water subsequently.

Determination of SPM concentration, organic matter content and mineralogical composition

Three mud sub-samples of 10 ml were dehydrated in a drying chamber at 60 °C for 48 hours to retrieve the mass weight of suspended matter and hence the SPM concentration.
The organic content was recorded as the ignition loss of the sub-samples. For this, they were finely ground in an agate mortar and afterwards heated in a muffle furnace at 550 °C for 6 hours.
The mineralogical composition of the mud samples was determined by XRD (X-Ray Diffraction) analysis (Siemens D5000, Institute for Geosciences, University of Kiel). The measurements were performed from 5° 2 Θ to 80° 2 Θ using a Cu X-ray tube (40 kV, 40 mA) and evaluated using X'Pert HighScore Plus software by PANalytical. The calculation of the mass fraction of the different mineral phases was done using rietveld refinement.

Reference run

Before the experimental runs had been carried out, a reference run was done to check the performance of the CTD and the salinometer in clear NaCl solutions. For this, salinities were measured in solutions, differing in NaCl concentration. The obtained reference values for the salinity were required, because the PSS-78 algorithm was fitted for seawater. Thus, the recorded salinity values wouldn't exactly match the adjusted salinity values in g l^{-1}.

Adjusting of the suspensions

In order to set up the SPM concentration of a test solution, a specific volume of mud was diluted with distilled water to a total volume of 3 l. The required mud volume $V_{mud,i}$ depended on the desired SPM concentration of the test solution and on the SPM concentration of the used mud sample. It amounts to:

$$V_{mud,i} = V_{tot} \cdot \frac{C_{SPM,i}}{C_{SPM,sample}} \tag{4.5}$$

where $C_{SPM,i}$ is the desired SPM concentration of the test suspension, $C_{SPM,sample}$ is the SPM concentration of the mud sample and V_{tot} is the volume of the test suspension, here 3 l. This method was used to produce suspensions with SPM concentrations of 0.5, 1, 5, 10, 25, 50, 75, 100, 150, 200 and 300 g l^{-1} with both gathered mud samples.

Experimental runs

Experimental runs were carried out for all the produced mud suspensions. That caused the SPM concentration to be constant during an experimental run, whereas the salinities were varied by the addition of NaCl. Salinities were adjusted between 0 and 40 g l^{-1} NaCl in steps of 5 g l^{-1}. The measured salinity values were recorded several minutes after an addition of NaCl, to ensure that the salt had been completely dissolved. However, the first salinity values were recorded before any NaCl was added, to check for the rest salinity of the mud.
Particle settling during the experimental runs was hindered by stirring the suspensions with an electrical mixer. The temperature of the suspensions varied between 19 °C and 22 °C during a single experimental run. However, these temperature variations did not affect the determined salinities, because the PSS-78 algorithm already accounts for the temperature influence on the electrical conductivity.

Determination of the adsorption of ions by clay minerals

The adsorption of salt ions caused by clay minerals was investigated in an additional experiment. In this experiment, test solutions with specific concentrations of SPM and NaCl were prepared. SPM concentrations of 1, 10, 25 and 75 g l^{-1} were chosen for these test solutions. Each SPM concentration was set up twice, once with a salinity that represents brackish conditions (10 g l^{-1} NaCl) and once with a salinity that represents marine conditions (35 g l^{-1} NaCl). The salinity was measured in a well-mixed state of the solutions. Then the suspensions were centrifuged to deposit the dissolved sediment. Afterwards salinities were measured a second time in the clear water, above the deposited sediment. The difference between the second recorded salinity and the corresponding reference salinity value corresponds to the adsorbed salt ions.

4.1.4 Results

Composition of the mud samples

The amount of SPM and the organic matter mass (i.e. ignition loss) of the three mud sub-samples are shown in table 4.1 for the mud from the Wadden Sea respectively in table 4.2 for the mud from the Ems estuary. The averaged values and the standard deviations are both declared in the last row.
Inferred from these data, the organic matter content in the Ems estuary was higher than in the Wadden sea, respective to the chosen collective sites. The averaged SPM concentrations of the mud samples (second column, last row in table 4.1 and 4.2) were used to adjust the SPM concentrations of the test solutions and they correspond to the term $C_{SPM,sample}$ in Eq. 4.5.
Based on the XRD measurements, the mud of both sample locations mainly consisted of quartz (68 %), dolomite (13 %) and calcite (6 %). The proportions of clay minerals in both samples were low (less than 10 wt%).

Salinity measurements in NaCl solutions

The results of the reference runs are shown in Fig. 4.1. Although the PSS-78 algorithm was derived to determine the salinity of sea water, the measured salinity values in terms of the practical salinity unit (PSU) almost match with the values of the adjusted NaCl concentrations in g l^{-1} in the context of the measurement accuracy.

Table 4.1: SPM concentration and organic matter content of the three Wadden sea subsamples

Sample ID	**SPM concentration [g l^{-1}]**	**m(organic) [g l^{-1}]**
Wadden1	636	29.07
Wadden2	647	28.57
Wadden3	654	27.00
Average:	646 +/- 5	28.21 +/- 0.62

Table 4.2: SPM concentration and organic matter content of the three Ems estuary subsamples

Sample ID	**SPM concentration [g l^{-1}]**	**m(organic) [g l^{-1}]**
Ems1	539	45.93
Ems2	537	45.88
Ems3	474	40.42
Average:	516 +/- 21	44.08 +/- 1.83

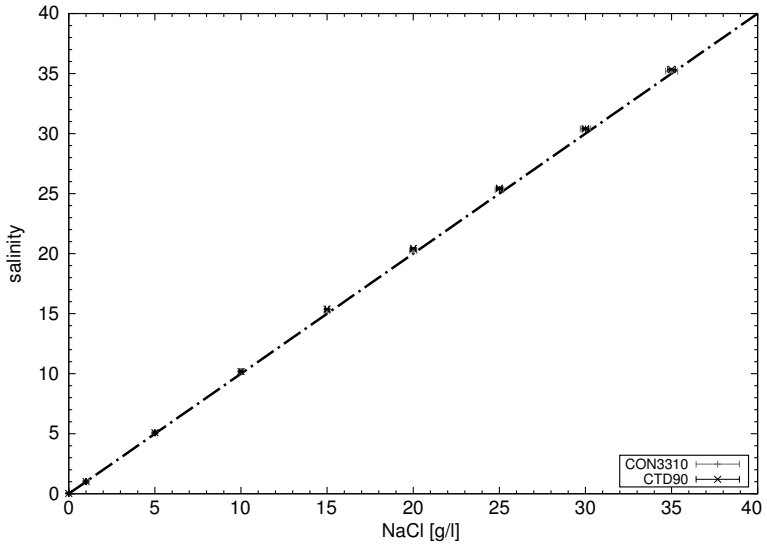

Figure 4.1: Salinity reference values measured with both instruments in NaCl solutions without SPM. The salinity values on the y-axis correspond to the PSU. The horizontal error bars represent the uncertainty of the adjusted NaCl concentrations whereas the vertical error bars represent the measurement uncertainties of the devices.

Deviations of measured salinity in turbid water

The first salinity measurements, i.e. before any NaCl was added to the test solutions are shown in Fig. 4.2. These values were used to correct the salinity differences for a possibly remaining salinity of the mud after the desalination process, and correspond to the term $S_{mud,0}$ in Eq. 4.3. The values indicate that a small amount of salt remained after desalination.

The results of the experiments with mud from Ems estuary are presented in detail in Fig. 4.3.a+c and 4.3.b+d for measurements with the CTD90 model and the CON3310 model, respectively. The results are expressed in differences between the measured salinity in test solutions and the reference salinity values for the same NaCl concentration, calculated with Eq. 4.3. The most apparent result was that the absolute value of the salinity differences generally increased with increasing NaCl concentration, for a given SPM concentration. The differences were positive in the test runs with less than 10 g l^{-1} SPM, i.e. the measured salinities were higher than salinity reference values for the same NaCl concentration. Maximum positive differences were reached in the experimental run with 0.5 g l^{-1} SPM: $\Delta S = +0.35$ for measurements with the CON3310 model and +0.27 for measurements with the CTD90 model. For a SPM concentration of 10 g l^{-1} the differences were very small (Fig. 4.3.a-b). However, the salinity differences in the test runs with these SPM concentrations were within the range of the combined error of measurement uncertainty and uncertainties of adjusted salinity and SPM concentration. The salinity differences became negative with further increasing SPM concentrations, i.e. less salinities were measured in the test solutions than in the reference solution with the same NaCl concentration. The salinity differences reached values of up to -12.60 for 40 g l^{-1} NaCl and a SPM concentration of 300 g l^{-1} (Fig. 4.3.d).
In addition to the salinity differences, relative salinity differences of the experimental runs with mud from the Ems estuary are shown in Fig. 4.4.a and 4.4.b, calculated with Eq. 4.4 for the measurements with the CTD90 model and the CON3310 model, respectively. As seen in these figures, the relative salinity differences were less than 2 % for SPM concentrations of up to 25 g l^{-1}. Again, the relative salinity differences increased with increasing SPM concentrations. They were about 5 % for a SPM concentration of 50 g l^{-1} and increased up to approximately 30 % for an SPM concentration of 300 g l^{-1}. However, the most important and most obvious finding in this form of presentation was the constance of relative salinity difference for NaCl concentrations above 15 g l^{-1} (Fig. 4.4.a-b). Whereas the relative salinity differences increased between 0 and about 15 g

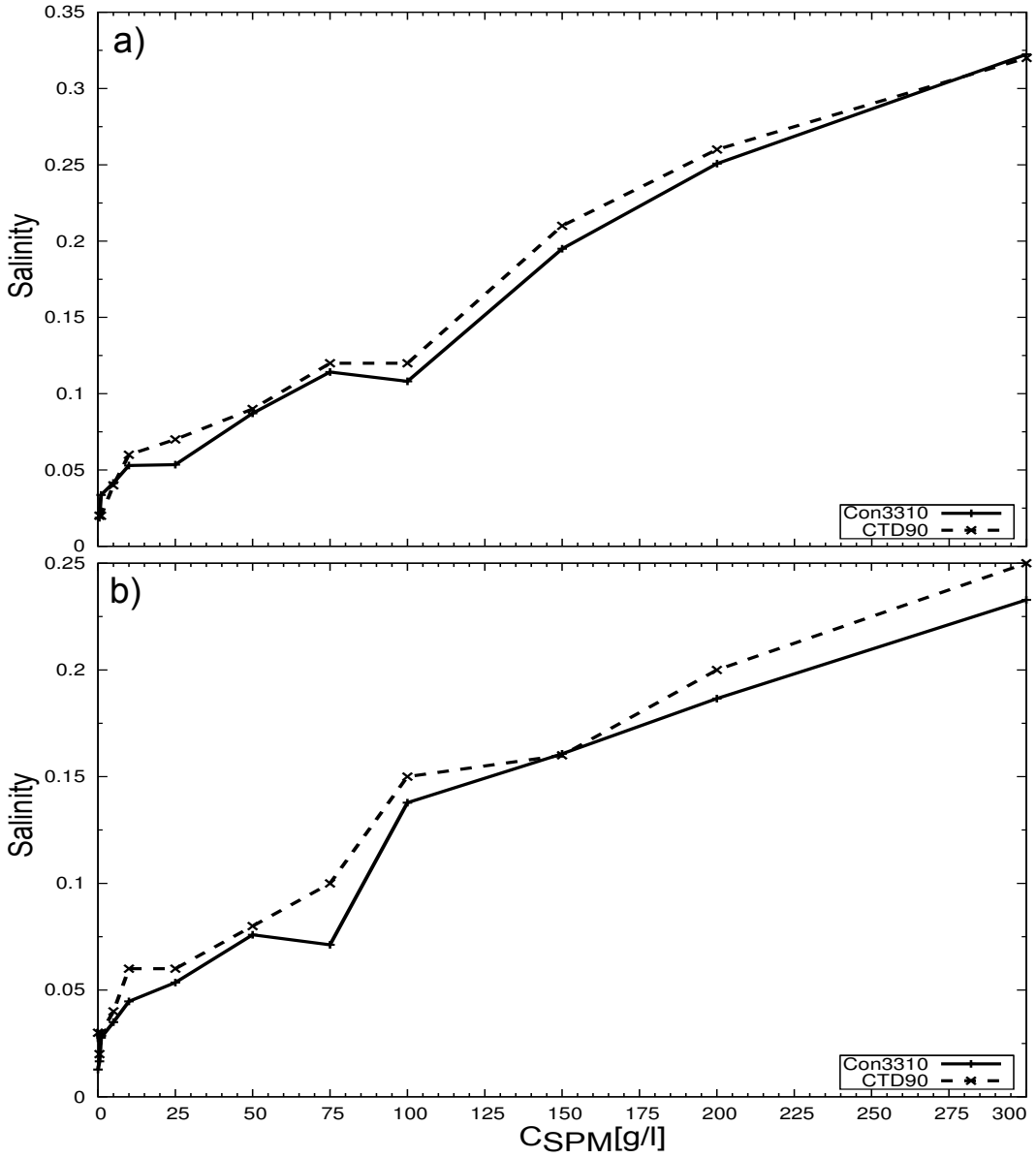

Figure 4.2: Salinity of the test solutions, before NaCl was added for the Ems estuary mud a) and for the Wadden Sea mud b). The values on the y-axis are expressed in terms of the PSU.

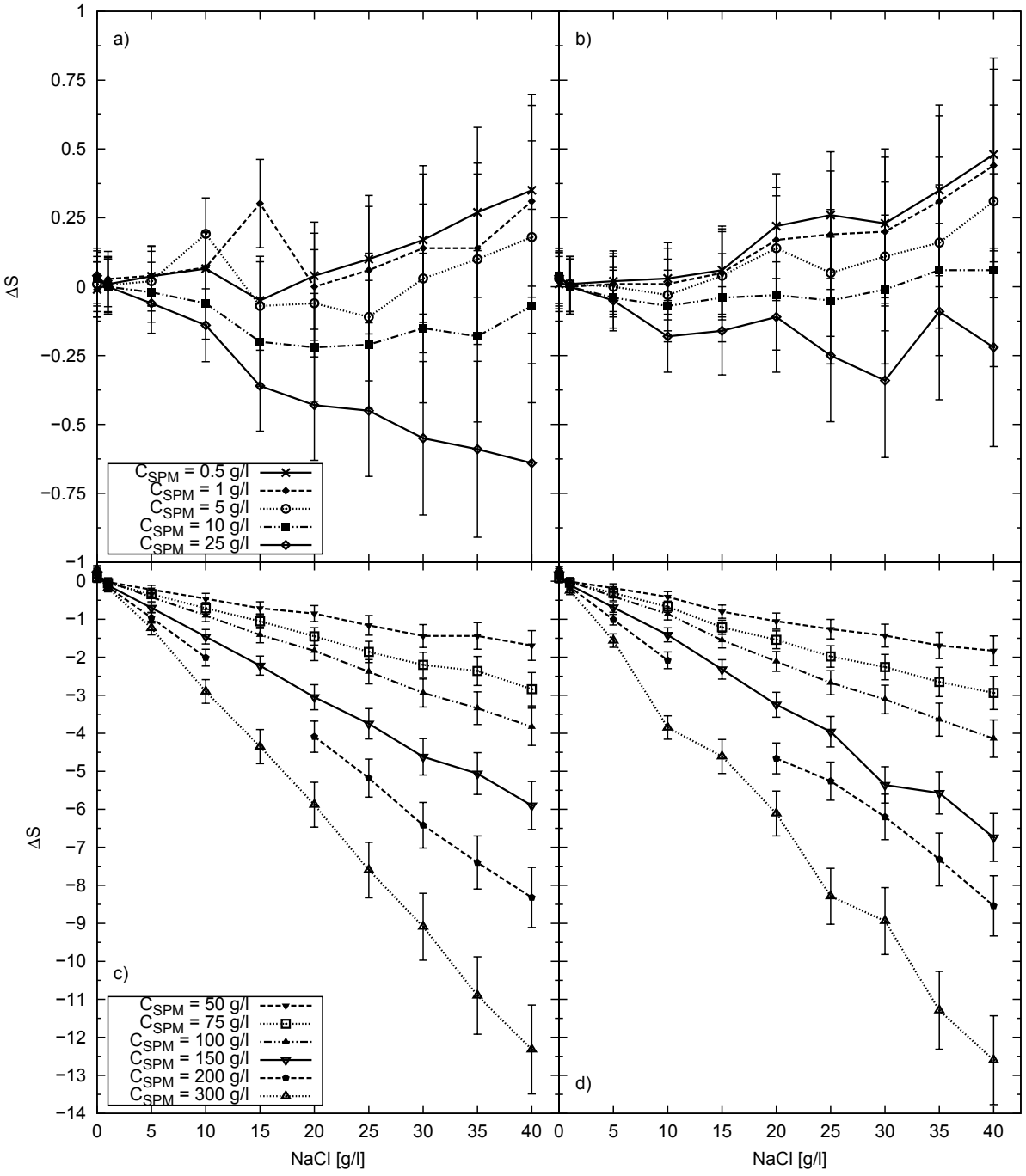

Figure 4.3: Salinity differences in dependence of the NaCl concentration for different SPM concentrations, measured with the CTD90 model (a and c) and the CON3310 model (b and d). These test runs were carried out with mud from the Ems estuary. The error bars represent the combined error of measurement uncertainty and uncertainties of adjusted salinity and SPM concentration.

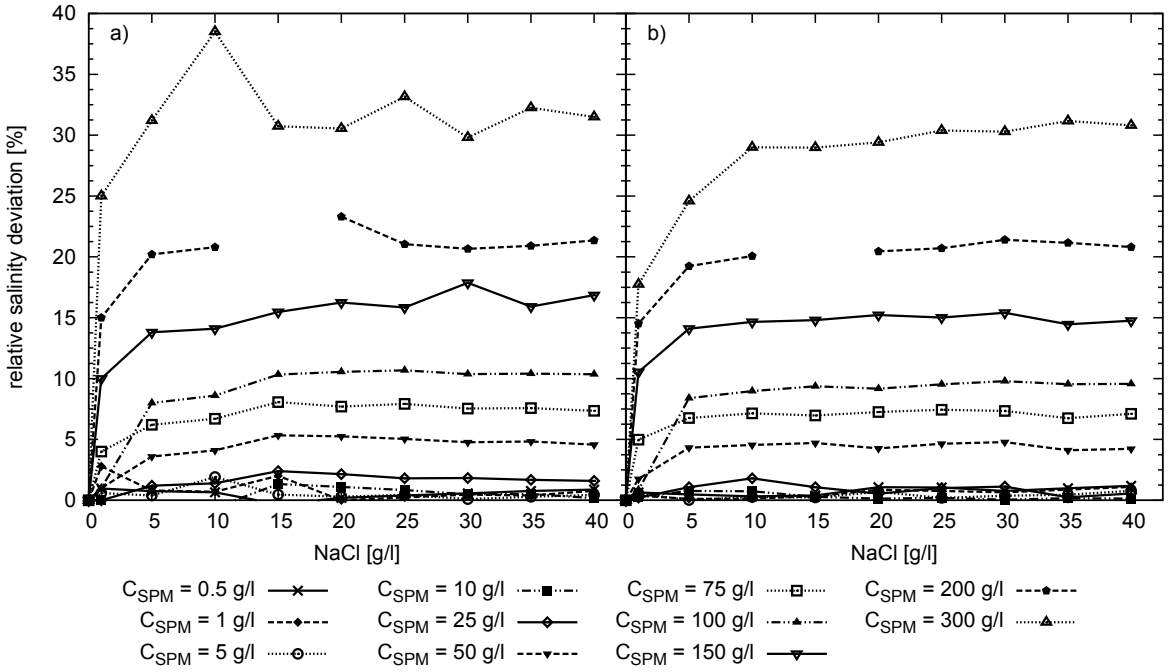

Figure 4.4: Relative salinity differences depending on the NaCl concentration for different SPM concentrations of the Ems estuary mud measured with the CTD90 model a) and the CON3310 model b).

l^{-1} NaCl, they remained almost constant for higher NaCl concentrations. The high variability of relative differences for test solutions with high SPM concentrations, e.g. 200 and 300 g l^{-1} must be accounted to the inability of keeping the mud in a homogeneous suspension. The suspension turbidity within the measuring cells could not be regarded as constant during the test runs with very high SPM concentrations.
The experiments with the mud samples from the Wadden Sea revealed the same features as described above for the test runs with Ems mud. This is exemplarily shown for the salinity differences obtained with the CTD90 model in Fig. 4.5, errorbars were not displayed in this figure for a better readability.

Ion adsorption by clay minerals

The results of the experiments about the ion adsorption by charged clay minerals are plotted in Fig. 4.6. Again, the shown results represent the difference between the measured salinity and the reference salinity value for the same NaCl concentration. The salinity differences ranged from -0.7 for 10 g l^{-1} NaCl and 75 g l^{-1} SPM (Fig. 4.6.a) to -4.0 for 35 g l^{-1} NaCl and an SPM concentration of 75 g l^{-1} (Fig. 4.6.b) in the well-

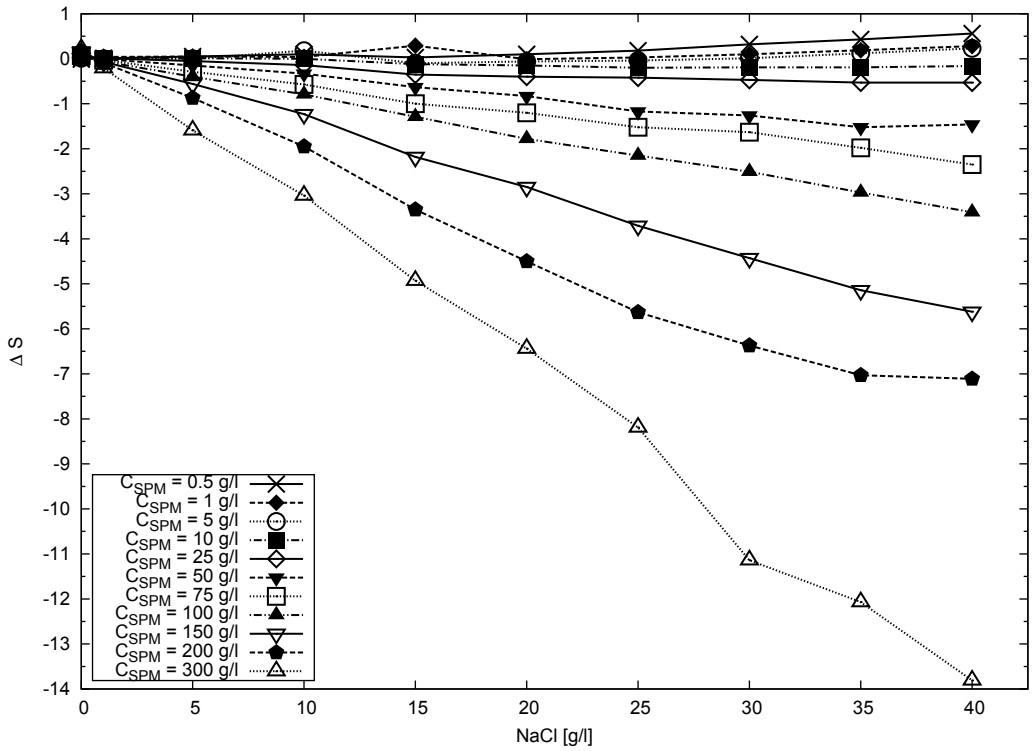

Figure 4.5: Salinity differences, depending on the NaCl concentration for different concentrations of SPM, measured with the CTD90 model; the SPM concentration in the different test runs was adjusted with mud from the Wadden Sea. Errorbars are not shown in this illustration, to improve the readability

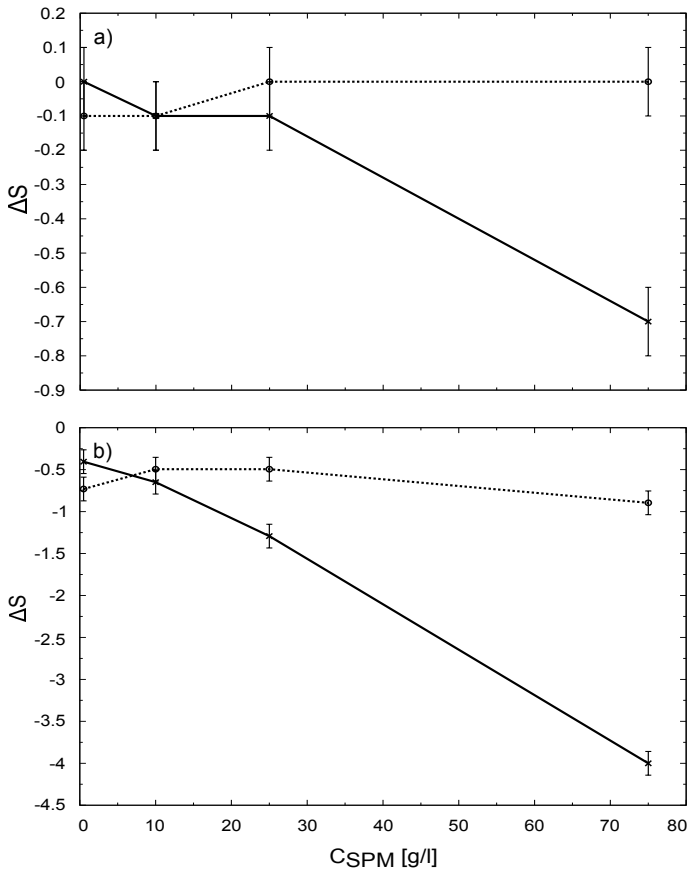

Figure 4.6: Salinity differences ΔS before (solid curve) and after centrifugation (dotted curve) of the test solution as a function of the SPM concentration for a NaCl concentration of 10 g l^{-1} a) and of 35 g l^{-1} b).

mixed solutions. After the test solutions had been centrifuged, the salinity differences were clearly reduced. They reached a maximum value of -0.1 in the solutions with 10 g l^{-1} and were hence in the range of the measurement uncertainty. However, the salinity differences of the centrifuged solutions with 35 g l^{-1} were still in the range between -0.5 and -0.9 and hence higher than the measurement uncertainty.
Thus, the salinity differences after centrifugation of the test solutions amounted to 20 - 25 % of the salinity differences in the well-mixed state.

4.1.5 Interpretation and discussion

The above presented results indicate that conductivity-based salinity measurements were affected by SPM. The obtained salinity values were generally lower than the real salinities of the turbid suspensions. These findings coincide with field observations done by

Traykovski et al. (2000) and Kineke et al. (1996). These authors reported on measured salinity values lower in fluid mud layers than in the overlaying water columns.
Despite the general trend, the salinity deviations were positive for "low" SPM concentrations, i.e. SPM <= 10 g l^{-1}. However, the positive deviations were lower than 1.5 % of the real value and were within in the range of the combined measuring uncertainties (Fig. 4.3.a+b). Again, the ΔS_i became greater and negative for SPM concentrations above 10 g l^{-1}, reaching up to 30 % of the real value. At this point it's worth noting, that a SPM concentration of 10 g l^{-1} is a widely accepted value for the transition from water to fluid mud (Manning et al., 2010; McAnally et al., 2007; Kineke and Sternberg, 1995; Ross and Mehta, 1989; Kirby, 1988).
Both used devices, the CTD90 model and the CON3310 model, revealed the same features during the measurements of the values. However, the amounts of these discrepancies were lower than the combined uncertainties of the measurements and of the adjusted salinities. This indicates, that the cell geometry design of the measurement instrument had no influence on the observed salinity deviations.
Furthermore, the results retrieved with mud samples from the two different origins were very similar regarding salinity differences, which were of the same order of magnitude, and the behaviour of the relative salinity differences.
In a second experiment, the adsorption of salt ions by charged clay minerals was examined. Clay minerals normally have low negative surface charge-distributions (Huang et al., 2012) and might be able to bind salt ions, themselves would not be available for the electrical current flow. The results of this study showed that ion adsorption by charged clay minerals could only explain for maximal 20 to 25 % of the observed salinity deviations in turbid solutions.
Depending on the requested accuracy of most salinity measurements, the effect of SPM on the retrieved data can be neglected for SPM concentrations below 10 g l^{-1}. This should be the case for most measurements on the shelf and especially in open oceans. To determine salinities in more turbid waters, such as coastal sites in particular estuaries, the method of Kineke and Sternberg (1995) is recommended. They collected water samples from fluid mud layers and measured the salinity after the SPM had settled. As shown by the results of the second experiment, this method would drastically decrease the error of salinity measurements. Only small deviations must be expected due to the adsorption of salt ions by charged clay minerals.
The graph of the relative differences between the measurements in the turbid mud solutions and the reference solutions (Fig. 4.6) leads to the following explanation of the

observed salinity differences. The relative differences were mostly constant for NaCl concentrations above 10 - 15 g l^{-1} in each test run. Among other parameters, salinity controls the flocculation of SPM (Mikeš, 2011; Mietta et al., 2009; Thill et al., 2001), i.e. increasing salinity promotes flocculation. This leads to an increasing size of the SPM. Flocculation was also visible during the experimental runs and the floc sizes seemed to be constant for NaCl concentrations above 15 g l^{-1}. SPM displaces water and thus reduces the water volume between the measuring electrodes, which is schematically shown in Fig. 4.7. This in turn decreases the cross section (parameter A in Eq. 4.2) of the virtual conductor between the electrodes. A decreased cross section results in a lower electrophoretic mobility of the ions which are responsible for the electrical current between the measuring electrodes. Since the ratio of $l\ A^{-1}$ is handled as a constant value by the conductivity meters, a lower current I is misinterpreted as a lower conductivity of the medium and subsequently a lower salinity is computed.
Assuming that the conductivity of water does not change, the volume concentration of the SPM can be calculated from the measured conductivities of the turbid and the reference solutions. To avoid temperature effects, the conductivities are corrected for 25 °C. In the following, $\kappa_{m,25}$ and $\kappa_{ref,25}$ denote the temperature corrected conductivities of a suspension and the reference solution, respectively:

$$\kappa_{m,25} = \frac{I_m}{U}\frac{l}{A}; \qquad \kappa_{ref,25} = \frac{I_{ref}}{U}\frac{l}{A_0} \tag{4.6}$$

here, I_m and I_{ref} are the electrical currents of the test suspension and the reference solution, respectively, and A_0 is the cross section. Under the assumption, that the conductivity of the water is not changed by SPM and only the cross section is reduced in a suspension, the following statement is also true:

$$\kappa_{susp,25} = \frac{I_m}{U}\frac{l}{A_{susp}} = \kappa_{ref,25} \tag{4.7}$$

where A_{susp} is the effective cross section in the suspension. Transforming this expression and combining it with the left-side of Eq. 4.6:

$$\kappa_{ref,25} = \frac{I_m}{U}\frac{l}{A_{susp}}\frac{A_0}{A_0} = \kappa_{m,25}\frac{A_0}{A_{susp}} \tag{4.8}$$

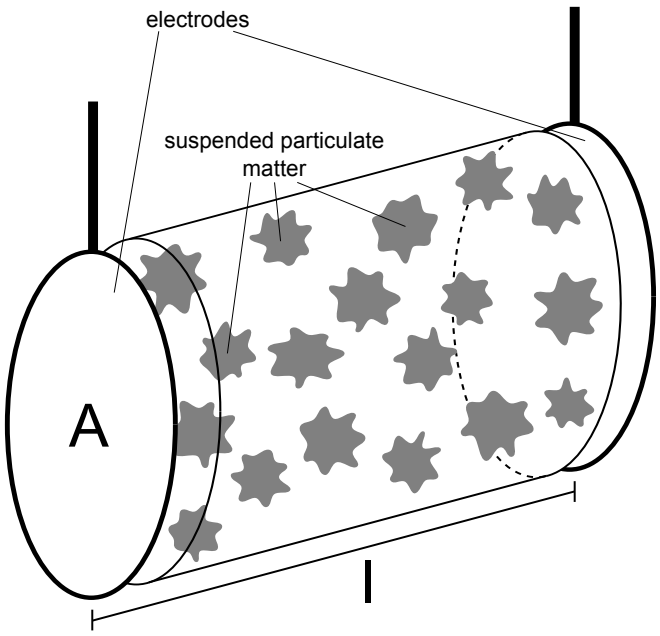

Figure 4.7: Schematic representation of a conductivity measuring cell with dissolved particles and flocs.

Using the volume expression: $V = A \cdot l$ yields:

$$\frac{V_{W,susp}}{V_0} = \frac{\kappa_{m,25}}{\kappa_{ref,25}} \tag{4.9}$$

where $V_{W,susp}$ is the water volume in suspension. Eq. 4.9 is an expression for the relative water content in suspension and can also be used to calculate the volume concentration of SPM via the electrical conductivity.

Results of the relative water content of the test solutions with the Ems estuary mud are shown in Fig. 4.8. For NaCl concentrations below 5 g l^{-1} the relative water volume was over 100 %, this was again caused by rest salinity in the mud samples. Hence these values were not further considered. For more than 15 g l^{-1} NaCl the relative water volume in the measuring cell was constant, expect for the 300 g l^{-1} SPM solution. These results support the assumption, that the influence of the SPM on salinity measurements is caused by a "blinding effect" of the conductivity sensor by the dissolved particles.

4.1.6 Conclusion

In this study, the influence of the SPM on salinity measurements was investigated in detail for the first time. Test runs with suspensions of different SPM and NaCl concen-

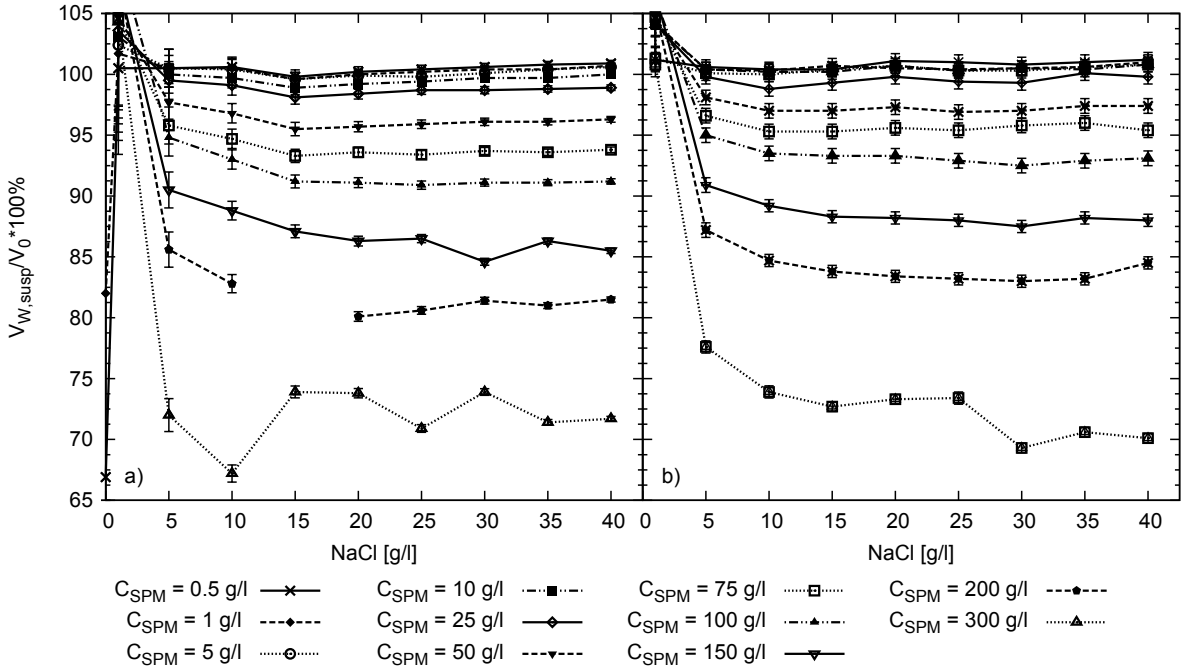

Figure 4.8: Ratio of the water volume to the cell volume in percent, calculated for the measurements with the CTD90 model a) and with the CON3310 model b) for the experiments with mud from the Ems estuary.

trations were carried out and the measured salinity was compared with salinity measurements in reference runs without SPM. To set up required suspensions with different SPM concentrations, as well as to verify potential influence by different mineral composition, mud samples from different origins were used after desalination. Salinity measurements were done by using two devices with different measuring cell geometries.

It was found out that SPM disturbs salinity measurements at concentrations above 10 g l^{-1} in the way that it leads to incorrect salinity values. The difference between salinity measurements in the test solution and in a reference solution (ΔS_i) increased with increasing SPM concentration and with increasing NaCl concentration. It could be shown, that the deviations can reach up to 30 % for a SPM concentration of 300 g l^{-1}. For lower SPM concentrations, i.e. $<$ 10 g l^{-1}, the deviations were below 1.5 % and in the range of the combined error of measurement uncertainty and accuracy of the set up of NaCl and SPM concentration. Hence, for salinity measurement in waters with low turbidity the error caused by the SPM may be negligible, depending on the requested accuracy. However measured salinity values of high turbid waters, e.g. fluid mud layers, should be handled with care. Salinity measurements in decanted water samples of these layers will yield more reliable results.

The adsorption of salt ions by charged clay minerals only explained about 20 - 25 % of the observed salinity deviations. Incorrect salinity values in turbid water are ascribed to a “blinding effect” of the conductivity sensor. Solid matter, i.e. single particles and flocs reduce the cross section of the virtual conductor within the measuring cell which in turn decreases the current between the electrodes. It was also found out that the measuring cell design had no recognisable influence on the observed salinity deviations.

4.1.7 Acknowledgements

The authors would like to thank Angela Trumpf for her support in the laboratory. This study was funded by the Deutsche Forschungsgemeinschaft as part of the Cluster of Excellence 'The Future Ocean'. Julian Jess is thanked for the language corrections. We would also like to thank the reviewers for their constructive criticism.

4.2 Sound velocity of natural sediment suspensions and their hydro-acoustic reflectivity

4.2.1 Abstract

Ultrasonic measurements are common and important methods in marine and coastal sciences. Echo sounders have been applied on seagoing vessels since the early last century. The influence of the water temperature, salinity and the depth on the sound velocity is nowadays quite well understood while the influence of suspended particles is not. Despite this, it is well known that sediment loaded water layers can create hydro-acoustic reflections.
In this study, the correlation between suspended particle concentration and sound velocity was investigated in the frame of laboratory, field and numerical experiments. The results of the laboratory and field experiments revealed a negative linear correlation between suspended particulate matter concentration and sound velocity. They also indicate a correlation between the sound velocity and the size of the suspended particles. Numerical calculations of the speed of sound in natural suspensions failed due to the unknown mechanical and acoustical properties of the particles aggregates. Therefore, further investigations on these parameters are suggested.
A simulation of the reflectivity of sediment-induced interfaces within the water column with a weak-scattering model confirmed the assumed correlation between the acoustic reflectivity, the signal frequency and the width of the interface.

Key words: Sound propagation, scattering, reflection coefficient, acoustic impedance, fluid mud

4.2.2 Introduction

Acoustical echos of interfaces within the water column are a known phenomenon since the first half of the last century. In natural water bodies like lakes, estuaries, coastal waters and the oceans, such interfaces normally occur between two layers of different temperature and/or salinity. Among other properties, both of them determine the density and the sound velocity and therefore the propagation of a sound wave. The discovery that a sound wave is affected by a layer of different temperature was the beginning of the acoustical oceanography in 1937 (Bjørnø, 2003). Nowadays, the correlation between sound velocity, temperature, salinity and pressure is well explored. But there are other

parameters which can affect the acoustical properties of a water layer, like suspended particles (Hoitink and Hoekstra, 2005; Jan Kowalski, 2004; Mobley et al., 1999; Temkin, 1998, 1992; McClements and Povey, 1989; Harker and Temple, 1988). This is especially important in energetic coastal waters where high turbid layers frequently occur. Such layers, which are a mixture of water, clay, mud and organic slime, are termed fluid mud, if their suspended particulate matter (SPM) concentration exceeds 10 g l^{-1}. They are often topmost bounded by a lutocline, which is a sharp gradient of SPM concentration. Such sediment induced interfaces can cause acoustical back-scattering which became apparent with the introduction of echo sounders on ships in the 1930s (Kirby, 2013).
In general, sound waves are partly reflected at boundaries between layers of different acoustic impedance Z:

$$Z = \rho \cdot c \tag{4.10}$$

where ρ is the density and c is the sound velocity. If both layers have the same acoustic impedance, reflections won't occur. The reflection coefficient R is the ratio of the sound pressures of the reflected wave to the incident wave. It can also be expressed by means of the acoustic impedance:

$$R = \frac{Z_2 - Z_1}{Z_1 + Z_2} \tag{4.11}$$

where Z_1 and Z_2 are the acoustic impedance of the first and second layer, respectively. In addition, the acoustic backscattering ability depends on the impedance gradient, i.e. how fast acoustic impedance changes compared to the acoustical wave length. Penrose and Beer (1981) modelled the reflection of an initially sharp pycnocline, which is broadened by diffusion, as a function of time. During this simulation, the reflection coefficient was rapidly decreasing. After a few hours it was too weak to cause detectable echoes. Additionally, the predominant opinion in literature is that natural salinity and temperature variations are not strong enough to create detectable backscattering. Hence, Penrose and Beer (1981) assumed that the accumulation of biota in the vicinity of pycnoclines was responsible for the observed acoustic echos. However, Seim (1999) found out that the sound propagation is strongly affected by salinity stratification in coastal waters.
To simulate the reflectivity of turbid water layers, the densities and sound velocities of these layers are required. Whereas the contribution of SPM to the density can be easily assessed, its influence on the sound velocity is not yet fully understood.
If the acoustic properties of fluid mud were known, ultrasonic measurements could be used to characterize natural SPM suspension (Maa et al., 1997). Such methods are

already used for industrial tasks, e.g. determination of particle concentrations in ice slurries (Langlois et al., 2011). Knowing the scatter-ability of sediment-induced interfaces would also provide a way for the detection and monitoring of turbid layers near the bottom, which is important for the managing and dredging of navigational channels near muddy coasts. The knowledge of fluid mud deposits improves also the forecasts of tidal models. Gabioux et al. (2005) showed that the predictions of tidal models will better match real tide levels if fluid mud deposits are taken into account. In general, the distribution of unconsolidated mud layers is important when trying to predict the wave energy input on coasts, because muddy layers reduce the bottom friction of shoaling waves.
In this study, the influence of SPM on the sound velocity was investigated in the frame of a laboratory study with natural fluid mud samples of different concentration. The gained results were compared with field measurements and outputs of two numerical models. Additionally, reflectivities of real lutoclines were simulated with a weak-scattering model.

4.2.3 Methods

Laboratory measurements

In the laboratory, sound velocity measurements were done in test solutions of specific SPM concentration, temperature and salinity. The SPM concentrations were set up with natural mud samples which had been collected during a survey in the Ems estuary from 11.06.2012 to 14.06.2012. The fluid mud samples were collected with a horizontal water sampler (HydroBios©) near the bottom. This sampler had a volume of approximately 2 l and an attached fin allowed the sampler to align in the current. The fluid mud samples had to be desalinated before they could be used to adjust the SPM concentration of the test solutions. The desalination was necessary because a salty mud would have distorted the adjusted salinity in the test solutions. To desalinate the mud, a mixture of mud and distilled water was filled into dialysis tubes which were subsequently transferred into a bath of distilled water. Dissolved ions were able to pass through the tube walls, driven by the osmotic effect. The water of the bath was continuously exchanged to maintain a salinity gradient between the exterior and interior of the tubes. A settling of the mud was hindered by periodically shaking the tubes. The mixtures of water and mud were kept in the water bath until they have reached a salinity of zero. The samples were afterwards concentrated by a remove of the clear excess water after the SPM had settled. Apart from these treatments the fluid mud samples were kept in a natural state.

Size analyses of these mud samples were done with a Beckman Coulter laser (LS 13320) for sub-samples. A detailed description of this method and the device is given in Papenmeier et al. (2014).
For the experimental runs, suspensions of different SPM concentrations were adjusted by diluting a specific volume of the fluid mud samples with distilled water. The salinities in these suspensions were adjusted with commercial NaCl. Settling of the SPM was avoided by mixing the suspensions with a magnetic stirrer.
The speed of sound in these suspensions were measured with a sound velocity probe of type Echometer 1076 K by Karl Deutsch, which had a resolution and accuracy of 0.1 m s^{-1}.

Field measurements

The velocities of sound in fluid mud were also measured under real conditions during the Ems survey from 11.06.2012 to 14.06.2012. For this, sound velocity profiles were recorded with a Reason SVP-T15 sound velocity profiler during slack water phases. The profiler operated at a frequency of 2 MHz and had a resolution of 0.1 m s^{-1} and an accuracy of 0.25 m s^{-1}, as stated by the manufacturer. CTD (Conductivity Temperature and Depth) profiles were simultaneous taken to record temperature and salinity profiles. Water samples were additionally taken every meter of water depth. Salinities were also measured in these water samples after the SPM had settled. Salinity measurements in the clear excess water of the water samples provided more reliable salinity values than the CTD measurements, since SPM can also disturb salinity measurements (see Chp.: 4.1). SPM concentrations were determined by vacuum filtration of an aliquot of each water sample through a glass fibre filter (1.2 µm pore diameter).

Calculation of the velocities of sound in suspensions

The sound velocities were calculated by the use of different approaches. One method was to use the results gained during the laboratory and field measurements. The salinities, temperatures and depth of the water samples collected during the survey were used to calculate the velocity of sound in clear water with the equation of Chen and Millero (1977). The gained results were then corrected for the SPM concentration of the water sample with the correlation factor derived from the laboratory experiments.
In addition, two approaches for the determination of the sound speed, which were published in literature, were used. The first approach was to regard the suspensions as

homogenous media with a specific density and sound velocity and to neglect sound scattering by the suspended particles (Hamilton, 1970). Applying this approach, which should be valid if the particles are small in comparison to the acoustic wave length, the velocity of sound c in a suspension of rigid particles reads (Wood, 1941):

$$c = \sqrt{\frac{1}{\rho_{\text{eff}} \kappa_{\text{eff}}}} \tag{4.12}$$

where ρ_{eff} and κ_{eff} are the effective density and compressibility of the suspension, respectively. The density of a suspension was estimated with the following expression (Gabioux et al., 2005):

$$\rho_{\text{eff}} = C_{SPM} \frac{(\rho_S - \rho_W)}{\rho_S} + \rho_W \tag{4.13}$$

where C_{SPM} is the SPM concentration, ρ_W is the water density depending on the salinity and temperature and ρ_S is the density of the suspended particles. The effective compressibility was calculated via (Harker and Temple, 1988):

$$\kappa_{\text{eff}} = \phi \kappa_W + (1 - \phi) \kappa_S \tag{4.14}$$

where ϕ is the volume fraction of the suspended particles, κ_S and κ_W are the compressibilities of the suspended particles and water, respectively. It was shown in chapter (4.1) that quartz is the most frequent fluid mud mineral at the collection site, therefore the density of quartz (ρ = 2650 kg m^{-3}) was used for the calculations of Eq. 4.13 and 4.14. Vsemirnova et al. (2012) modeled a seismogram of turbid bottom layer in the Faroe-Shetland Channel with this approach. The obtained results were in a good agreement with their air-gun measurements.

The second used mathematical approach, to calculate the velocity of sound in suspensions, was to regard the scattering of an acoustic wave by each single particle. In this approach, each suspended particle responds on the incident wave as scatterer and generates a phase-shifted secondary wave, propagating in all spatial directions. The resulting sound wave at a random point is then the superposition of the primary and all scattered secondary waves. The scattered secondary waves will have to be taken into account, if the acoustic wave length is in the range or smaller than the suspended particles.
In general, the scattered waves are anisotropic with amplitudes depending on the spatial angle and the frequency of the incident wave. James J. Faran (1951) derived a mathematical description for the amplitude of the secondary wave for scattering at solid

cylinders and spheres. Mobley et al. (1999) developed a method to calculate the speed and attenuation of a sound wave in suspensions, based on these Faran's amplitudes and the complex wave number for multiple scattering, found out by Waterman and Truell (1961). Mobley et al. (1999) only regarded forward scattering of the sound wave and obtained the following expression for the sound velocity:

$$c(\omega) = \frac{c_W}{1 - \frac{2\pi c_W^3}{\omega^3} \sum \eta(a_q) \sum (2n+1) \Im[D_n(\omega)]} \tag{4.15}$$

where c_W is the sound velocity in water, ω is the angular frequency of the sound wave, $\eta(a_q)$ is the number density of particles with a diameter of a_q, D_n are the expansion coefficients and Im denotes the imaginary part. The D_n's were related to Faran's c_n by:

$$D_n = \frac{c_n}{p_0(2n+1)(-i)^n} \tag{4.16}$$

where p_0 is the pressure of the incident sound wave. $c(\omega)$ means that the velocity of sound in the suspension in the dependence of on the angular frequency, i.e. the sound propagation is dispersive in the suspensions. Faran's expansion coefficients depend on the acoustical behaviour of the suspended particles, i.e. the speeds of the compression and shear waves within the scatterer. Mobley et al. (1999) achieved a good agreement between their calculations and measurements in suspensions consisting of water and polystyrene beats of different particle size distributions.
In order to account also for a "first order" multiple scattering, Eq. 4.15 was expanded by terms, expressing a single backward and subsequent forward scattering of the acoustic wave. It then became:

$$\begin{aligned} c(\omega) = c_W \cdot \Bigg[& 1 - \frac{\eta 2\pi c_w^3}{\omega^3} \sum_{n=0}^{\infty} (2n+1) \operatorname{Im}[D_n(\omega)] \\ & + \frac{1}{2} \frac{4\pi^2 c_W^6}{\omega^6} \left(\sum_q \eta(a_q) \sum_{n=0}^{\infty} (2n+1) \operatorname{Re}[D_n(\omega)] \right)^2 \\ & - \frac{1}{2} \frac{4\pi^2 c_W^6}{\omega^6} \left(\sum_q \eta(a_q) \sum_{n=0}^{\infty} (2n+1) \operatorname{Im}[D_n(\omega)] \right)^2 \Bigg]^{-1} \end{aligned} \tag{4.17}$$

where Re denotes the real part. Again, quartz was regarded as the main scatterer for these calculations.

Simulation of the reflectivity of a pycnocline

Ross and Lavery (2012) developed a weak-scattering model to simulate the reflectivity properties of oceanic pycnoclines. This model is an improvement of a model which was developed for a laboratory study of a double diffuse microstructure (Lavery and Ross, 2007). The model divides the interface or pycnocline of interest in several sublayers of constant density and sound velocity. The width of such a sublayer is controlled by the signal frequency and defined to be $\Delta = \lambda/20$, where λ is the wave length of the signal. Reflections of a sound wave occur at both sides of a sublayer, which can be calculated using Eq. 4.11, respectively. The superposition of both part waves leads to interference effects due to their different path lengths. In order to account for these interferences, the reflected waves have to be coherently added. A detailed description of this procedure for a three layer system is given in Brandt et al. (1996). Adding coherently the reflectivities of all sublayers yields the following expression for the total reflectivity of a pycnocline (Ross and Lavery, 2012):

$$R_{\mathrm{tot}} = \frac{1}{2} \frac{\sum_{n=(M-1)N}^{MN} R_{n,n+1} \exp\left(2i \sum_{m=(M-1)N}^{n} k_m \Delta\right)}{1 + \sum_{m=(M-1)N}^{n} \Delta / r_{scat}} \tag{4.18}$$

where $R_{n,n+1}$ is the reflectivity of the interface between the sublayers n and $n+1$, k_m is the wave number in sublayer m and r_{scat} is the distance between the average depth of the pycnocline and the transducer.

4.2.4 Results

Grain size distribution of the mud samples

The grain size distribution of the collected fluid mud sample together with its two-fold standard deviation are shown in Fig. 4.9. The results showed that the mud sample mainly consisted of the clay and silt fraction.

Sound velocity measurements in the laboratory

First of all, the results of the laboratory experiments with the synthesized fluid mud suspensions were presented. The sound velocity measurements in dependence of the SPM concentration for 8 and 21 °C and a salinity of zero are shown in lower and upper part

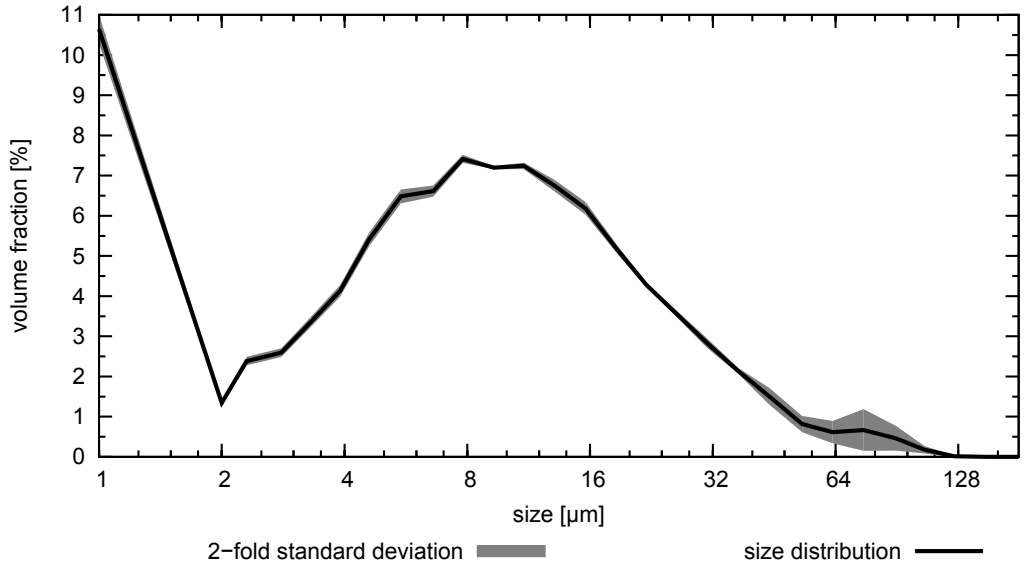

Figure 4.9: Grain size distribution of the fluid mud sample. The grey area indicates the 2 fold standard deviations. The x-axis is logarithmic scaled.

of Fig. 4.10, respectively. Both curves show a clear linear decrease of the sound velocity with increasing SPM concentration. Hence, the measurements were linearly fitted, the corresponding regression curves are also shown in Fig. 4.10. Such experimental runs and regression analyses were done for several temperatures and salinities. The results indicated that salinity reduces the influence of SPM on the sound velocity. In the experimental runs with up to 5 g l^{-1} NaCl the slope of the regression lines varied between -0.029234 and -0.040741 m s^{-1} (g l^{-1})$^{-1}$, whereas it was -0.022448 or only -0.019101 m s^{-1} (g l^{-1})$^{-1}$ at NaCl concentrations of 10 and 20 g l^{-1}, respectively. Hence, the slope of the regression curves was milder for higher salinities. For up to 5.0 g l^{-1}, the average correlation factor between the SPM concentration and sound velocity was -0.034535 $\pm$ 0.003826 m s^{-1} (g l^{-1})$^{-1}$. This value was quite small in comparison with the influence of temperature or salinity.

Sound velocity measurements in dependence of the temperature for different SPM concentrations (0, 0.5, 10 and 50 g l^{-1}) are show in Fig. 4.11. The curves ran parallel and were shifted to smaller values for higher SPM concentrations. There were no hints for higher order dependences between SPM concentration, temperature and sound velocity, recognizable in the run of the curves.

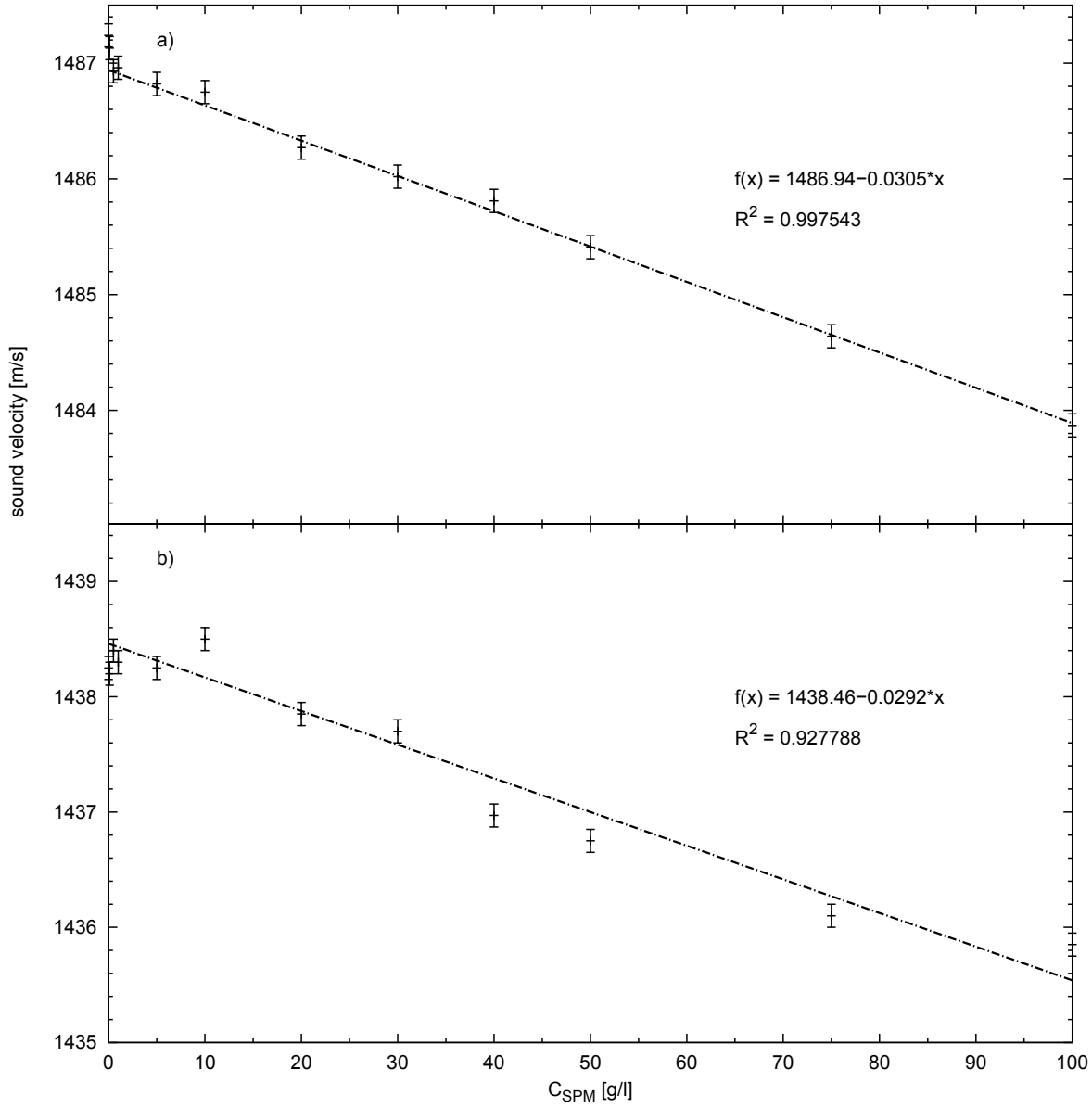

Figure 4.10: Sound velocities in dependence of the SPM concentrations, for a salinity of zero and a temperature of 21 °C (a) and 8 °C b).

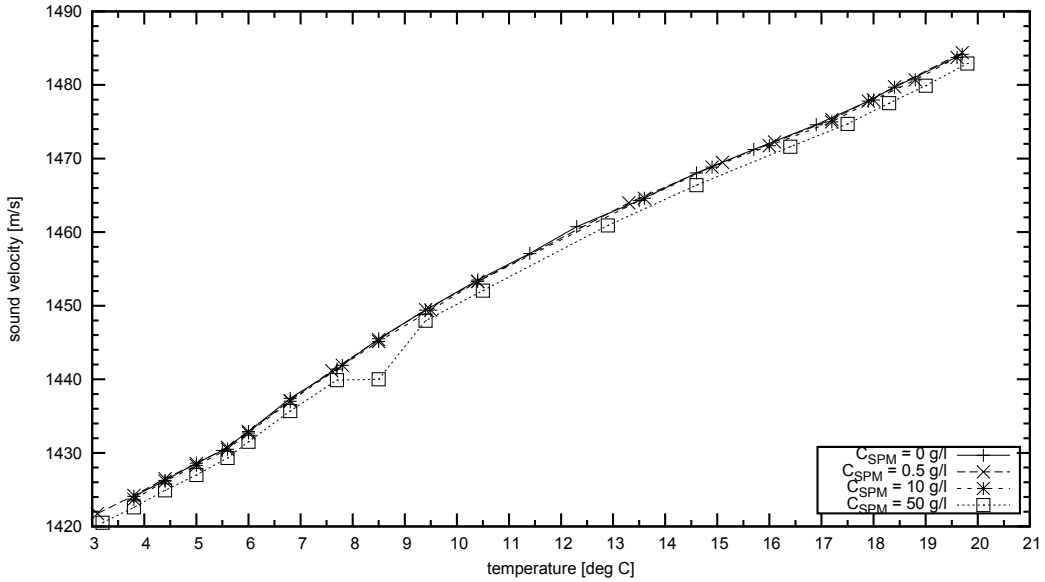

Figure 4.11: Sound velocities in dependence of the temperature for different SPM concentrations. The curves are shifted to lower sound velocity values for higher SPM concentrations.

Sound velocity measurements in the Ems estuary

The sound velocity profiles which were recorded during the Ems survey in June 2012 are presented in Fig. 4.12. A lutocline was manifested by a sharp decrease of sound velocity in the profiles b-e, whereas there was no lutocline recognizable in the profile a.

Calculated sound velocities

The results of two different methods to calculate the speed of sound in suspensions are also shown in Fig. 4.12. One set was calculated with the correlation factor of the laboratory experiment and the other one was calculated by use of the two-phase model described in Eq. 4.12. The results of both methods revealed a strong decrease of the sound velocity near the depth of the lutocline. However, the influence of SPM on the sound velocity was underestimated when applying the laboratory results and overestimated by the two-phase model. Except in the cases of panel d, where both methods provided values for the sound velocity which were higher than the measured ones.
The results of the scattering model (Eq. 4.18) are presented in dependence on the frequency for different SPM concentrations in Fig. 4.13. There was no dispersive behaviour recognizable in the frequency range of 0 to 1000 kHz. The results in dependence on the SPM concentration together with a linear fit are shown for a frequency of 100 kHz in Fig.

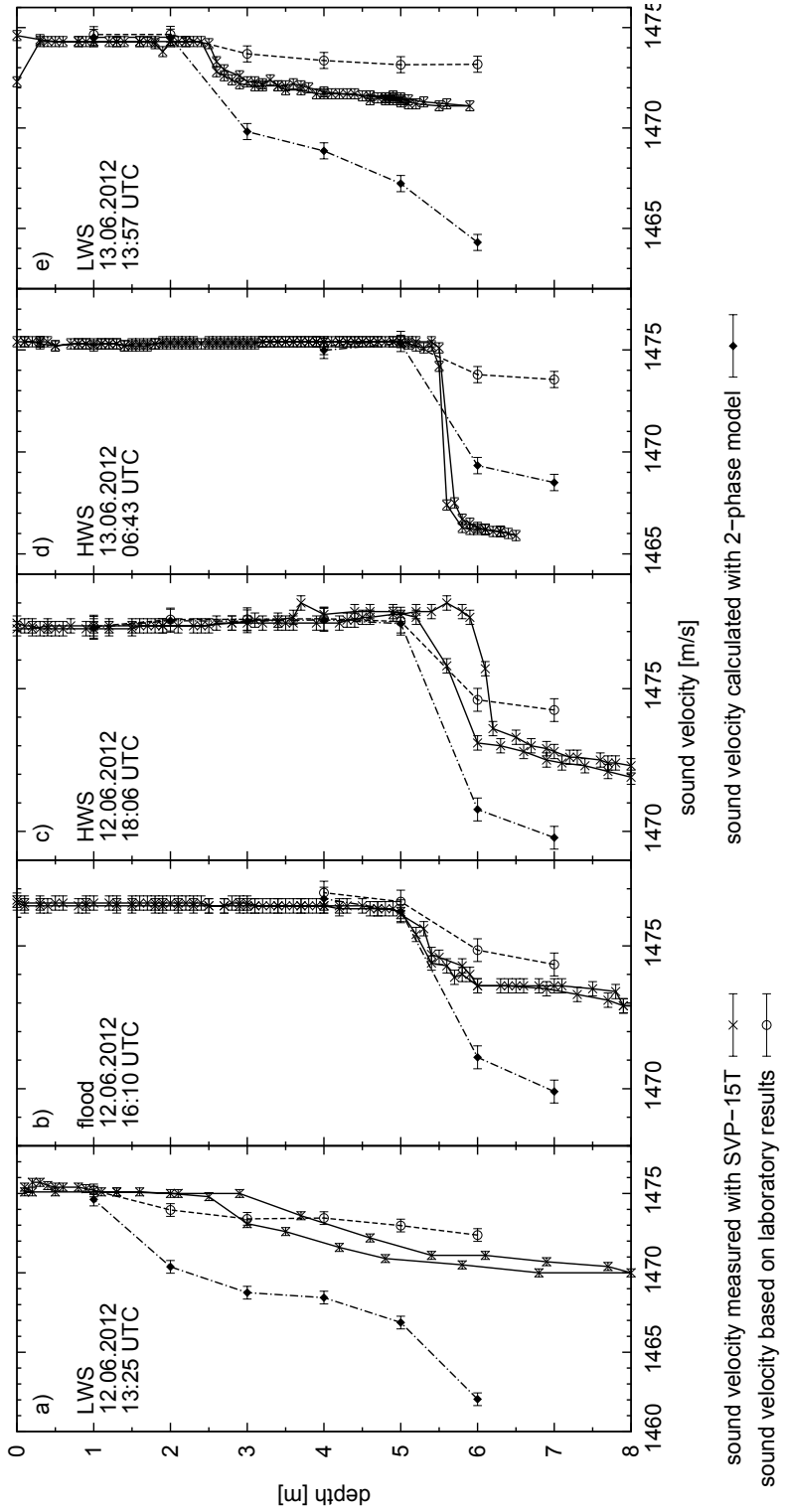

Figure 4.12: Sound velocity profiles recorded during the Ems survey in June 2012. The measured sound velocities are compared with values calculated with the found correlation factor and with values theoretically derived with a two-phase model (Eq. 4.12).

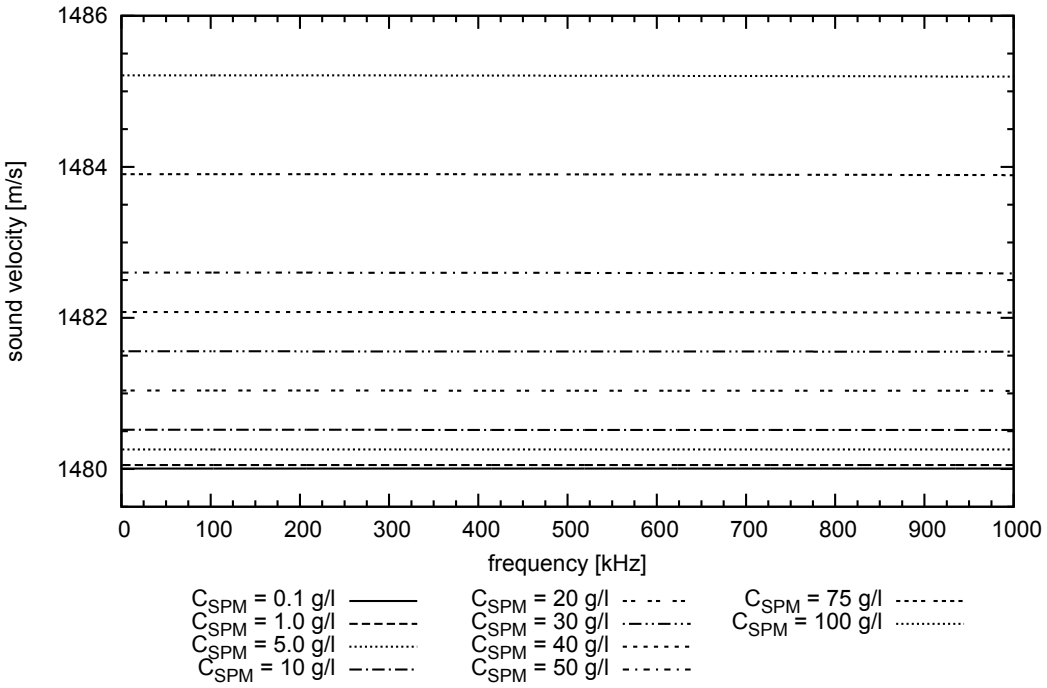

Figure 4.13: Sound velocity in dependence on the frequency for different SPM concentrations. The values of the sound velocity were calculated with the scattering model described in Eq. 4.17.

4.14. The correlation was positive with a slope of 0.0521 m s^{-1} (g l^{-1})$^{-1}$ and a correlation coefficient of 0.9999352993.

Simulations of the reflectivities of natural lutoclines

The simulated reflectivities of lutoclines, observed during the Ems survey in June 2012, are present in Fig. 4.15. This figure shows in the upper panel (Fig. 4.15.a) the maximum reflectivity coefficients and the depth of the maximum reflection in the lower panel (Fig. 4.15.b), each in dependence on the frequency. As it was seen from these results, the reflectivity of a sediment-induced interface depended strongly on the signal frequency and was generally higher for lower frequencies. Constructive and destructive interferences caused oscillations which were superimposed on this general trend. For the same reason, the depth of backscatter varied by few decimeters, meaning that signals differ in frequency will be reflected at different depth with different strength.

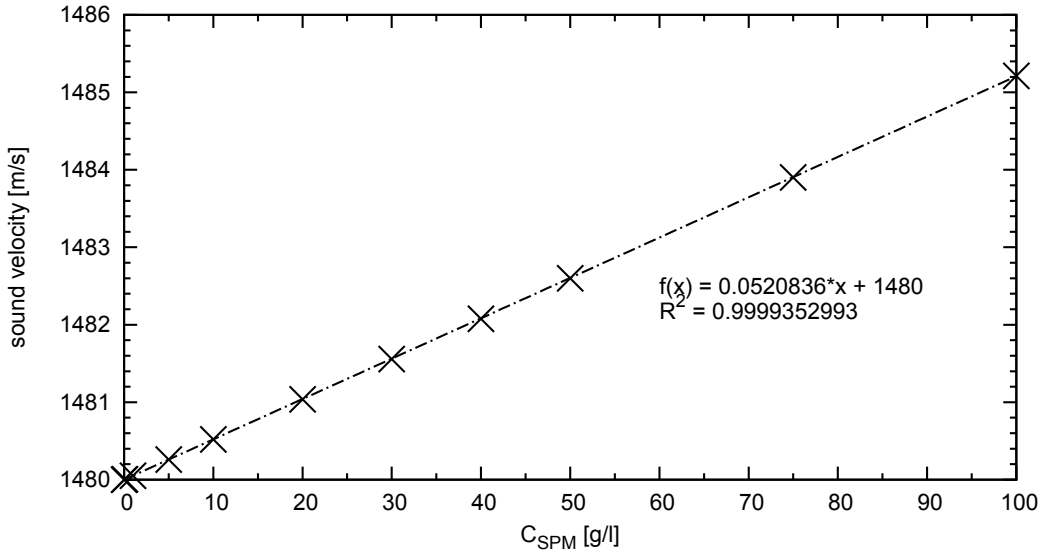

Figure 4.14: Sound velocity in dependence on the SPM concentrations for a frequency of 100 kHz. The values of the sound velocity were calculated with the scattering-model of Eq. 4.17.

4.2.5 Interpretation and discussion:

Laboratory experiments with adjusted fluid mud suspensions revealed a clear linear decrease of sound velocity with increasing SPM concentration. The correlation factor between SPM concentration and sound velocity was ascertained to be $\Delta c/\Delta C_{SPM}$ = -0.035 m s^{-1}/ 1 g l^{-1}, and hence significantly lower than the influence of temperature ($\Delta c/\Delta\theta$ 4.0 m s^{-1}/ 1 °C), salinity ($\Delta c/\Delta S$ 1.4 m s^{-1}/ 1 (PSU)) or even depth ($\Delta c/\Delta p$ 0.17 m s^{-1}/ 1 bar).

A decrease of the acoustical wave speed was also observed in some consolidated mud layers at the sea bed, even though sound velocity is normally higher in solid matter than in fluids. Schneider von Deimling et al. (2013) found out that gas bubbles in the mud layers were responsible for this phenomenon. These gas bubbles usually consist of methane, produced by bacteria under anaerobic conditions, have been observed worldwide (Robb et al., 2006). In general, the influence of gas bubbles on the sound propagation depends on the ratio of bubble size to the acoustical wave length. The wave speed is reduced for signal frequencies below the resonance frequency of the gas bubbles, whereas it is unaffected for signal frequencies much higher than the resonance frequency (Wilkens and Richardson, 1998). Near the resonance frequency the sound propagation is dispersive (Robb et al., 2006). However, the occurrence of gas bubbles in fluid mud layers is

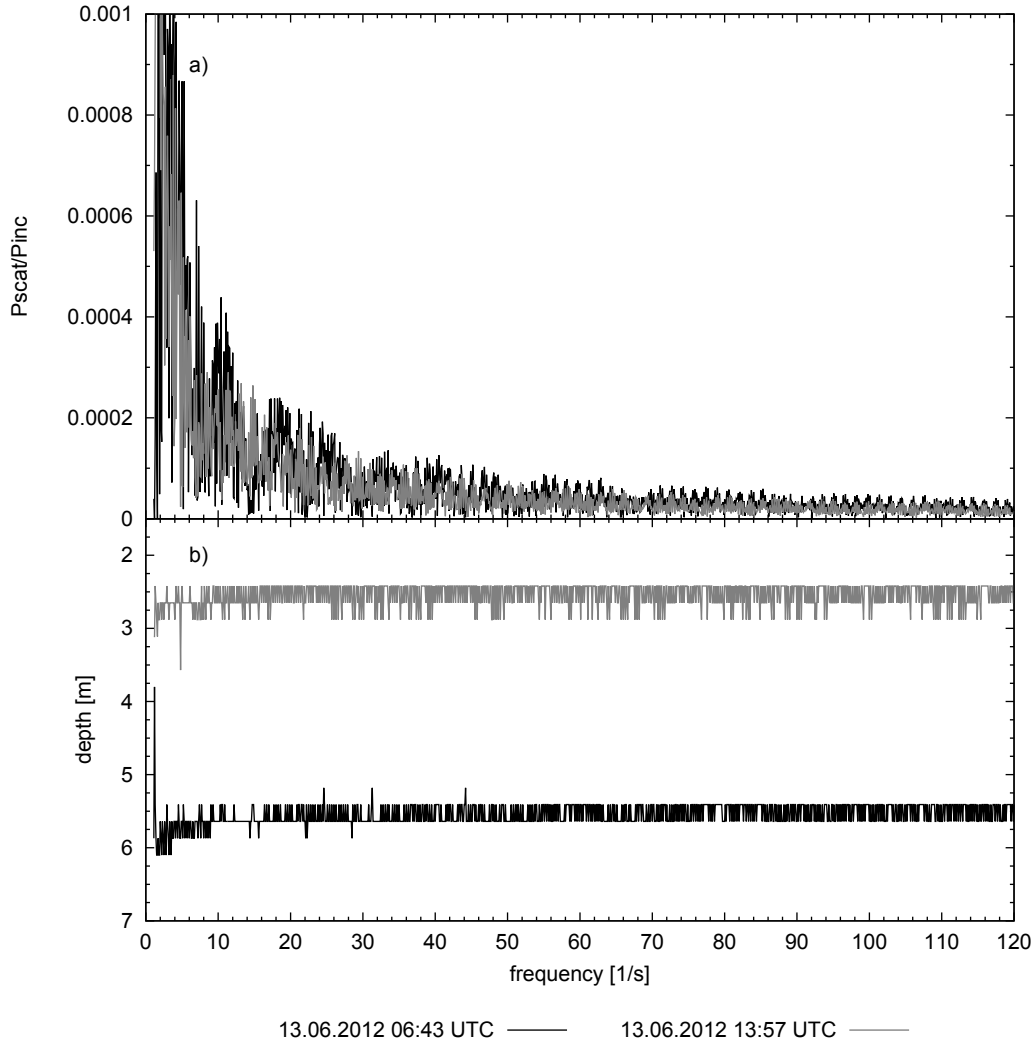

Figure 4.15: Simulated reflectivities of two lutoclines observed during the Ems survery in June 2012 (a) and the depth of the maximum reflections (b). The results were simulated with the weak-scattering model described in Eq. 4.18.

implausible, since they would escape due to their buoyancy.
Calculated values of the speed of sound in suspensions didn't match with the field measurements of the sound velocity. Different methods were used to calculate the velocity of sound in suspensions. One was to correct the velocity of sound in clear water, calculated with the equation of Chen and Millero (1977), for the SPM concentration with the correlation factor derived from the laboratory experiments. This method underestimated the effect of SPM on the sound velocity, so that the obtained sound velocities were too high. Another approach was to calculate the sound velocities with a two-phase model, also used by Vsemirnova et al. (2012) for the simulation of a seismogram of a turbid layers. This method overestimated the influence of SPM on the sound velocity, i.e. the obtained values were too low. A third method was the application of a scattering-model. Mobley et al. (1999) achieved good agreements between the results of this model and measurements in a suspension consisting of water and polystyrene beads. They also found out that the velocity of sound is dispersive in such solutions. A dispersion of the sound velocity was not predicted by the model for the suspension examined in this study, at least in a frequency range between 0 and 1000 kHz.
The differences between the calculated and the measured values of the sound velocity were properly caused by using the mechanical properties of quartz for the computations. Although, quartz was the most frequent mineral of the fluid mud in the Ems estuary, as shown in chapter 4.1. In estuaries and adjacent coastal water, most of the SPM don't consists of single dissolved minerals but of aggregates of these primary particles (Eisma, 1986). As shown by the laser analyzes the solid parts of fluid mud samples consist of clay and silt, which are terrigenous sediments (Hayter and Mehta, 1986). These particles have a complex surface charge distribution with a negative net charge, leading to repulsion between each other (Huang et al., 2012). Dissolved salt ions counteract this electrical repulsion so that aggregation of the particles becomes possible (Thill et al., 2001). Additionally, organic slime, produced by bacteria in the fluid mud, sticks single dissolved particles together. These two processes lead to aggregation and flocculation. The mechanical properties of the flocs are different than those of quartz, because they are at least a two-phase system consisting of quartz minerals and organic slime. The structure determines the mechanical properties, e.g. density and compressibility of the mud (Kranenburg, 1994). However, their mechanical properties are generally unknown and varying due to their various structures and sizes, which can reach values of up to 1000 µm in diameter (van der Lee, 2000). However, flocculation is an interaction between growing and decaying processes, depending strongly on the hydrodynamic conditions,

e.g. flow velocity and turbulence (Safak et al., 2013; Mikeš, 2011; van Leussen, 2011; Mietta et al., 2009; van der Lee, 2000). Thus, the flocs sizes in the experimental runs differed form those during the field measurements in the Ems estuary because of the different hydrodynamic conditions. Hence, the influence of flocs in the synthetic suspensions was differently strong compared to the influence of flocs in the fluid mud layer of the Ems estuary, because of their different structures and size distributions.
If the acoustical properties of the flocs were known, the two presented models would be applicable. An inversion of such a model comprises the possibility to determine fluid mud properties, e.g. SPM concentration, by measuring the sound velocity. SPM concentrations are normally determined by filtration of water samples or by optical methods, e.g. optical backscatter or laser transmission. However, all of these methods have inherent disadvantages: water samples can only be taken at discrete water depths and their filtration must be done later on in the laboratory and is time-consuming. A real-time determination of SPM concentrations is not possible. Optical methods enable the real-time profiling measurements, but the devices will be saturated in high concentrated layers (Traykovski et al., 2000).
The simulated reflectivities of lutoclines (Fig. 4.15.a), revealed a strong dependence on the signal frequency. Low frequencies had higher reflectivity coefficients than high frequencies. This is caused by the finite width of natural lutoclines and pycnoclines. Therefore, the change of acoustical impedance per wave length depends on the frequency and gets greater the lower the signal frequency is. A lutocline becomes detectable by hydro-acoustic methods if the ratio p_{scat} to p_{inc} is higher than the signal to noise ratio of the transducer (Ross and Lavery, 2012).
Additionally, the depth of maximum backscatter was simulated with the same model. The results showed that the echo depths also depend on the signal frequency (Fig. 4.15.b). This has to be taken into account when comparing different records of a lutocline, taken with hydro-acoustics differing in signal frequency.

4.2.6 Conclusions

In this study, the influence of SPM on the sound propagation, particularly on the sound velocity, were investigated. For this, results of laboratory, field and numerical measurements were combined and compared against each other. In the final part, the reflectivities of natural lutoclines, which were observed during a field trip in the German Ems estuary, were simulated with a weak-scattering model. From these investigations, the following conclusions were gained:

1. The speed of an ultrasonic wave is reduced by the presence of SPM, which could be observed in the field as well as during the laboratory measurements. The correlation between wave speed and SPM concentration is linear.

2. The reduction coefficient depends on the structure of the flocs, e.g. the greater the flocs, the lower the acoustical wave speed.

3. Due to the unknown mechanical and acoustical properties of the mud flocs, a numerical calculations of the sound velocity fails. Therefore, a characterization of suspension via the sound velocity is not yet possible.

4. The simulation of the backscattering ability of sediment-induced interfaces is possible with a weak-scattering model if the necessary parameters, i.e. sound velocity and density are known.

5. The strength of the echo depends on the width of the lutocline as well as on the signal frequency. The same applies for the depth of strongest echo.

Therefore, further investigations on the acoustical properties of natural muds and flocs, e.g. the development of a scattering-model for flocs, are recommended. An inversion of such a model would yield the ability to derive fluid mud properties, like SPM concentrations and grain-size distributions, from sound velocity measurements. This would allow the online determination of these parameters even in high concentrated layers, where conventional optical method break down.

4.2.7 Acknowledgments

We would like to thank the crew of FK Senckenberg for their assistance and patience during the Ems survey. Alexander Bartholomä and Jens Boczek are thanked for their help on board. Stephanie Peters is gratefully acknowledged for filtering the water samples. This study was financed by Deutsche Forschungsgemeinschaft in the frame of the Cluster of excellence “The Future Ocean”.

4.3 Summary and conclusion of chapter 4

In this chapter, the deployment of some common oceanographic methods in turbid water layers were examined. Firstly, the performances of electric conductivity sensors in turbid waters were investigated. For this, suspensions of different SPM concentrations and salinities were set up in the laboratory. Salinities of these suspensions were measured with two devices with different cell design. The measured salinity values were compared with reference run measurements in clear water. The absorption of salt ions by clay minerals was additionally analysed.
Secondly, the reflection of sound waves at sediment-induced interfaces within the water column was examined. This study consisted of two parts: the investigation of the influence of SPM on the sound velocity and the hydro-acoustic reflectivity of lutoclines. The first part comprised experiments, carried out in the laboratory and in the field, as well as calculations with different mathematical approaches. The second part implied the simulations of the acoustic reflection coefficients of natural lutoclines.
The following conclusions were drawn from the two validation studies:

- SPM concentrations above 10 g l^{-1} disturbed conductivity-based salinity measurements in a way that the recorded salinity values were lower than the adjusted salinities.

- The differences between measured and adjusted salinities increased proportionally to the SPM concentrations. A deviation of up to 30 % was observed at a SPM concentration of 300 g l^{-1}.

- Care should be taken when interpreting salinity values which were measured in turbid water layers.

- More accurate salinity values will be obtained, if conductivity is measured in collected water samples after SPM has been settled.

- The influence of SPM on salinity measurements may be neglectible for concentrations below 10 g l^{-1}, depending on the requested accuracy. This should be the case for most measurements on the shelf and especially in the open oceans, since the SPM concentrations there are clearly below 1 g l^{-1}.

- Adsorption of salt ions by charged clay minerals were responsible for about only 20 - 25 % of the observed salinity deviations.

- Erroneous salinity measurements in fluid mud layers were ascribed to a "blinding" of the sensor by the SPM: The dissolved solid particles and the agglomerations of single particles decreased the cross section of the virtual conductor between the measuring electrodes. This resulted in a lower electrical current flow, which was mistaken as a lower conductivity, and congruously as a lower salinity.

- The cell geometry had no recognisable effect on the observed error.

- SPM affected also the sound propagation in fluids. The velocity of sound in water decreased with increasing SPM concentration. This effect could be observed in the laboratory as well as in the field.

- A linear correlation factor between sound velocity and SPM concentration was derived from the laboratory measurements. It amounted to -0.035 m s^{-1} $(g\ l^{-1})^{-1}$.

- SPM had a higher influence under natural conditions, meaning that the sound velocity was stronger reduced by SPM in the field than in the laboratory. Values of the sound velocity calculated with the laboratory correlation factor didn't match the values measured in the field.

- The correlation factor between the velocity of sound in fluids and the SPM concentration most probably depends on the size and structure of the agglomerated particles.

- A published weak-scattering model could be adapted to simulate reflection coefficient of natural lutoclines.

- The echo strength as well as the depth of the most pronounced echo depended on the lutocline width and on the acoustic wave length. In general, the echo strength was higher for lower frequencies. The depth of the most pronounced echo varied with the frequency by several decimeter.

5 Evolution of internal waves in the Ems estuary

In this chapter, the studies concerning the IWs in the Ems estuary are presented. Special focus was placed on the processes leading to IW generation and breaking, as well as on the contribution of IWs to vertical exchange.

5.1 Generation and evolution of high-frequency internal waves in the Ems estuary, Germany[1]

P. Held[a], K. Schrottke[a], A. Bartholomä[b]

[a] Cluster of Excellence "The Future Ocean", Institute of Geosciences at Kiel University, Otto-Hahn-Platz 1, 24118 Kiel, Germany

[b] Senckenberg Institute, Department of Marine Research, Südstrand 40, 26382 Wilhemshaven, Germany

5.1.1 Abstract

The breaking of internal waves (IWs) is one of the most important factors for the vertical mixing of suspended sediments and nutrients in estuaries. Information on the generation and evolution of IWs in such environments is therefore required to better understand their physics and related processes of sediment transport. New data on highly resolved IWs recorded in the turbidity maximum zone of the Ems estuary (Germany) have provided new insights into the dynamics of estuarine IWs.

To investigate the generation and evolution of IWs as well as their contribution to vertical mixing, a variety of hydro-acoustic devices was deployed in combination with a vertical sampling of suspended particulate matter. Wave parameters such as significant wave height, wave frequency, wave length and steepness were computed from these data. The hydro-acoustic data reveal the formation of a prominent lutocline during slack water, at which IWs begin to be generated with the onset of tidal forcing. The two water bodies, which are characterised by markedly different suspended sediment concentrations, show clear differences in flow behaviour. As a consequence of current shear along the lutocline, Kelvin–Helmholtz instabilities are generated, which then produce IWs. The IWs break when high shear stresses between the two layers are coupled with great wave steepness, and the breaking causes vertical mixing of the sediment. Most IW breaking events occur during the decelerating ebb phase and thereby promote downstream sediment transport.

[1] This article was published in Journal of Sea Research, 2013, Vol. 78, p. 25-35

5.1.2 Introduction

Internal Waves

Internal waves (IWs) are a common phenomenon in stratified fluids (Adams Jr. et al., 1990). Stratification is ubiquitous in natural fluids and occurs in lakes, rivers, oceans, coastal seas (e.g., estuaries) and in the atmosphere, being caused by variations of fluid density with depth. Fluid density can change either progressively due to gravity and the resultant hydrostatic pressure of the overlying fluid layer or abruptly at pycnoclines, which are interfaces between fluid layers having different densities. Because density, among others, depends on temperature, salinity and the concentration of particulate matter (SPM), the abrupt change of one of these variables can result in the formation of a pycnocline. In correspondence with these two types of stratification, two types of IWs can be distinguished. In continuously stratified fluids, IWs propagate at a certain angle to the vertical (LeBlond, 2002). In this case, the highest attainable wave frequency is the corresponding Brunt–Vaisala frequency (N):

$$N = \sqrt{\frac{-g}{\rho}\frac{\partial \rho}{\partial z}} \tag{5.1}$$

where g is the acceleration due to gravity, z is the height of the water column, and ρ is the density. At a pycnocline, by contrast, the density gradient $\partial\rho/\partial z$ approaches infinity. IWs propagating along pycnoclines can therefore have arbitrary frequencies and can be characterised by the following dispersion relation:

$$\omega^2 = gk\frac{\rho_2 - \rho_1}{\rho_2 \coth(kd_2) - \rho_1 \coth(-kd_1)} \tag{5.2}$$

where k is the wave number and ρ_1, ρ_2 and d_1, d_2 are the densities and depths of the upper and lower layers, respectively. Surface gravity waves are a special case of IWs because air is a fluid of negligible density. Setting ρ_1 to zero yields the corresponding dispersion relation for surface waves.

IWs in natural waters occur within a wide range of periods (Adams Jr. et al., 1990). Due to smaller density differences between two adjacent water layers, IWs can attain higher amplitudes than waves at the water surface (Rao et al., 2010). Several mechanisms of IW generation are known, the most important being tide–topography interactions (e.g. D'Asaro et al., 2007; Nakamura and Awaji, 2001), wind (e.g. Vilibić et al., 2004), surface waves (e.g. Maxeiner and Dalrymple, 2011; Traykovski et al., 2000), shear instability

(e.g. Wang, 2006), decelerating river plumes, and resonance effects (Baines, 1995). A concise treatment of IW generation caused by flows over topography, decelerating river plumes and resonance effects can be found in Groeskamp et al. (2011).
Highly concentrated near-bed sediment suspensions (fluid mud), which are generally composed of fine-grained particles and organic matter, often occur in estuaries and other energetic coastal waters. In these environments, suspended sediment concentrations (SSC) can reach tens to hundreds of g l^{-1} and thicknesses of up to several metres, as, for example, recorded in the Weser estuary by Schrottke et al. (2006). A generally accepted SSC for the transition from water to fluid mud is 10 g l^{-1} (Kineke and Sternberg, 1995; Kirby, 1988; Manning et al., 2010; McAnally et al., 2007; Ross and Mehta, 1989). Fluid mud is often associated with a strong SSC gradient (McAnally et al., 2007), known as a lutocline. A lutocline is also a pycnocline, as fluid mud has a higher density than water. IWs propagating along a lutocline can achieve amplitudes of several metres (Traykovski et al., 2000).
Vertical mixing is an important process for the exchange and transport of nutrients and sediments. In general, vertical mixing is inhibited or at least reduced by a stable stratification (Bouruet-Aubertot et al., 2001). In such stably stratified systems, turbulence and, hence, vertical mixing can be caused by breaking IWs (D'Asaro et al., 2007; Wang, 2006). IWs are therefore a major mechanism for vertical mixing in the ocean interior (Birch and Sundermeyer, 2011). In the case of estuaries, IWs seem to play an essential role in SPM dynamics. However, very few studies to date have been able to document the generation and breaking of IWs in turbid estuaries at a high temporal and spatial resolution.
In this paper, high-resolution hydro-acoustic records of a lutocline in the Ems estuary, Germany, are presented. These records show the generation, growth and breaking of IWs. On basis of these data, and together with simultaneous SSC and flow speed measurements, parameters such as wave height, wave steepness and shear stress were calculated to document the dynamics of an estuary affected by IWs.

Regional setting

The coastal-plain estuary of the river Ems is located at the North Sea coast of northwestern Germany, close to the Dutch border (Fig. 5.1). The estuary can be subdivided into a lower funnel-shaped section between Pogum and the open North Sea, which also includes the adjoining Dollart tidal basin, and an upper channelised section between Herbrum and Pogum. The estuary has been highly impacted by human activities related

to economic development. Repeated dredging of the mainnavigation channel is needed to maintain a navigable depth of at least 5.7 m at a low-water spring tide (Schuchardt et al., 2007). The bathymetry of the river thus continuously changes in space and time (Chernetsky et al., 2010). The Ems estuary falls within the upper mesotidal category controlled by semidiurnal tides, with a marked spring-neap tidal cyclicity. The tide-influenced section has a length of approximately 100 km, stretching downstream from the island of Borkum to the weir at Herbrum (Spingat and Oumeraci, 2000). The estuary is flood-dominated (de Kreeke et al., 1997), with a mean tidal range of 2.25 m near Borkum and 3.1 m at Emden (de Jonge, 1992; van Leussen, 1999). Jens Jürgens and Norbert Winkel (2003) report a maximum tidal range of 3.8 m. It is a partially mixed estuary (van Leussen, 1999), the salinity decreasing from approximately 30 to 1 over the 60 km distance between Borkum and Leer (de Jonge, 1992). Upstream from Leer, brackish water conditions can only be found during low-water slacks and low river discharge (Spingat and Oumeraci, 2000). Depending on the literature source, strong temporal variations in river discharge are indicated (de Jonge, 1992), ranging from 25 to 380 m^3s^{-1} (van Leussen, 1999) to 30 to 300 m^3s^{-1} (de Kreeke et al., 1997).
Accordingly, the current velocities in the Ems are highly site-specific and variable, but generally decrease slightly downstream from a maximum of 1 m s^{-1} during times of high river discharge (Spingat and Oumeraci, 2000).
The Ems estuary is well known for its high SPM concentrations, which have dramatically increased over the recent decades, as already reported by de Jonge (1983). SSCs of up to 1.6 g l^{-1} have been reported by Wurpts (2005). The estuary exhibits a well-developed turbidity maximum zone (TMZ) that extends over a distance of more than 60 km (de Kreeke et al., 1997). Fluid mud is regularly observed throughout the TMZ during slack water, but it varies in spatial distribution and thickness. Talke et al. (2009) observed 1–2-m-thick fluid mud deposits in the upper estuary, with SSCs of 10–80 kg m^{-3}.

5.1.3 Measurements and methods

Measurement setup

Water depths and fluid interfaces within the water column were recorded using the parametric Sediment Echo-Sounder SES-2000® standard of Innomar Technology GmbH (Rostock, Germany). This device has a high vertical resolution (<6 cm) and accuracy, e.g., 100/10 kHz: 2/4 cm +0.02% of the water depth (Wunderlich and Müller, 2003).

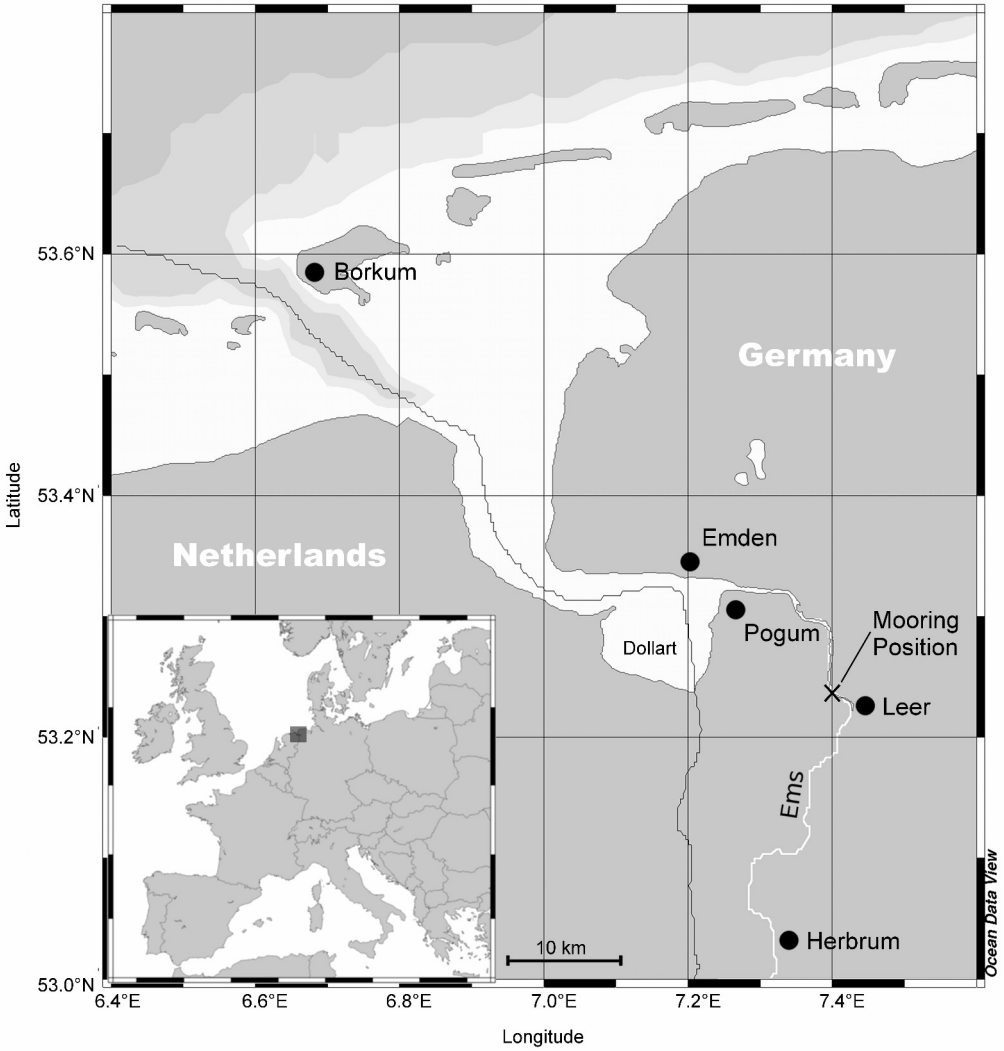

Figure 5.1: Map of the Ems estuary together with the mooring position of RV Senckenberg.

Both the primary frequency of 100 kHz and a selected secondary frequency of 12 kHz deliver the most accurate depth information. Due to its higher sensitivity to small changes in acoustic impedance, the high-frequency channel was used to extract the depth of the first pronounced interface. The water depth (distance from the water surface to the consolidated riverbed) was measured at the 12 kHz frequency because of its lower attenuation in turbid water. The transducer was firmly mounted on the portside of the research vessel at a depth of 1.6 m below the water surface. Ship movements (heave, roll, pitch and heading) were compensated for by a motion sensor (Seatex® MRU-6).
A Seabat 8125 multibeam echo-sounder (MBES) by Reson™, with a working-frequency of 455 kHz and 256 beams, was used to detect the lutoclines. The MBES transducer was installed on the same mounting pole as the SES, but at a water depth of 1.8 m. According to the manufacturer, the MBES achieves a depth resolution of 0.06 m. Ship movements were compensated for by using an Octans™ Surface (IXSEA OCEANO) gyrocompass and motion sensor.
An RDI-Teledyne™ 1200 kHz Workhorse Acoustic Doppler Current Profiler (ADCP) was used to measure the flow speed. The ADCP was installed in a rigid frame attached to the starboard side of the vessel at a depth of 1.35 m below the water surface. A 0.25 m cell size with a blanking-zone of 0.50 m was selected for the ADCP measurements. Ensembles of flow speed and direction were provided at time intervals of 2.33 s. The standard deviation of the measured flow speeds was 0.129 m s^{-1}.
A horizontal water sampler (HydroBios©) with a sampling volume of approximately 2 l was used to collect water samples. A fin aligned the water sampler with the current. Water samples were taken 1 m above the consolidated riverbed and 1 m below the water surface six times. The SSC values were extracted as dry masses per unit water volume. For this purpose, an aliquot of each water sample was vacuum filtered through glass fibre filters having a pore diameter of 1.2 µm.

Mooring position

Stationary measurements were taken in the channelised section of the Ems estuary at 53°14'10.0"N, 007°23'50.6"E (Fig. 5.1). This position is in the freshwater zone of the Ems estuary. During the measurements, the research vessel (RV Senckenberg) was moored between two piles on the western side of the navigation channel, with the bow facing in the upstream direction.
The measurements were taken from 2051 UTC 3 September 2008 to 0255 UTC 5 September 2008. Starting with a flood tide, three flood and two ebb tidal cycles were covered

by the measurements. The previous spring tide occurred on 30 August and the following neap tide on 7 September 2008. During the measurement period, the mean river discharge at Versen was 38.7 m^3s^{-1} (source: Wasser- und Schifffahrtsamt Meppen/2012).
A second dataset was collected from 1500 UTC 18 June 2007 to 1129 UTC 19 June 2007, covering two ebb and one flood tidal cycles. The previous spring tide occurred on 15 June and the following neap tide on 22 June 2007. The mean river discharge was 60.8 m^3s^{-1} (source: Wasser- und Schifffahrtsamt Meppen/2012).

Data analysis

The depth of the lutocline was extracted from the SES records by means of the capture mode of the SES software ISE 2.9. This method implies an estimated error for the depth values of approximately ±0.1 m. The MBES signal is reflected directly by the lutocline. The time series of SES and MBES are both averaged over 1 s.
A Fast Fourier Transformation (FFT) was applied to the data to extract the frequencies of interface undulations. For this computation, the freely available C library FFTW (Fastest Fourier Transformation in the West; (Frigo and Johnson, 2005)) was used. An interval of 1024 sampling points was chosen for the FFT. Due to the previous averaging, this corresponds to an interval length of 1024 s, with an error for retrieved frequencies of $\Delta f = 1/1024\ s = 0.0010\ s^{-1}$. Noise and linear trends in the signal were removed by applying a bandpass filter. After each FFT, the interval was shifted by a time step of 600 s.
The significant wave height was calculated from the vertical displacements of the interface visible in both the SES and MBES records. The significant wave height is defined as the average of the highest one-third of waves recorded over a certain time interval. In this study, a time interval of 10 min was chosen.
The wave steepness, which is the ratio of the height to the length of a wave, was also calculated from the SES time series. Whereas wave heights could be directly measured, wave lengths had to be calculated using the dispersion relation because the vessel was moored at a fixed position. For this purpose, the current speed U had to be implemented in Eq. 5.2. The dispersion relation then becomes:

$$\left(\frac{2\pi}{T} \pm \frac{2\pi}{\lambda}U\right)^2 = g\frac{2\pi}{\lambda}\frac{\rho_2 - \rho_2}{\rho_2 \coth(\frac{2\pi}{\lambda}d_2) - \rho_1 \coth(\frac{-2\pi}{\lambda}d_1)} \tag{5.3}$$

where T is the wave period, here taken as the time between the passage of two adjacent wave crests in the SES records. The densities ρ_i are estimated via the bulk density

relation:

$$\rho = \rho_W + SSC\left(1 - \frac{\rho_W}{\rho_S}\right) \tag{5.4}$$

where ρ_W is the density of water and $\rho_S = 2650$ (g l $^{-1}$) is the sediment density (Guan et al., 2005). For this estimate, the SSCs of all samples from one layer were averaged.
Flow velocities were retrieved from the ADCP measurements. Several difficulties can arise when using ultrasonics in fluid mud, e.g., multiple scattering and attenuation of sound. Gratiot et al. (2000) showed in a laboratory study that multiple scattering of the signal in fluid mud did not invalidate velocity measurements of an acoustic Doppler velocimeter with a working frequency of 5 MHz because the multiple scattered echo is attenuated so much that it is below the threshold of the receiver. These experiments were carried out for SSCs ranging from 20 g l^{-1} to 200 g l^{-1}. Although a different working frequency was used in this study, it was assumed that the ADCP measurements were similarly reliable or, at the very least, gave a reasonable estimation of fluid mud movement. Variations in the speed of sound with depth do not affect measurements of the horizontal component of the flow velocity because changes in sound speed and the refraction of the signal compensate each other. From the ADCP measurements, the depth-averaged flow speed, i.e., the average of the horizontal velocity components in each cell over the covered part of the water column, was calculated. To compare the flow behaviour of water and fluid mud, the mean flow speeds of the two layers were computed separately. Oscillations in the depth averaged flow speed were also subjected to Fourier analysis. For this purpose, 512 sampling points (corresponding to a time interval of 1193 s) were used for each FFT interval to achieve a similar temporal resolution as for the SES and MBES data. Here, the error of retrieved frequencies was Δf=1/(2.33*512 s)=0.0008 s^{-1}. Again, the FFT was repeated every 600 s of the time series, the extracted frequencies being subsequently bandpass filtered.
The frequency spectra of the MBES, SES and ADCP time series were compared to ensure that the oscillations found in the different time series were comparable and caused by the same phenomenon. Therefore, each frequency spectrum was searched for the three highest peaks. The best-matching peaks of two frequency spectra were then compared.
The flow behaviour of the combined water-fluid mud system was estimated via the Froude number, which, for a two-layer flow, reads (Dalziel, 1991):

$$G^2 = F_1^2 + F_2^2 = 1 + \frac{d_1 + d_2}{d_1 d_2 g'} c_+ c_- \tag{5.5}$$

where g' is the reduced gravity $g' = g(\rho_1 - \rho_2)/\rho_2$, c_+ and c_- are the phase speeds of a long IW propagating in either the upstream or downstream direction. The phase speed in a two-layer system is (Baines, 1995):

$$c_\pm = \frac{u_1 d_2 + u_2 d_1}{d_1 + d_2} \pm \left(\frac{g' d_1 d_2}{d_1 + d_2}\right)^{1/2} \left(1 - \frac{(u_2 - u_1)^2}{g'(d_1 + d_2)}\right)^{1/2} \tag{5.6}$$

where u_1 and u_2 are the flow speeds of the upper and lower layers, respectively. If c_- vanishes, $G^2 = 1$ and the flow becomes critical.

5.1.4 Results

Suspended sediment concentration

During the survey of 2008, the SSCs measured 1 m below the surface varied between 0.491 ±0.002 g l^{-1} and 2.21 ±0.02 g l^{-1} (mean 1.49 g l^{-1}). In comparison, the SSCs measured 1 m above the consolidated riverbed varied between 23.2± 0.8 g l^{-1} and 88.2 ±3.0 g l^{-1} (mean 57.5 g l^{-1}). The SSCs near the bottom were thus substantially higher compared with those in the upper water column. Based on this finding, the water column could, at the very least, be subdivided into an upper and a lower water layer, the values for the latter indicating the presence of fluid mud.

Fluid interface and internal waves

The occurrence of an interface within the 8–11 m deep water column is reflected in both the SES and MBES data sets. The depth of the interface below the water surface varies from 4 to 6 m. For most of the time, undulations and wave-like features can be observed at this interface. Only during high-water slacks is the interface smooth, apart from a few isolated wave packets. Such wave groups consist of three to four wave crests that are led by the highest wave with subsequent waves successively decreasing in height. The wave period is approximately 60 s. Before and after the passage of such wave packets, the interface is smooth. With the onset of the ebb current, the interface becomes disturbed and small undulations appear on the interface. These undulations grow in size with increasing current speed and eventually develop into wave-like structures. Significant wave heights of these IWs are shown in Fig. 5.2a. Maximum significant wave heights of 0.75 m, temporarily reaching 1.3 m, occur approximately 3 h after a high-water slack tide. Thereafter, the wave heights progressively decrease to approximately 0.3 m (Fig. 5.2a). During decelerating ebb currents, it was possible that the interface could temporarily

not be clearly detected in the SES or MBES time series. At these times, the upper layer becomes highly turbid and the interface vanishes in the SES data, as shown in Fig. 5.3. Altogether, 110 such events were identified in the SES time series (Fig. 5.2b, marked with black diamonds) of the 2008 survey. In the time series of 2007, by contrast, 146 such events were found (Fig. 5.4, marked with black diamonds).
Around low-water slack tides, the interface is no longer detectable. With increasing flood tide, wave heights again increase, with maximum significant wave heights occurring approximately 1 to 1.5 h after low-water slacks. After peaking, the wave heights again decrease and eventually disappear at high-water slack tide.

Frequencies of internal waves

The frequencies of IWs are shown in Fig. 5.5 for the time after low-water slack tide at 2135 UTC 3 September 2008 and for the time after high-water slack tide at 0315 UTC 4 September 2008. There are some differences in the evolution of the IWs after high- and low-water slack tides. Until 20 min after high-water slack tide, there is almost no energy in the frequency spectrum, the interface over this time interval being smooth. With the onset of tidal flow, low-frequency undulations develop first, accompanied by a slight tilting of the interface. With time, the energy increases and is distributed almost equally over the complete frequency range. Even 110 min after high water, no prominent peaks are visible in the frequency domain (Fig. 5.5c). The IW field consists of several superimposed waves with different periods.
During flood tide, by contrast, the frequency spectra look quite different. Thus, 20 min after the low-water slack tide, the highest peaks appear at low frequencies (Fig. 5.5d), indicating the presence of long-period undulations on the interface. At 120 min after low-water slack tide, four clearly defined peaks are visible (Fig. 5.5f). The undulations on the interface now mainly consist of four different IW systems. This means that the IWs show a more regular pattern during the flood tide compared with the ebb tide.

Wave steepness

For the calculation of wave steepness, it is assumed that IWs propagate in the downstream direction. This assumption is based on the observation that IWs are first generated during the ebb tide. The results of these calculations are shown in Fig. 5.2a. Around the high-water slack tide, the wave steepness is zero because there are no waves. Increasing wave heights are then associated with increasing wave steepness. During the ebb phase, the steepest waves appear before the highest ones, whereas during the flood

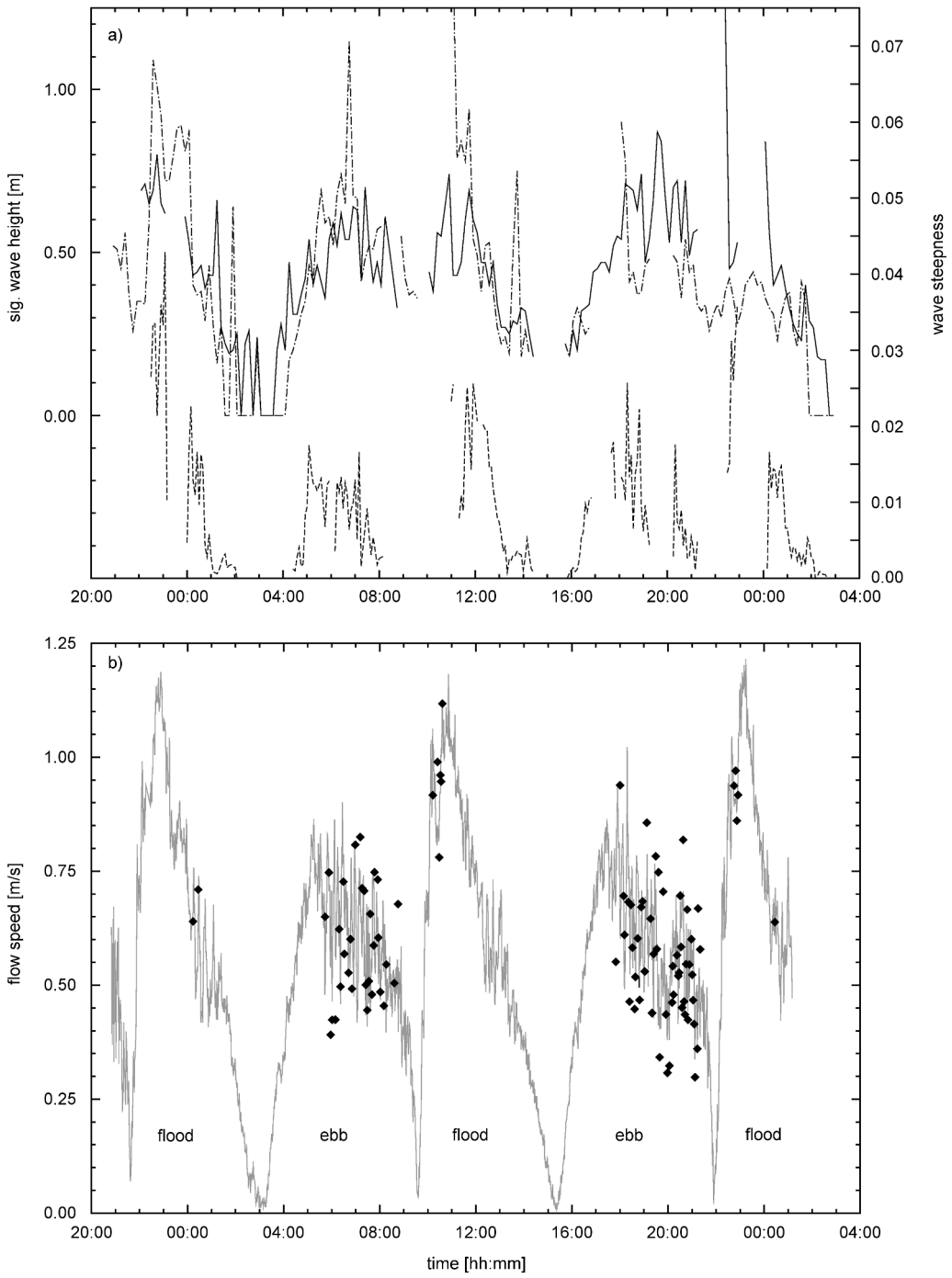

Figure 5.2: Significant wave heights retrieved from SES data (solid line) and MBES data (dot–dashed line) together with the calculated wave steepness (dashed line). The peaks of significant wave heights during the first HWS in a) are caused by trains of internal soliton waves. b) Tidal curve of the depth-averaged flow speed showing the observation times of IW breaking (black diamonds) in the period from 3 to 5 September 2008.

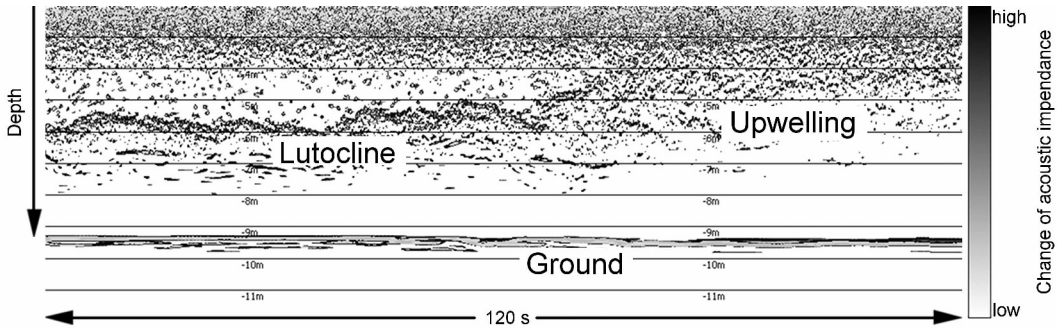

Figure 5.3: An example of IW breaking as seen on an SES record over a time sequence of 120 s. Wave motions on the lutocline are visible in the left part, whereas the whole water column is turbid and the lutocline has disappeared in the right part.

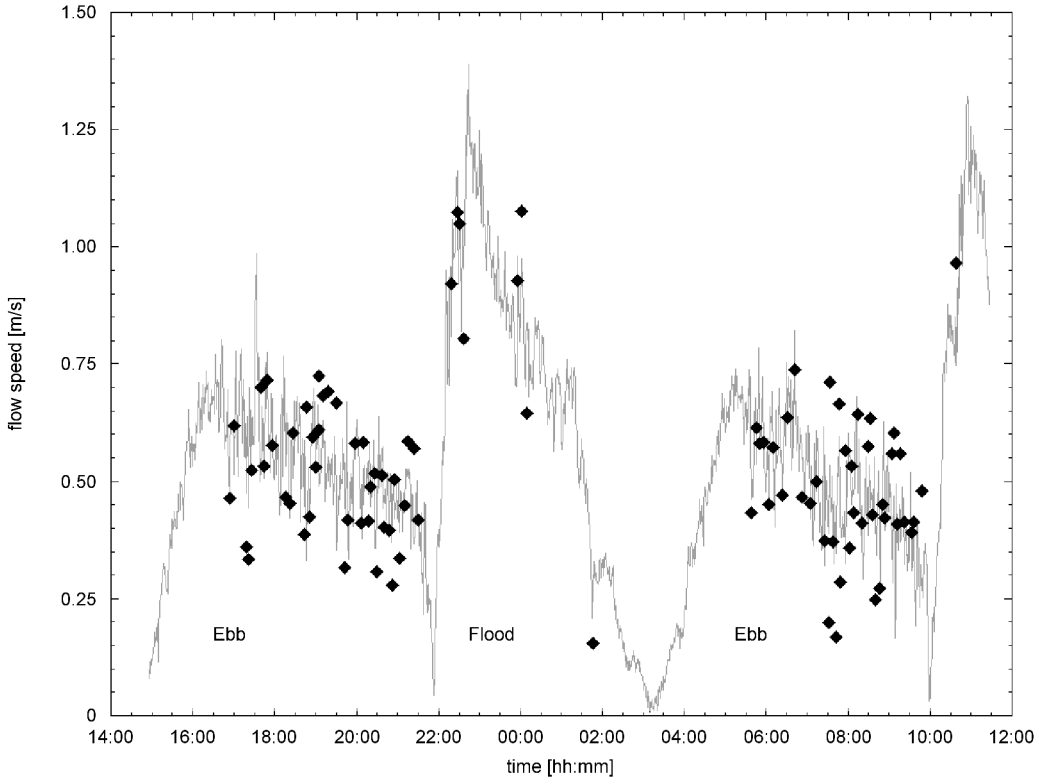

Figure 5.4: Depth-averaged flow speed showing the observation time of IW breaking (black diamonds) in the period from 18 to 19 June 2007.

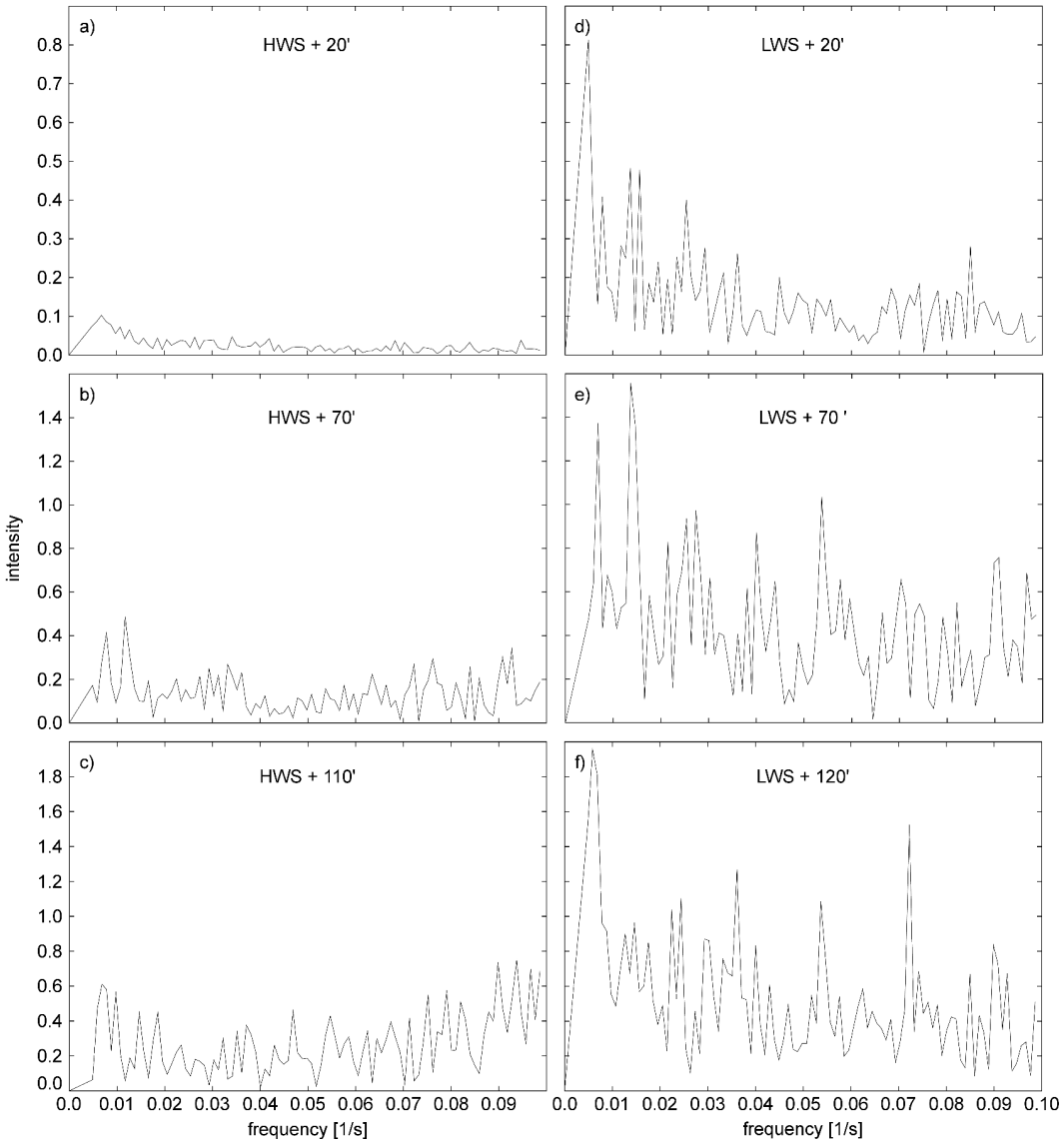

Figure 5.5: Spectra of 1024 s long sections of SES records of the lutocline for different times after high-water slack (HWS) (a, b, c) and after low-water slack (LWS) (d, e, f).

phase, the highest waves coincide with the steepest ones. The steepest waves, with a height to length ratio between 0.035 and 0.04, appear approximately 1 h after the low-water slack tide. Another peak in wave steepness occurs in the second half of the flood tide.

Flow speeds

At first, a flood-current dominance is clearly visible in the depth-averaged horizontal flow speeds (Fig. 5.2b). With maximum speeds of approximately 1.20 m s^{-1}, the flood current is stronger than the ebb current, which reaches maximum speeds of approximately 0.85 m s^{-1}. While the flood current increases faster than the ebb current, it is of shorter duration (340 min) than the ebb current (390 min). Furthermore, the low-water slack period is shorter than the high water-slack period.
The depth-averaged flow speed is marked by persistent oscillations (Fig. 5.2b). These oscillations occur over almost the complete tidal cycle but are more frequent after the strongest ebb current when they are very prominent for approximately 4 h. A second oscillation event occurs during the decelerating flood phase, which, however, persists for only approximately 1.5 h.
Current speeds are not uniform throughout the water column, as is demonstrated in Fig. 5.6 by the mean horizontal flow speed of the layer above the interface and that below. Differences in the flow speeds of the two layers can be distinguished in the course of a tidal phase. Starting at low-water slack tide, both layers are at rest. With the onset of the flood tide, they start to flow simultaneously in the upstream direction with similar flow speeds (dashed line in Fig.5.7b). Then, 45 min before the flood current peaks, the upper layer is temporarily overtaken by the lower one (dot-dashed line in Fig. 5.7b). Approximately 1.5 h after peak flow, the speed of the lower layer decreases more rapidly and remains lower than that of the upper one. At the high-water slack, tide both layers are at rest again. With the onset of the ebb tide, the upper water layer begins to flow downstream ahead of the lower one (Fig. 5.6) and also flows faster throughout the ebb tide (dashed line in Fig. 5.7a).
Another interesting feature is revealed when the flow directions of the two layers are considered. At times of marked oscillations in the flow speed, the two layers temporarily flow in opposite directions (dot–dashed line in Fig.5.7 a).

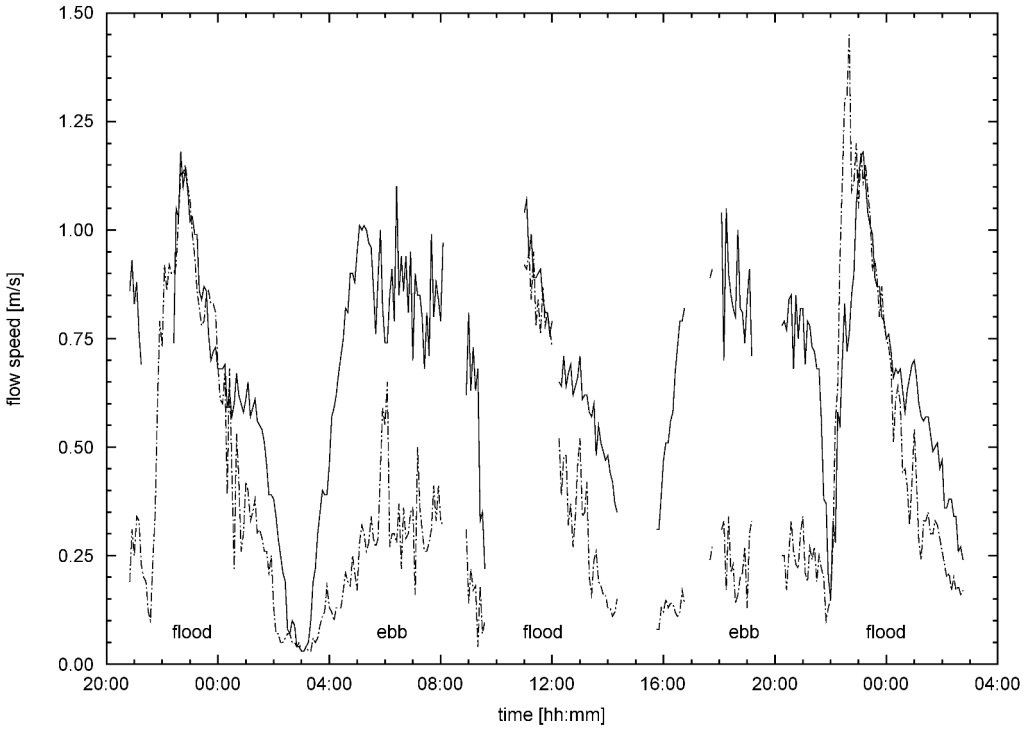

Figure 5.6: Flow speed of fluid mud (dot–dashed line) and upper water layer (solid line) in the period from 3 to 5 September 2008. Gaps indicate time intervals without data.

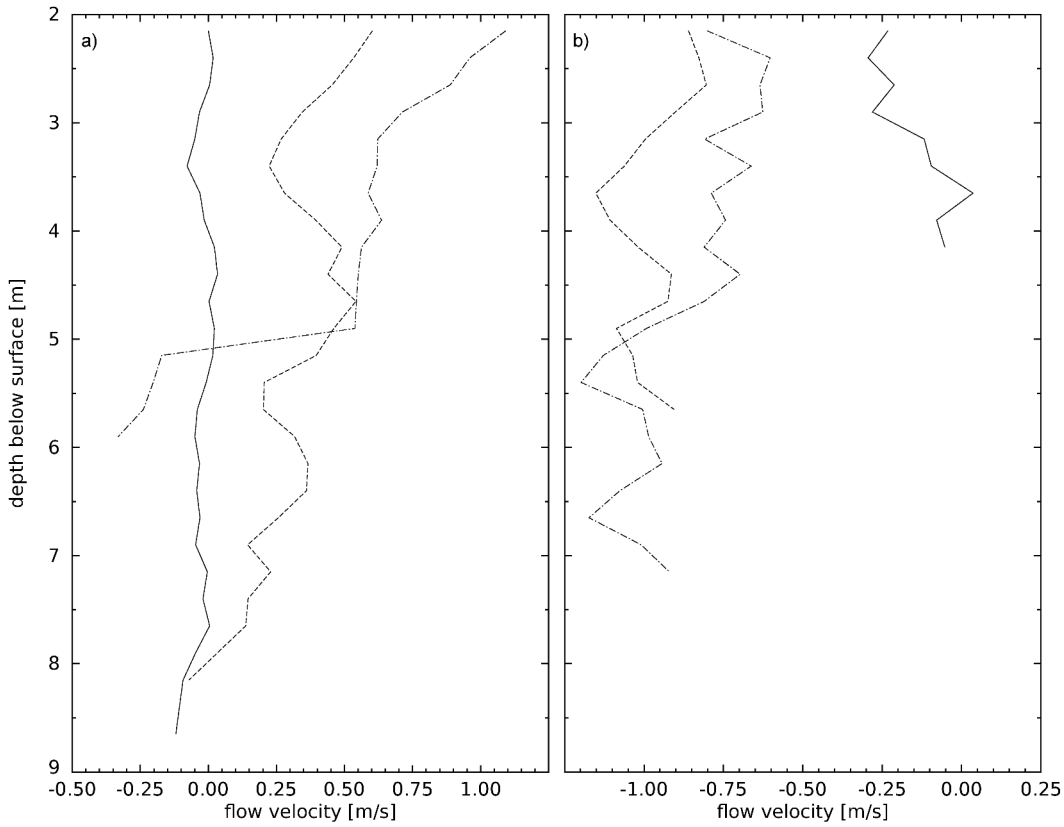

Figure 5.7: a) Selected profiles of horizontal flow velocity, HWS, at 0315 UTC 4 September 2008 (solid line), HWS + 45 min (dashed line) and HWS + 210 min (dot–dashed line). b) LWS at 2135 UTC 3 September 2008 (solid line), LWS + 45 min (dashed line) and LWS + 75 min (dot–dashed line).

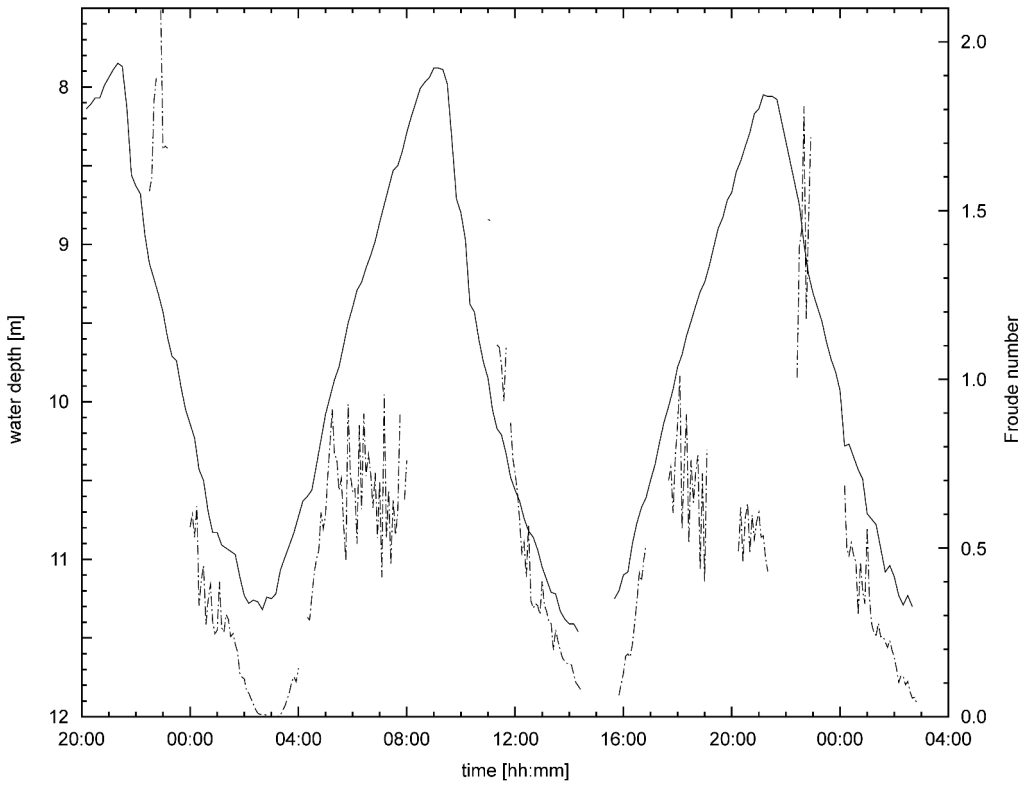

Figure 5.8: Water depth (solid line) and Froude number (dot–dashed line), showing times of sub- and supercritical flow in the period from 3 to 5 September 2008.

State of flow

The Froude numbers for the two-layer system relative to the tidal phase are shown in Fig. 5.8. During the ebb tide, the mean Froude number is 0.7, which means that the flow remains subcritical. Only at approximately 2.5 h after high-water slack tide does the Froude number temporarily reach nearly 1, indicating a brief critical state of flow. During the first half of the flood tide, by contrast, the flow is supercritical, which indicates that the flow crosses the critical regime twice in the course of a tidal cycle.

Frequency peaks of the FFT

The frequencies of interface undulations computed by the FFT from both the SES and MBES times series are in good agreement with each other (Fig. 5.9). The mean frequency deviation is 0.0005 s^{-1}. When the IW frequencies are compared with the frequencies of the oscillations of the depth-averaged current speed (Fig. 5.10), they again match quite well, with the mean frequency deviation being 0.0006 s^{-1}.

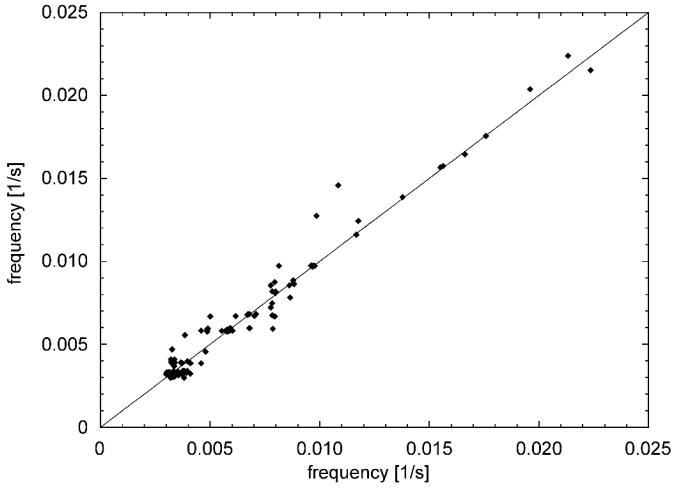

Figure 5.9: Scatterplot of IW frequencies extracted from SES (x-axis) and MBES (y-axis) time series.

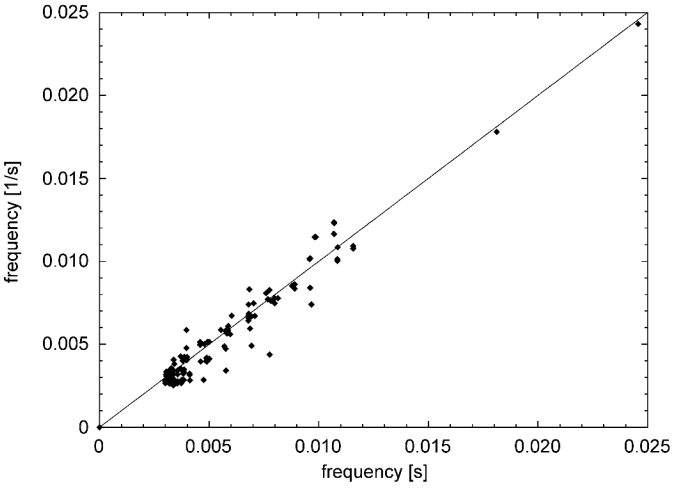

Figure 5.10: Scatterplot of IW frequencies extracted from SES time series (x-axis) and depth-averaged flow speeds of the ADCP data (y-axis).

5.1.5 Interpretation and discussion

At the measuring site in the fresh-water region of the Ems estuary, water stratification is caused by strong SSC gradients in the water column. Mean SSCs of 57.5 g l^{-1} within the lower layer indicate the presence of fluid mud with a thickness of several metres. The interface detected by the different hydro-acoustic systems can therefore be defined as a lutocline. The thickness of the fluid mud layer varied between 2 and 5.5 m during the measurement period.

Unfortunately, the lutocline was not continuously detected over the measuring period because it temporarily disappeared during the ebb tide when the fluid mud was mixed into the upper layer (Fig. 5.3). Additionally, no signal was received from the lutocline at low-water slack tide, most likely because the transducers of the SES and MBES were submerged in the fluid mud layer. Under such conditions, it is impossible to acoustically detect the lutocline.

From the data, it can be shown that oscillations of the depth-averaged flow speed and high IWs occur at the same time and with the same frequencies (Fig. 5.10). From this result, it can be concluded that fluctuations in the flow speed are caused by IWs. This assumption is consistent with the observations of (Adams Jr. et al., 1990), who also found that IWs were present in his velocity records.

Internal wave evolution

Ws first develop on the lutocline shortly after high water when the shear stress between the upper water layer and the fluid mud begins to increase. Approximately 1 h after the high-water slack, significant wave heights of 0.2–0.3 m are reached. A nearly critical flow is reached 2.5 h after the high-water slack tide. The highest IWs appear after the maximum ebb flow. At this time, the vertical shear remains nearly constant, and the fully developed wave field consists of several waves with different wave periods (Fig. 5.5a). Because the IWs develop before the flow becomes near-critical, it is concluded that the observed IWs are generated by excitation through Kelvin–Helmholtz instabilities rather than resonant flow conditions. This conclusion is supported by the fact that the IWs described in the literature that are generated by resonance are actually solitons, e.g., the IWs observed by Silva and Helfrich (2008) in the Race Point Channel (Gulf of Maine, USA) and by Groeskamp et al. (2011) in the Marsdiep channel (The Netherlands). In contrast, the IWs described in this study are generated by shear stresses between two fluid bodies. The IWs in the Ems estuary also differ from others observed in coastal

areas where they were mostly generated by the interaction of currents with topography (D'Asaro et al., 2007; Silva and Helfrich, 2008; Leichter et al., 2005; Nakamura and Awaji, 2001; Rao et al., 2010; Vilibić et al., 2004; Wang, 2006). Adams Jr. et al. (1990) also actually observed high-frequency Kelvin–Helmholtz billows superimposed on longer IWs. The long IWs in that case were generated in the lee of an obstacle, whereas the Kelvin–Helmholtz billows were generated by shear stresses at the crests and in the troughs of the long IWs.

The process of IW generation by tidal currents described in this study is similar to that of surface gravity waves, which are the product of interfacial shear instability (Miles, 1957). At first, small undulations (ripples) are produced by wind-induced stresses on the surface. Wind waves then progressively develop due to the continued interaction between wind and these initial ripples. The highest waves occur shortly after the wind forcing ceases. The fully developed wind seas consist of several waves with different wave periods.

The slight decrease in wave height towards low tide and the short duration of the low-water slack tide are evidence of the presence of undulations on the lutocline during slack water. IWs with significant wave heights of 0.3–0.4 m most likely propagate on the lutocline at the low-water slack tide. These IWs increase in height by 0.1–0.2 m during the following flood tide. Vertical shear stresses are negligible because both fluid layers have a similar velocity at that time. Maximum significant wave heights coincide with maximum flood currents. The MBES records show that the crests and troughs of the IWs are oriented nearly perpendicularly to the mean current direction. Four prominent peaks are visible in the frequency spectrum after the maximum flood current (Fig. 5.5f), which corresponds to a wave field essentially consisting of four wave systems, as it is more regular than the one found during the ebb tide. Significant wave heights decrease after the maximum flood current and, with the exception of some isolated wave packets, the IWs disappear from the lutocline when high-water slack tide is reached. As the flow passes from the subcritical to the supercritical regime before and after the time of maximum flood current, there is a possibility that IWs are generated by resonance at those times. The wave packets, in turn, only occur during high-water slacks and, on account of their progressive decrease in height, are interpreted as solitons that may have been generated as lee waves behind an obstacle somewhere else in the estuary.

Internal wave breaking

The lutocline temporally disappears from the hydro-acoustic records at several time intervals. As seen in the SES records, the lutocline during these time intervals rises towards the surface and finally breaks up (Fig. 5.3). These events are interpreted as IW breaking because fluid mud is mixed into the upper water layer; this also becomes visible at the water surface in the form of highly turbid clouds.
As shown in this study, high and steep waves with significant wave heights over 0.4 m and large shear stresses between two fluid layers are common conditions favouring the breaking of IWs. This phenomenon mainly occurs during ebb tide, when the ebb current is in the phase of deceleration. In addition, breaking events are also observed during the flood tide, i.e., approximately 45 min before it reaches its maximum speed and approximately 2.5 h before the high-water slack tide. Similar significant wave heights, wave steepness and vertical shear stresses are observed in all occasions when IW breaking takes place. Nevertheless, significantly fewer IW breaking events are observed during flood tides than ebb tides. It seems that the occurrence of breaking IWs is correlated with the thickness of the upper water layer. During the flood phase, the thickness of the upper layer is 6 m or more, whereas it is 5 m or less during the decelerating ebb tide. A correlation between the occurrence of IW breaking and the thickness of the fluid mud layer was not observed.
Fluid mud is mixed into the upper water layer when IWs break. After being mixed into the upper fluid layer, the sediment is transported within this faster flowing layer. IW breaking is hence linked with vertical mixing and the initiation of sediment transport. As more IW breaking events are observed during the ebb tide, the net sediment transport triggered by IW breaking is in the seaward direction.

5.1.6 Conclusion

SC and SES records show the presence of a lutocline in the river section of the Ems estuary. The lutocline defines the interface between the 2 to 5.5-m-thick layer of fluid mud and the overlying water column. The two layers show different responses to tidal forcing.
In this study, the behaviour of the lutocline in the course of a tidal cycle was investigated by the deployment of three different hydro-acoustic devices in combination with the collection of water samples from different water depths. All three devices revealed the same phenomenon. From the data, it can be concluded that the IWs observed in

this study are generated by the differential effect of vertical shear stresses across the lutocline.

In the Ems estuary, IWs are generated by shear instabilities along the lutocline during the ebb current phase. Significant wave heights of up to 1.3 m are reached. The IW field is more regular during the flood tide than during the ebb tide. Around the high-water slack tide, the lutocline is essentially smooth, whereas IWs are most likely still present on the lutocline during the low-water slack tide.

IW breaking is observed during both ebb and flood tide, but mainly during the decelerating ebb phase. The preconditions for IW breaking are steep waves with significant wave heights of at least 0.4 m together with large shear stresses between the two fluid layers. It seems that IW breaking is suppressed if the thickness of the upper layer exceeds 6.0 m.

IW breaking mixes fluid mud into the upper water layer and causes the downstream transport of sediment because IWs break more frequently during the ebb tide than the flood tide. In addition, during the ebb tide the upper water layer moves faster than the fluid mud layer. IW breaking is hence an important mechanism for the understanding sediment transport dynamics in waters characterised by sediment-induced stratification, such as highly turbid estuaries.

Acknowledgements

The authors would like to thank the captain and crew of "RV Senckenberg" for their excellent job and inexhaustible patience during the acquisition of the datasets for this study. Arnulf Möller from the Senckenberg Institute is thanked for his support onboard the ship and for the processing of the MBES data. Svenjy Papenmeier and various student assistants of the Institute of Geosciences at Kiel University are thanked for analysing the water samples. The Senckenberg Institute kindly provided the ship time. This study was funded by the Deutsche Forschungsgemeinschaft as part of the Cluster of Excellence 'The Future Ocean' and partly by the Research Center for Marine Environmental Sciences (MARUM). We would also like to express our gratitude to Mr. Burghard Flemming for the language corrections. Finally, the authors would like to thank the reviewers for their constructive criticism.

5.2 Generation and breaking of internal waves on a lutocline in the Ems estuary (Germany) and their contribution to vertical mixing

5.2.1 Abstract

Internal waves are an ubiquitous phenomenon in natural fluids. Turbulence, caused by breaking of internal waves is one of the main reasons for vertical mixing of stratified oceanic and coastal waters. Thus, they play a key role for the vertical exchange of sediment, nutrients and other dissolved substances. Internal waves in coastal waters are mostly generated at locations, where water masses overflows topographic obstacles. In the tide-dominated Ems estuary, internal waves arise from Kelvin-Helmholtz instabilities as stated in this study, based on new detailed hydro-acoustic data.
In this estuary, the generation of internal waves starts during the accelerating ebb phase. At the beginning of the ebb phase, when small undulations occur on the lutocline, the shear stress on the lutocline rises and the gradient Richardson number falls below 0.25. It then takes about 81 minutes from the occurrence of the first undulations to the first internal wave breaking. Breaking of these waves is not triggered by wave steepness nor by the Reynolds number.
Internal wave breaking on the lutocline contributes to vertical mixing as it could be seen by a widening of the lutocline. The corresponding squared Brunt-Väisälä frequency at the lutocline will be reduced by up to 60 percent, indicating a decrease of the stratification.

Keywords: Kelvin-Helmholtz instabilities, shear stress, Reynolds number, Richardson number, wave steepness

5.2.2 Introduction

Internal waves (IWs) are a common feature at stratified water masses of oceans, coastal waters and even in the atmosphere. Their breaking is one of the main sources of turbulence and mixing processes in the oceans interior (Birch and Sundermeyer, 2011). Thus, IWs may lead to sediment resuspension and transportation, but related processes are still poorly documented (Pomar et al., 2012).
A disturbance of the hydrostatic equilibrium between gravity and buoyancy results in an

oscillation within the medium. If, for example, a fluid body is moved in a region where the surrounding medium has a different density, it will be forced back by its buoyancy and will oscillate around its equilibrium position. The higher the density gradient is, the higher is the corresponding buoyancy frequency N:

$$N = \sqrt{-\frac{g}{\rho}\frac{\partial \rho}{\partial z}} \tag{5.7}$$

here g is the acceleration due to gravity, ρ is the density and z is the vertical coordinate in upward direction. The buoyancy frequency is also known as Brunt-Väisälä frequency. In cases where background currents are present, this disturbance propagates as IW. Depending on the ratio of the forcing to the buoyancy frequency, IWs propagate at a certain angle to the vertical in continuously stratified fluid LeBlond (2002). In the presence of a discontinuity in the stratification, such as an interface between fluids of different densities IWs will propagate along this pycnocline. Such IWs can be characterized by the following dispersion relation:

$$\left(\omega^2 \pm kU\right) = gk\frac{\rho_2 - \rho_1}{\rho_2 \coth(kd_2) - \rho_1 \coth(kd_1)} \tag{5.8}$$

where ω is the angular frequency, $k = 2\pi/\lambda$ is the wave number, U is the background flow velocity, ρ_i and d_i are the densities and depths of the upper and lower fluid respectively. Due to the small density differences between two layers in the ocean or in the atmosphere, IWs can attain higher amplitudes than waves on the ocean surface (Rao et al., 2010). For the same reason the phase velocity of IWs is smaller (Pomar et al., 2012).
According to literature the main reason for the generation of IWs is the interaction of a stratified flow with topography (Sutherland et al., 2000). Topographic obstacles can be are for example continental shelf edges (e.g D'Asaro et al., 2007; Huthnance, 1989), straits (e.g. Brandt et al., 1996) and deep ocean ridges (e.g Konyaev et al., 1995). For a concise treatment of IW generation caused by flows over topography see Groeskamp et al. (2011). Underwater dunes are an example for estuarine obstacles, triggering the generation of IWs. Even in the atmosphere, mountain regions are the main source for IW generation as found by (Nastrom and Fritts, 1992). Topography-induced IWs are normally solitary-like. Other sources for IW generation are amongst others wind (e.g Vilibić et al., 2004; Kantha, 1979) surface waves (e.g Maxeiner and Dalrymple, 2011; Traykovski et al., 2000), decelerating river plumes and resonance effects (e.g Baines, 1984). Held et al. (2013) observed IWs on a lutocline in the Ems estuary, for which they

assumed that they were generated by growing shear instabilities.
Two aspects are focused in this study. Firstly, mechanisms of IW generation in the Ems estuary are analysed in detail to underline the hypothesis proposed in Held et al. (2013). Secondly, conditions leading to IW breaking as well as the role of IWs regarding sediment mixing and transport are investigated. For this, spatial and temporal variability of the detected lutocline was documented with a parametric echo-sounders. Hydro-acoustic datasets were then combined with data of flow velocity measurements and water samples. Based on these data it is possible to compute, for example, the gradient Richardson number, the Reynolds number and the wave steepness. These values allow a deeper insight in the underlying circumstances leading to wave generation or wave breaking. Such a detailed combination of different high-quality hydro-acoustic data to examine the prevailing conditions during IW breaking have not been published yet.

5.2.3 Regional setting and hydrodynamic conditions at the study site

The Ems estuary is located along the Southern North Sea, at the border between north-western Germany and the Netherlands (Fig. 5.11). The lower part is funnel-shaped with an adjoining tidal basin, the Dollart, whereas the part upstream of Pogum is channelized. It is a partially-mixed estuary (van Leussen, 1999). The tidal influenced area extends over about 100 km from the seaward end near the island Borkum to the weir at Herbrum (Spingat and Oumeraci, 2000). The mean tidal range of the lower part of the estuary increases from about 2.25 m near Borkum to 3.1 m at the port of Emden (de Jonge, 1992; van Leussen, 1999). A maximal tidal range of 3.7 m at Papenburg was reported by Jens Jürgens and Norbert Winkel (2003). The estuary is flood dominated (de Kreeke et al., 1997; Held et al., 2013). The mean river discharge underlies strong seasonal variations (de Jonge, 1992) with a mean discharge between 25 and 380 m^3s^{-1} (van Leussen, 1999).
The Ems estuary is well known for high suspension loads with depth-averaged suspended particulate mater (SPM) concentrations of up to 1.6 g l^{-1} (de Jonge, 1983). High concentrated near-bed suspensions are also often observed within the turbidity maximum zone which extends over 60 km (de Kreeke et al., 1997). If the suspended sediment concentration (SSC) of such a layer exceeds 10 g l^{-1} it is called fluid mud (Kineke and Sternberg, 1995; Kirby, 1988; Manning et al., 2010; McAnally et al., 2007; Ross and Mehta, 1989). Papenmeier et al. (2012) introduced a further subdivision of fluid mud

into three sub-classes. They set an upper limit for fluid mud at 500 g l^{-1}. A 1-2 m depth fluid mud layer with SSCs between 10 and 80 kg m^{-3} in the upper Ems estuary is reported by Talke et al. (2009). Such a layer is often bounded by a strong vertical SSC gradient, the so called lutocline.

The Ems estuary is intensively used as waterway, especially to the main ports as well as the shipyard in Papenburg and underlies severe human impact e.g. by repeated deepening, ongoing maintenance as well as constructional works in and along the main navigational channel. This has caused a change of bathymetry over space and time (Chernetsky et al., 2010). The sustained navigable depth currently amounts to 5.7 m at low-water spring (Schuchardt et al., 2007). Additionally, water depth is temporarily increased by river damming at the Ems barrier near Gandersum, for passages of large cruise liners from Papenburg to the open North Sea.

5.2.4 Survey

The measurements were done in the turbidity maximum zone of the Ems estuary from the RV Senckenberg, which was moored near Leerort at 53° 14.077' N and 007° 23.843' E (Fig. 5.11) from 11.06.2012 to 14.06.2012. Neap tide was at the beginning of the survey on the 11.06.2012, the following spring tide was at new moon on 19.06.2012. The ship's heading was set upstream.

Water stratification, especially the lutocline, was recorded with a parametric Sediment Echo-Sounder (SES) of type Innomar SES-2000® standard. The transducer was mounted in a rigid frame midships on the port-side at 1.5 m water depth. The device operated with two frequencies, the primary frequency of 100 kHz and a chosen secondary frequency of 12 kHz. The vertical resolution is 6 cm and the accuracy depends on the frequency and water depth, e.g. 100/10 kHz: 2/4 cm + 0.02% of the water depth. Heave, roll and pitch of the ship were compensated with data of a Seatex® MRU-6 motion sensor. Water depth and interfaces within the water column were extracted from the SES records by using the capturing mode of the SES software ISE 2.9.

Sound velocity profiles were taken for SES data correction regarding sound speed and to examine the nature a sound reflections within the water column. The used sound velocity profiler of type SVP-T15 has a resolution of 0.1 m s^{-1} and an accuracy of 0.25 m s^{-1}. In addition, sound velocities were also calculated from simultaneous taken water samples by the UNESCO formula (UNESCO, 1981), which is based on salinity, temperate and depth values.

Water parameter such as salinity, temperature and SSC were retrieved from water sam-

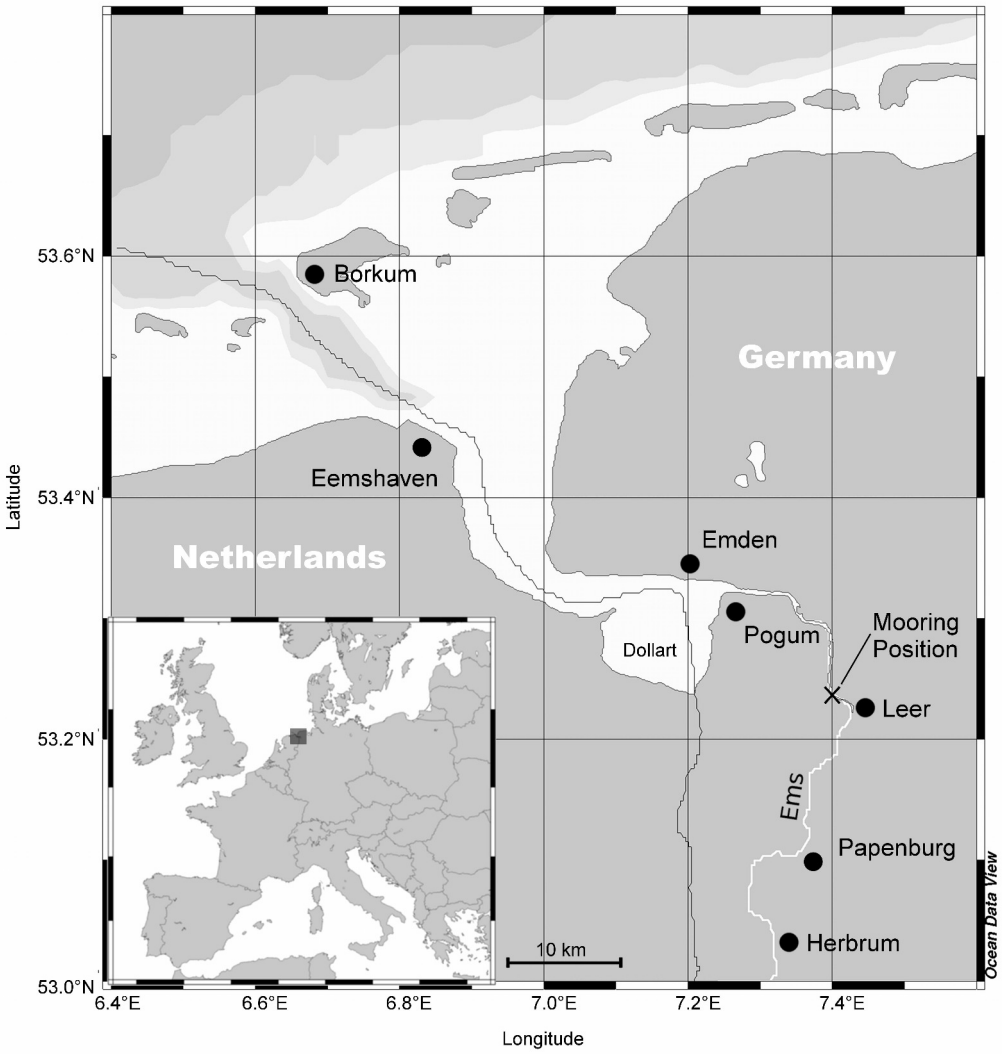

Figure 5.11: Map of the test region. The mooring position of the RV Senckenberg is marked with a black cross. This figure was created with Ocean Data View (Schlitzer, 2013).

ples, which were collected with a horizontal water sampler by HydroBios©. The sampler was aligned in flow direction by a fin and has a sampling volume of approximately 2 l. Temperature was immediately measured after water sampling whereas salinity values were recorded only after settling of the SPM. This procedure prevented for incorrect measurements due to a negative influence of SPM on the conductivity. Temperature and salinity measurements were done with a salinometer of type CON 3310 by WTW® (accuracy of temperature 0.1 °C, accuracy of salinity 0.1). Salinity values are given in terms of the practical salinity scale (PSS-78).
SPM concentrations were recorded as masses per unit water volume. For this, an aliquot of each water samples was vacuum-filtrated through a 1.2 µm glass fibre filter.
Flow velocities were measured with an RDI-Teledyne™ 1200 kHz Workhorse ADCP (Acoustic Doppler Current Profiler), which was installed at 1.81 m water depth at the port-side of the research vessel. The select cell size was set to 0.25 m. It has a blanking-zone of 0.5 m. The standard deviation of the velocity measurements amounts to 0.129 m s^{-1}.

5.2.5 Data analysis

To reveal the IW generation mechanism and the prevailing conditions during wave breaking, the hydrodynamic conditions were derived form the recorded data and their temporal evolutions were investigated.
The Richardson number is an indicator for the stability of sheared flows and defined as the ratio of the potential to the kinetic energy of a fluid:

$$Ri = \frac{g}{\rho} \frac{\mathrm{d}\rho/\mathrm{d}z}{(\mathrm{d}u/\mathrm{d}z)^2} \tag{5.9}$$

where g is the acceleration due to gravity and $\mathrm{d}\rho/\mathrm{d}z$ and $\mathrm{d}u/\mathrm{d}z$ are the vertical gradients of density and velocity, respectively. If the Richardson number falls below 0.25 the flow will become unstable and susceptible for disturbances (Lott et al., 1992). A $\mathrm{Ri} < 0.25$ is also necessary criterion for the formation of Kelvin-Helmholtz instabilities in stratified shear flows (Miles, 1961).
The shear stress upon the lutocline was determined by fitting the horizontal flow velocities of the upper water layer into a logarithmic velocity profile:

$$u(z) = \frac{U^*}{\kappa} \ln(z) \tag{5.10}$$

where κ is the dimensionless Karman constant ($\kappa = 0.4$) and U^* is the shear stress velocity which is related to the shear stress τ via the following definition:

$$U^* = \sqrt{\frac{\tau}{\rho}} \tag{5.11}$$

The required density values were obtained from water samples.
To investigate the conditions leading to IW breaking, the wave steepness and the state of flow were considered in detail 10 minutes before and while the first breaking event. Wave steepness is defined as the ratio of the wave height H to the wave length λ:

$$\xi = \frac{H}{\lambda} \tag{5.12}$$

It is a classical geometric criterion for the stability of waves. If a wave exceeds a certain steepness it will become unstable and collapse. Tanaka (1983) found a limit steepness of 0.137 for surface gravity waves. The application of Eq. 5.12 requires the height and the length of the waves. Wave heights could be directly retrieved from the SES records whereas wave lengths had to be calculated with Eq. 5.8. The required wave period was obtained by a fast Fourier transformation (FFT) of the lutocline oscillations. The wave period is the reciprocal of the main frequency of the gained spectrum.
The state of flow of the upper layer was determined by the Reynolds number, representing the ratio of inertial force to frictional force:

$$\mathrm{Re} = \frac{U_1 \cdot d_1}{\mu_1/\rho_1} \tag{5.13}$$

where U_1 is the mean horizontal flow speed, d_1 is the depth and μ_1 and ρ_1 are the dynamic viscosity and density of the upper layer, respectively. The flow is laminar for low values of the Reynolds number, whereas it becomes turbulent for high Reynolds numbers (Kuhlmann, 2007). However, the Reynolds number is a similarity parameter, meaning that only values of hydro-dynamic similar systems are comparable. Limit values for the transition to turbulent flow must be specified for particular systems.
The required dynamic viscosities were determined with a relation found by Papenmeier et al. (2014). They found a relationship, connecting the dynamic viscosity with the SSC.
The stability of the stratification was estimated by the Brunt-Väisälä frequency (Eq. 5.7) of the lutocline. The Brunt-Väisälä frequency represents a quantitative measure for the stability of the stratification since it is directly proportional to the square root of the

density gradient. The higher the value of a real N the more stable is the corresponding system. A stratification is unstable for an imaginary value of N which could be achieved by an inverse density stratification.

5.2.6 Results

Water stratification

The SES detected internal reflectors at depths between 4m and 6.5 m within the water column. However, such a reflector was not always detectable. It was mainly visible around high-water slack and during ebb tide whereas it was not visible at low water slack and mostly during flood tide. Additionally, the SPM concentrations below the detected reflectors were clearly increased, indicating the presence of fluid mud. The lower layer had a thickness of 3-5.5 m and a SPM concentration between 14.33 ± 1.37 g l^{-1} and 74.25 ± 1.37 g l^{-1} (mean 38.30 g l^{-1}). The concentrations above the reflector varied between 0.28 ± 0.01 g l^{-1} and 5.02 ± 0.01 g l^{-1} (mean 1.63 g l^{-1}). The SPM concentrations in the course of two ebb-cycles are shown in Fig. 5.12.
When comparing the water samples, taken during the slack water phases, other features become obvious (Fig. 5.13). At high-water slack, the layer above the reflector had a higher salinity than the fluid mud layer, whereas it was the opposite way around during low-water slack. The salinity of the fluid mud layer was almost constant, but salinity varied between 0.9 ± 0.1 (low-water slack at 12.06.2012 1250 UTC) and 4.1 ± 0.1 (high-water slack at 12.06.2012 1800 UTC) in the upper layer.

Sound velocity profiles

Sound velocity profiles are exemplarily shown for selected slack-water phases in Fig. 5.14. They revealed, with one exception, an abrupt decrease of sound velocity, which had a width of less than 1 m. Calculated sound velocities are shown in the same figure. The calculated sound velocities coincided with the measured one in the upper water column. However, none of the calculated sound velocities showed an abrupt decrease with depth.

Flow velocities

The depth-averaged flow velocities of the upper layer revealed a clear flood-current dominance (Fig. 5.15). Peak current velocities of up to 1.35 m s^{-1} were reached during

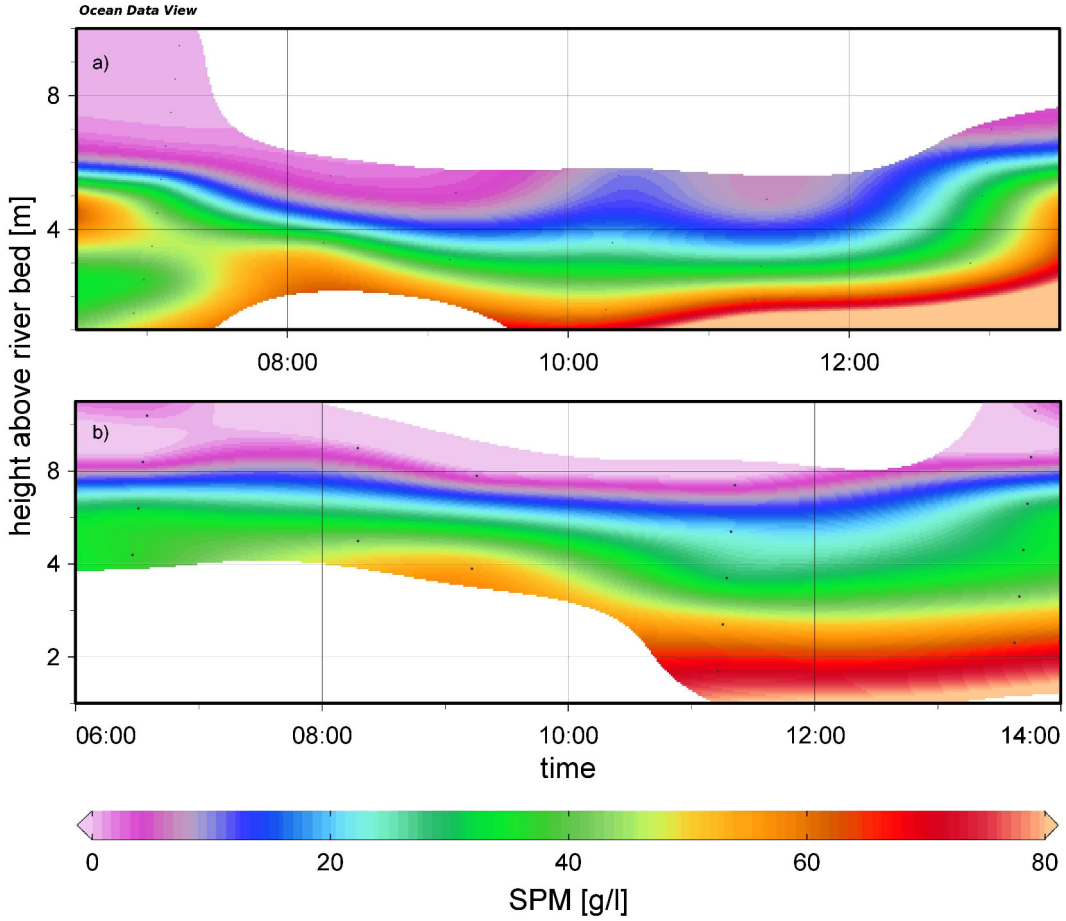

Figure 5.12: Temporal development of the SPM-concentrations for the ebb-cycle from 0525 to 1228 UTC on 12.06.2012 a) and from 0635 to 1318 UTC on 13.06.2012 b). The small black points correspond to the collected water samples. This figure was created with Ocean Data View (Schlitzer, 2013).

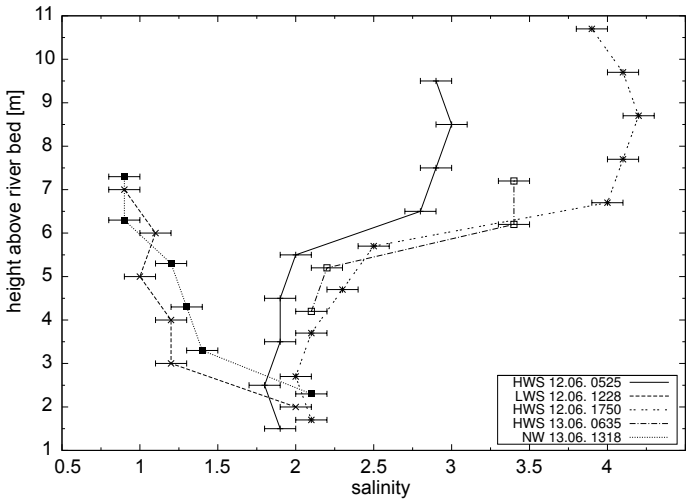

Figure 5.13: Salinities of water samples which were taken during the slack water phase.

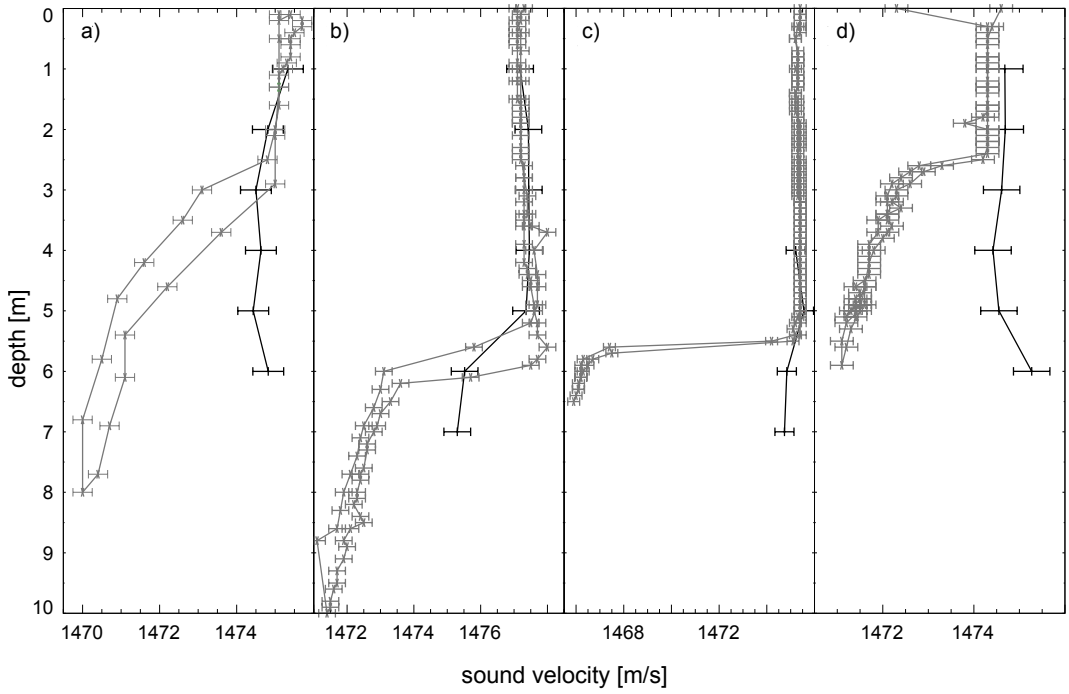

Figure 5.14: Comparision of computed sound velocities (black curve) and measurements taken with SVP-T15 (gray curve), a) LWS 1325 UTC 12.06.20121, b) HWS 1806 UTC 12.06.2012, c) HWS 0643 UTC 13.06.2012 and d) LWS 1357 UTC 13.06.2012.

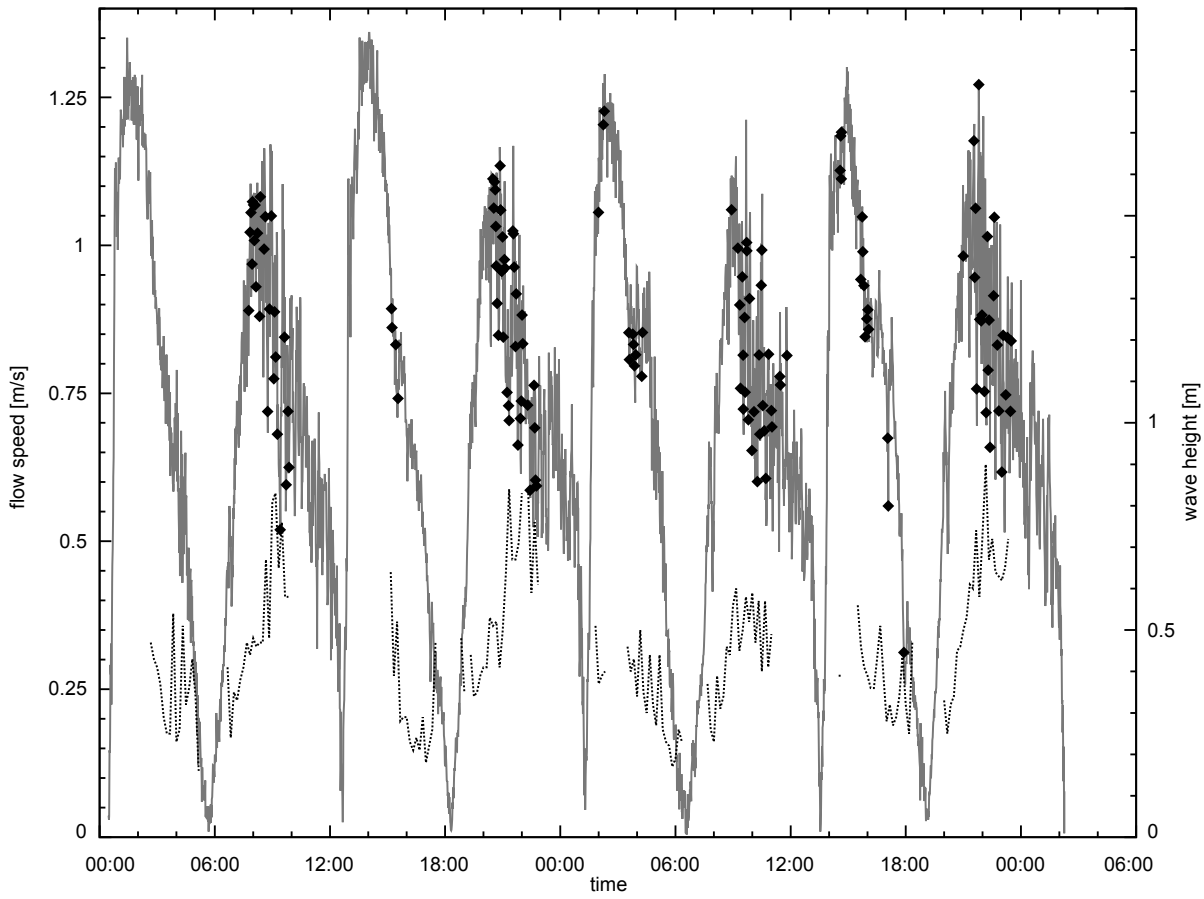

Figure 5.15: Horizontal flow speeds of the water layer above the fluid mud (gray curve) together with significant wave heights of the IWs (black dotted curve). Gaps of the significant wave height curve occur when no lutocline was detected by the SES. IW breaking events are marked with black diamonds.

flood tide. In spite of this flood-current dominance, the ebb tide took longer than the flood tide. The duration of the ebb tide was on average 7 hours, whereas flood tide was significantly shorter with only 5 hours and 21 minutes. Strong current oscillations occurred in the records during ebb tide.

Shear stress and Richardson numbers during IW generation

The onset of IW generation was identified in the SES time-series as the time when the reflectivity of the lutocline (i.e. the amplitude in the SES records) starts to decrease and the first small undulations occur. Values for the shear stress (Eq. 5.11) and the Richardson number (Eq. 5.9) were calculated for the time 10 min before, at and 10 min after the onset of IW generation. It could be concluded from these temporal evolutions

(Fig. 5.16), that the shear stress significantly increased during IW generation. The shear stress continuously increased after the first undulations had occurred . At the same time, the Richardson number decreased clearly. Values of up to 3.5 were calculated for the time 10 min before the onset of IW generation. During the beginning of IW generation, the Richardson number was below 0.25 in all investigated cases. It also remained below this limit 10 min after the first undulations occurred.

Wave steepness and state of flow at IW breaking

The end of an IW is marked by its breaking. During IW breaking events, the reflector in the SES time series temporarily disappeared. Additionally, the upper water layer became more turbid. The time interval between the onset of IW generation and the first observed IW breaking event varied between 66 min and 97 min with an average of 81 min. During this time period, IWs grew from zero to maximum heights of up to 1.5 - 2 m, and significant wave heights of 0.9 m were reached (Fig. 5.15).
Wave steepness and Reynolds number are presented for the time 10 min (t = -10 min) before and at the first wave breaking event (t = 0 min) in Fig. 5.17. In all cases, the wave steepness had been increased during the last 10 min before the waves broke. However, it was difficult to define a limit for the wave steepness from these data. At least, it could be seen that all breaking waves were steeper than 0.055. But it has to be mentioned that non-breaking IWs of steepness 0.060 were observed at t = -10 min.
The situation was different for the Reynolds numbers. An increase of their values could not be noticed during the last 10 min before the IWs broke. On the contrary, the Reynolds numbers of all examined cases slightly decreased during that period (Fig. 5.17).

Diapycnal mixing

The mixing of SPM across the lutocline was analysed for the ebb phase from 0525 to 1228 UTC on 12.06.2012 (Fig. 5.12.a) and for the ebb phase from 0635 to 1318 UTC on 13.06.2012 (Fig. 5.12.b). The depth-averaged SPM-concentration increased from 22.8 g l^{-1} to 36.2 g l^{-1} during the first mentioned ebb-cycle and from 17.8 g l^{-1} to 28.0 g l^{-1} during the latter one. In both cases, the height of the lutocline decreased in the course of the ebb tide, whereas it rose again during the subsequent low water slack. Additionally, a widening of the lutocline was observed during the second half of the ebb tide, in both cases.
At about 1030 UTC on 12.06.2012, there was a strong short-term increase of SPM

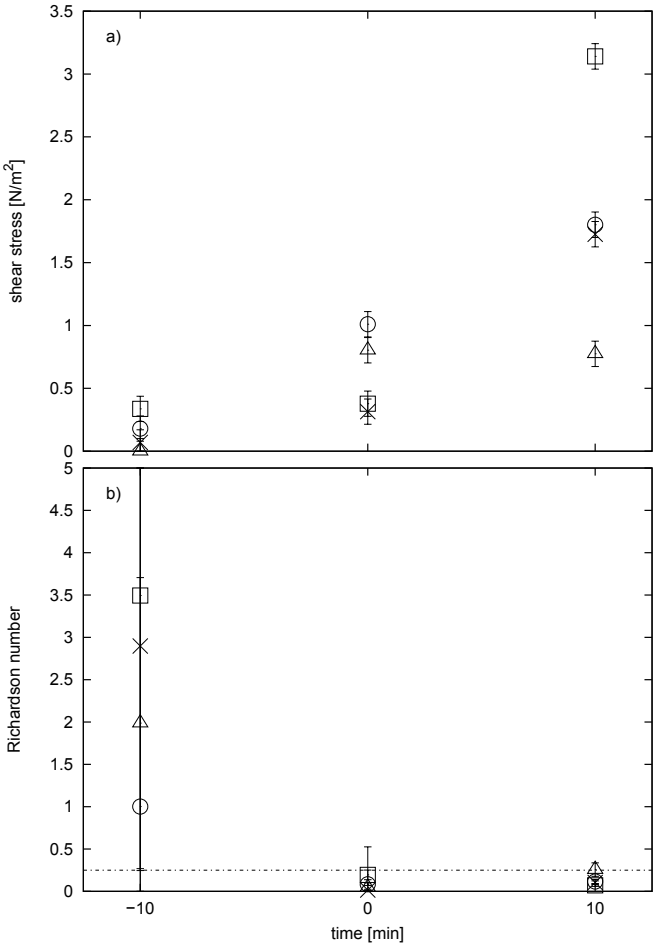

Figure 5.16: Shear stress on the lutocline (a) and gradient Richardson number (b) at the onset of IW generation (t=0) for four ebb-cycle, 0645 UTC 12.06.2012 (cross), 1910 UTC 12.06.2012 (square), 0744 UTC 13.06.2012 (circle) and 1953 UTC 13.06.2012 (triangle). The limit of the Richardson number for the generation of Kelvin-Helmholtz instabilities (Ri = 0.25) is indicated by the dash-dot line in b).

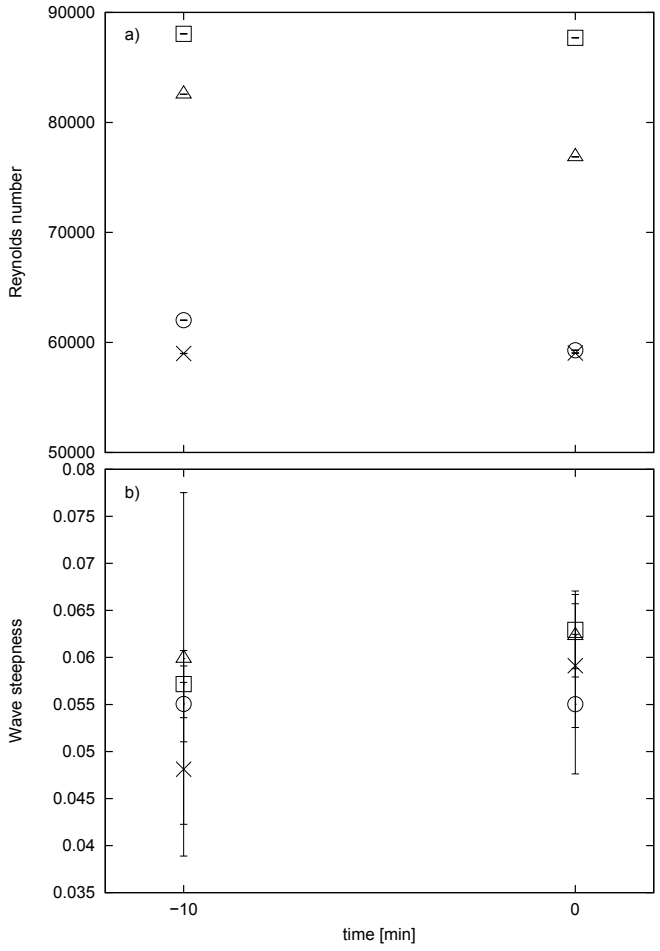

Figure 5.17: Temporal course of the Reynolds number a) and wave steepness b) when the first IWs are about to break (t=0), 0803 UTC 12.06.2012 (cross), 2029 UTC 12.06.2012 (square), 0907 UTC 13.07.2012 (circle) and 2130 UTC 13.06.2012 (triangle). Please note that the errorbars in the upper panel are smaller than the symbol sizes and may get oversight.

Table 5.1: Time course of the Brunt-Väisälä frequency of the lutocline for two ebb-cycle. The values of the last column were computed close to low-water slack.

ebb-cycle: 0525 - 1228 UTC 12.06.2012	time after HWS [min]:	100	172	227	357	451 (LWS)
	N^2:	0.2250	0.1552	0.0905	0.0822	0.1317
ebb-cycle: 0635 - 1318 UTC 13.06.2012	time after HWS [min]:	0	100	160	280	430 (LWS)
	N^2:	0.1739	0.1196	0.1532	0.1173	0.1638

concentration above the lutocline (Fig. 5.12.a). The corresponding water sample was most probably collected after an IW breaking event, which mixed sediment into the upper water layer.
The calculated Brunt-Väisälä frequencies of the lutocline are presented in table 5.1) for the above mentioned ebb tides. The smallest values of the Brunt-Väisälä frequency were reached during the second half of the ebb tides. N^2 was reduced by 30 - 60 percent at these times.

5.2.7 Interpretation and discussion

Stratification

It could be concluded from the obtained water samples and the recorded SES time-series that the water column at the measuring station was at least subdivided into to layers. A upper water layer with low to moderate SPM concentrations and a 3 - 5.5 m thick fluid mud layer near the bottom. The observerd fluid mud layer was hence thicker than that one reported by Talke et al. (2009). However the SPM concentrations were similar. Averaging of SPM concentrations over the complete water column revealed noticeably larger values than that ones reported by de Jonge (1983).
The SPM concentrations of the whole water column were significantly higher at low-water slack than at high-water slack, which agrees with other findings in literature. de Kreeke et al. (1997) took stationary time series between Eemshaven and Emden and observed that suspended sediment concentrations were higher during ebb tide than during flood tide, although the current velocities behaved in the opposite way.
The height of the lutocline was more or less the same during both slack waters, meaning that the tidal range mainly took place in the upper water layer. This finding was

supported by the salinity time courses of the fluid mud layer and the upper water layer. Diluted marine water flowed upstream in the upper layer during flood tide, whereas fresh water was stratified over the fluid mud layer during ebb tide. The salinity of the fluid mud layer remained almost constant, indicating a minor salt exchange between both layers. Such a conservative behaviour of fluid mud was also reported by Kineke and Sternberg (1995). Additionally, the lutocline declined during ebb tide. These findings indicated that fluid mud thickness mainly depended on the current velocity rather than on the tidal phase.

Sound velocities

The abrupt decrease of sound velocity with depth coincided with the depth of the reflector in the SES records and with the increase of the SPM concentrations. Thus, the reflector detected by SES was clearly a lutocline. This finding agreed well with other findings in the literature. Both Wurpts (2005) and Held et al. (2013) reported on hydro-acoustic detected fluid mud layers in the Ems estuary. In fact, that sediment induced interfaces within the water column can cause acoustical backscatter has been known since the introduction of echo-sounders on board ships in the 1930's (Kirby, 2013). However, the cause of hydro-acoustic backscatter from lutoclines was not described in any of these studies. The calculated sound velocities agreed quite well in the upper less turbid water layer with the values of the measured sound velocity profiles. However, this was not the case in the fluid mud layer, where the calculated values didn't match with the measured ones. The discrepancies amounted to several m s^{-1}, and were hence greater than the accuracy of measurements. Thus, SPM had a clear influence on the sound velocity and the UNESCO algorithm (UNESCO, 1981) for the sound velocity was not applicable in high turbid water layers.

Current velocities

ADCP measurements were only possible in the upper less turbid water layer, because only bad and sometimes even none echos were received from the fluid mud layer. This was caused by the high SPM concentrations within the fluid mud, which strongly attenuate the sound signal (Gratiot et al., 2000; Sottolichio et al., 2011).
The observed flood-current dominance of the Ems estuary was also notice by de Kreeke et al. (1997). The strong current oscillations during ebb tide were the same as that one already described by Held et al. (2013). They showed by frequency-analysis of time-series, recorded by different hydro-acoustic devices, that these oscillations were caused

by high IWs. Such footprints of IWs in velocity records were also observed by Adams Jr. et al. (1990).

IW generation

The temporal evolutions of the shear stresses and of the Richardson numbers around IW generation showed clearly, that the first observed disturbances on the lutocline were Kelvin-Helmholtz instabilities. Thus, the generation mechanism of IWs in the Ems estuary was different to those mostly described in literature, where IWs were mainly generated by a current-topographic interaction. Further indications, contradicting a topographic induced generations are: a lee wave generation mechanism could be excluded since firstly, the observed IWs were no solitons. Additionally, wave growing was observed at the measuring station. The latter indicates, that the waves were generated and further excited over a wider area, so that all the time new and higher grown IWs passed the observation point. Additionally, a resonant wave generation was already excluded by Held et al. (2013). They already assumed that the IWs in Ems estuary were created by growing Kelvin-Helmholtz instabilities, but couldn't prove this because of the lack of high-resolution SPM-concentration measurements. A physical and mathematical prove for the generation of IWs by Kelvin-Helmholtz instability in the Ems estuary is therefore firstly presented in the current study.
After they had appeared on the lutocline, the first wave-like undulations were further stimulated by still faster flowing upper water layer. The undulations modulated the flow field, causing lower pressures in front of an undulation and higher presser behind by the Bernoulli effect. These pressure patterns finally caused the development of IWs out of the Kelvin-Helmholtz instabilities (Otten, 2008; Ott, 1996; Miles, 1957).

Breaking of IW

Although an increase of wave steepness could be observed during the last 10 min before the first wave breaker occurred, a threshold for the wave steepness could not be defined. A maximum wave steepness of 0.060 for a non-breaking IW was calculated. This values was less than of the limit for surface waves (Tanaka, 1983).
The temporal evolution of the Reynolds numbers showed a slight decrease just prior wave breaking. Thus, IW breaking was not caused by a destabilisation of the background current.
In general, wave breaking is a difficult topic and not very well understood yet, even there was a lot of effort in the last century. The most well-known criteria are the wave steepness

and the ratio between the crest velocity and the phase speed. The latter is a logical criterion: If the wave crest propagates faster than the rest of the wave, it will overturn and the wave will break. However, a lot of experimental studies and observations have shown waves, that had broken long before they have reached this threshold (Banner and Peregrine, 1993; Oh et al., 2005). Small instabilities are always present on waves, and sometimes they grow until they cause the collapse of the wave. For example, if wind is blowing over the sea surface, small capillary waves will be present. These capillary waves are modulated and steepened up by long gravity waves. If they collapse they can trigger the break down of the complete gravity wave (Banner and Peregrine, 1993). Such instabilities make it difficult to define a general accepted breaking criterion. Common breaking criteria only exist at beaches. These criteria are usually based on relations between the wave height or length and the water depth (Peregrine, 1983).
Oh et al. (2005) found out that a dynamic criterion, based on the ratio between surface acceleration and gravity, is more suitable to describe the stability of deep-water waves. But surface accelerations are difficult to measure and even impossible for the IWs studied in this work.
Another cause for IW breaking are accelerated shear flows, which are able to deform IWs until they overturn and collapse (Bouruet-Aubertot and Thorpe, 1999). However, it was unlikely that accelerated shear flows trigger IW breaking in the Ems estuary, since most breaking events occurred after the ebb current had peaked.

5.2.8 Mixing of SPM by breaking IWs

The lutocline became wider and was descending during the second half of the ebb tide. These two processes coincided with the occurrence of IW breakers. Additionally, the upper water layer became more turbid during that time. It was therefore concluded that IW breaking eroded the fluid mud layer and mixed sediment into the upper less turbid water layer. The vertical exchange of sediment decreased also the stratification. The corresponding Brunt-Väisälä frequency of the lutocline reached its lowest values during the second half of the ebb-tide.
That breaking IWs could cause vertical exchange is known, it is even the main source for turbulence and diapycnal mixing in the oceans (Leichter et al., 2005). Turbulent events are in turn import for sediment transport processes (Pomar et al., 2012; Birch and Sundermeyer, 2011).
In the Ems estuary, vertical uplift of sediment from the fluid mud layer by breaking IWs was already observed by Held et al. (2013). However, they only presented a qualitative

description. This study on contrast presents the temporal evolution of the lutoclines and of the SPM distributions during ebb tide. These results were combined with quantifications of the stratification by means of the Brunt-Väisälä frequency. This study therefore provides quantitative informations about the influence of breaking IWs on the vertical exchange of sediment in the Ems estuary for the first time.

5.2.9 Conclusion

In this study, the generation mechanism and the break down of IW on a lutocline in the German Ems estuary during ebb tide were investigated. For this, the temporal evolutions of hydrodynamic and wave parameters during IW generation and wave breaking were analysed. In addition, the contribution of IW breaking to the vertical exchange of sediment was examined. This was done by analysing the evolution of the SPM distribution in the water column and of the Brunt-Väisälä frequency which quantize the stability of the stratification.
From these investigations, the following findings were concluded:

1. Water stratification in the Ems estuary was caused by a strong increase of SPM with depth. Salinity and temperature variations had only a minor effect. SPM concentrations of up to 74.25 g l^{-1} indicated the presence of a 3 - 5.5 m thick fluid mud layer.

2. Onset of IW generation was on average 75 minutes after high-water slack. Further 81 minutes later the first breakers occurred. Wave heights of 1.5 – 2 m and significant wave heights of 0.9 m were reached.

3. Richardson numbers were below 0.25 during the onset of IW generation. These results proved that IWs develop from Kelvin-Helmholtz instabilities, caused by a strong shear stress between the fluid mud layer and the overlaying water column. Such a generation mechanism is in contrast to other findings in literature, where IWs in coastal waters are mainly caused by an interaction between currents and topographic obstacles.

4. IW breaking could neither be predicted by the wave steepnesses nor by the Reynolds numbers, since in half of the investigated cases, both values were higher 10 minutes before than at the first wave breaking.

5. Shear stress and IW breaking caused an erosion of the fluid mud layer during ebb tide, which was manifested by a decline of the lutocline. Additionally, the lutocline became wider and the corresponding Brunt-Väisälä frequency of the lutocline depth decreased to a third of its value during previous slack water. IW collapse temporarily increased the SPM concentration above lutocline by mixing fluid mud into the upper water layer.

5.2.10 Acknowledgements

The authors would like to thank the captain and crew of "RV Senckenberg" for their excellent job and inexhaustible patience during the acquisition of the datasets for this study. Alexander Bartholomä from the Senckenberg Institute and Jens Boczek are thanked for their support on board the ship. Our student assistants are thanked for analysing the water samples. The Senckenberg Institute kindly provided the ship time. This study was funded by the Deutsche Forschungsgemeinschaft as part of the Cluster of Excellence 'The Future Ocean'.

5.3 Summary and conclusion of chapter 5

The previous two sections dealt with IWs on a lutocline in the Ems estuary. The three main objects were: To identify and understand the processes of IW generation, to identify the hydro-dynamic conditions leading to IW breaking and to estimate the role of IW breaking for the sediment transport dynamics in the Ems estuary. For this, hydro-acoustic records, flow speed measurements and water samples of three different Ems surveys in the years 2007, 2008 and 2012 were evaluated and analysed. SES records of the lutocline were used to determine the beginning of IW generation, to measure wave heights and to identify IW breaking events. Flow speeds, measured with an ADCP, were used to determine the movement patterns of the fluid mud layer and of the overlaying water body, as well as to derive flow speed gradients within the water column. Frequency analysis of the SES and ADCP time-series were done to check whether features in both time-series are caused by the phenomenon. Water samples were collected to figure out SPM concentrations and to measure salinities. Further hydrodynamic and wave parameters, like Richardson and Reynolds numbers, buoyancy frequencies, wave lengths and steepnesses, were mathematically deduced from the mentioned measurements. These investigations allowed to clearly identify the generation mechanism of the IWs in the Ems estuary and to get further insights in the processes leading to IW breaking. The influence of IW breaking on the stratification stability was determined in terms of the Brunt-Väisälä frequency. A contribution of IW breaking to vertical exchange and sediment transport dynamics was also observed.
The main findings in more detail were:

- A clear and prominent lutocline developed in the TMZ of the Ems estuary mainly during high-water slack. The high SPM concentrations below the lutocline indicated the presence of a 2 - 5.5 m thick fluid mud layer.

- Both layers, fluid mud and upper water layer, were differently strong forced by the tides, resulting in a faster flowing water layer during Ebb tide. In contrast, both layers had similar depth-averaged flow speeds during flood tide.

- The different depth-averaged flow speeds caused shear stress between both layers during the onset of ebb tide. This shear stress triggered in turn the development of Kelvin-Helmholtz instabilities, as indicated by Froude numbers below 0.25. Wave like features grew from these instabilities through further excitation by rising ebb current. Hence, IWs in the Ems estuary are neither internal tides nor produced

by current-topographic interaction, as it is mostly the case for IWs described in literature.

- Maximum significant wave heights of up to 1.3 m were reached after the ebb current had been peaked.
- High IWs modulated the current in the Ems estuary. The depth-averaged flow speed oscillated with the wave frequencies during the time the highest IWs appeared. This was checked by a frequency analysis of the ADCP and SES data sets.
- The first breakers occurred less than two hours after the onset of IW generation. Wave breaking was neither triggered by the state of flow nor by the wave steepness. The temporal evolution of the Reynolds numbers and the waves steepnesses didn't indicated a clear limit.
- IW breaking mixed fluid mud across the lutocline, which resulted in a temporary increase of SPM concentration in the upper water body. This became also visible as dark clouds at the water surface.
- IW breaking eroded the lutocline, indicated by a widening of the lutocline and reduced hydro-acoustic backscatter. Additionally, the Brunt-Väisälä frequency of the lutocline decreased by up to 60 percent, denoting a reduced stratification stability.
- During the second half of the ebb tide, the flow speed of the upper water water layer was higher than that of the fluid mud layer and significantly more IW breaking events occurred compared to the other tidal phases. These two facts meant that IW breaking supported the downstream transport of sediment.

6 Summary and overall-conclusion

This thesis dealt with IWs on a lutocline and their contribution to sediment dynamics in the Ems estuary. Firstly it was verified whether the used marine measurement devices which were developed and calibrated for clear water usage operate properly in high turbid water layers. These validations were necessary, because of the high suspension loads of the Ems, which can reach depth-averaged suspended sediment concentrations of up to 1.6 g l^{-1} (Wurpts, 2005). Concentrations of even several ten's of kg m^{-3} were measured in the fluid mud layers by Talke et al. (2009).

An influence of SPM was especially assumed for conductivity-based salinity measurements. This assumption was based on hints in the literature, where some authors observed fluid mud layers with clearly lower salinities than the overlaying water body. However, salinity is an import water parameter since it, among others, strongly influences the water density and velocity of sound in fluids. In this thesis water densities were in turn required to calculate wave parameters, such as the IW lengths. A possible influence was hence checked in the frame of a laboratory study. For this, natural mud samples from two different locations were collected and desalinated. Afterward, these mud samples were used to adjust solutions with specific salinities and SPM concentrations. Salinity was measured in several test runs with solutions differing in SPM concentrations and salinities. The influence of SPM was determined as the difference between adjusted and measured salinity.

The influence of SPM on the sound propagation in water was additionally checked. SPM can affect sound propagation in different ways. It changes the water density, which is well known and the density of the corresponding suspension can be calculated with a mathematical expression given in Gabioux et al. (2005). Additionally, it can change the sound velocity by scattering a part of the sound wave or by influencing the compressibility of water. The exact influence of natural SPM on the sound propagation is not fully understood yet and a correction of the sound velocity for the SPM concentration has not been published so far. Both parameters are required to predict the reflectivity of water layers and hence for a better interpretation of hydro-acoustic records of the water

column. Thus, the influence of SPM on the sound velocity was investigated in the frame of laboratory and field experiments as well as by numerical modelling. Additionally, the reflectivities of real lutoclines were simulated with a weak-scattering model.
SPM may also affect hydro-acoustic current measurements, because of multiple scattering of the sound signal by the dissolved particles. Multiple scattering in turn affects the Doppler shift of the signal leading to wrong current velocities. However, Gratiot et al. (2000) already validated the reliability of acoustic Doppler velocimeters in turbid suspensions. They conducted several tank experiments and found out that a multiple scattered signal is strongly attenuated so that no echo returns to the transducer. Suspended particles thus do not influence hydro-acoustic velocity measurements. ADCP measurements in the TMZ of the Ems estuary were therefore considered to be trustworthy in this study.
The IW investigations are based on data collected during three surveys in the years 2007, 2008 and 2012. These data were used to examine how the IWs develop on a lutocline, which conditions lead to their breaking and last but not least their contribution to vertical mixing and sediment transport processes in the Ems estuary. IW generation was investigated by analysing the hydrodynamic conditions prevailing while the first disturbances were appearing on the lutocline. The breaking of IWs was examined by analysing the temporal evolutions of the state of flow and of wave parameters, e.g. wave steepness. Last but not least, the contribution of breaking IWs to vertical mixing and sediment transports processes was examined in terms of variations of the SPM distributions, caused by breaking waves. The affect of IW breaking on the stratification was analysed by the temporal evolutions of the buoyancy frequencies, which are a quantize for the stability of a stratification. Before the above mentioned investigations were carried out, it had been checked, too, whether the measurements of different hydro-acoustic devices revealed the same features.
The following main findings could be concluded from these investigations:

- Conductivity based salinity measurements were distorted in high turbid waters with SPM concentrations above 10 g l^{-1}, reaching deviations of up to 30 % for a SPM concentration of 300 g l^{-1}. The deviations may be neglectible for lower concentrations, depending on the requested accuracy.

- These deviations were caused by a “blinding effect” of the measuring cell by suspended particles. The cell geometry had no influence.

- Better and more accurate results will be obtained if salinity is measured in collected

water samples after SPM had settled.

- SPM also affected the sound velocity. The velocity of sound in suspensions decreased with increasing SPM concentrations. The dependence of the sound velocity on the SPM concentration was small compared with its dependence on the temperature or salinity.

- A calculation of the sound velocity in turbid water layers was not possible with previously published algorithms. Additionally, the conducted experiments indicated that the speed of sound depends also on the size of the suspended particles.

- Further investigations on the acoustical properties of SPM, i.e. primary particles as well as agglomerates, are recommended therefore.

- A published weak-scattering model could be adapted to simulate the reflectivity of lutoclines in dependence of the SPM gradient, the sound velocity profile and the acoustic wave length.

- Simulations for natural lutoclines showed a decrease of the reflection coefficient with increasing signal frequency. In addition, the depths of the maximum reflections varied by several 10 cm, depending on the signal frequency. The latter has to be taken into account when comparing records of a lutocline, recorded with different frequencies.

- A 2 - 5.5 m thick fluid mud layer with a prominent lutocline developed in the TMZ of the Ems estuary during high-water slack.

- Fluid mud layer and overlaying water body underlie different accelerations in the course of an ebb tide, resulting in different flow speeds of both layers. This caused rising shear stress between both layers during increasing ebb current. In contrast, the both layers had almost the same current velocities during flood tide.

- The shear stress destabilized the lutocline and triggered the development of instabilities. The appearance of Kelvin-Helmholtz instabilities could be verified by Richardson numbers below 0.25 when the first undulations appeared on the lutocline. The first undulations were observed on average 75 minutes after high water slack.

- IWs developed out of these Kelvin-Helmholtz instabilities by further excitation caused by a rising ebb current. The generation mechanism of the observed IWs

was hence different from that mostly described in literature, where IWs mostly are either internal tides or generated by current-topographic interactions.

- The highest IWs, with maximum wave heights of 1.5 to 2 m, occurred after the ebb current had been peaked and the shear stress decreased.
- During flood tides, the wave fields were more regular than during ebb tides, indicating the presence of a kind of "swell" on the lutocline. Combined with the neglectible shear stress during flood tide, this suggested that IW generation took place only during the ebb cycles.
- First IW breakers appeared on averaged 80 minutes after the onset of IW generation. A breaking criterion in terms of the wave steepness of the Reynolds number could not be defined. Nevertheless, some lower limits were observed: A wave height of at least 0.4 m, a steepness of at least 0.055 combined with a shear stress between both layers led to IW breaking.
- Shear stress and IW breaking caused an erosion of the fluid mud layer during ebb tide, manifested in a decline and widening of the lutocline during the second half of the ebb tide.
- IW breaking was linked with vertical exchange of sediment. The water body above the lutocline became more turbid after an IW breaking events, which were sometimes even visible at the water surface as dark clouds. The vertical mixing of sediment reduced the stratification stability, indicated by a decrease of the Brunt-Väisälä frequency by up to one third.
- Significantly more IW breaking events were observed during ebb tide than during flood tide.
- The vertical exchange of fluid mud together with the faster flowing upper water body during ebb tide mean that IW breaking supported the downstream transport of sediment.
- The wave pattern were more regular during flood tide than during ebb tide. The wave field consisted of four to five main wave components during flood tide, whereas it was completely irregular during ebb tide.
- High IWs caused disturbances of the depth-averaged current velocity, which oscillated with the main wave frequency during the second half of the ebb tide.

- Although, it was not possible to define a breaking criterion for IWs in the frame of this thesis, new insights in the processes prevailing during IW breaking were gained. It must also be mentioned that wave breaking is a very complex issue and the circumstances leading to wave breaking, even for surface waves, are not fully understood up to now.

Acknowledgements

I would like to thank Prof. Dr. Kerstin Schrottke for taking on the supervision and Prof. Dr. Karl Stattegger for taking on the co-supervision of this PhD-thesis. It was carried out in the research group "Sea-Level Rise and Coastal Erosion" which is a part of the DFG (Deutsche Forschungsgemeinschaft) Cluster of Excellence 'The Future Ocean'. I thank Dr. Alexander Bartholomä for his help on board the RV 'Senckenberg' during the Ems surveys and for proofreading the first paper.

Special thanks go to Angela Trumpf for insightful discussions and her technical assistances in the laboratory.

Furthermore, I would like to thank my colleagues for supporting, useful discussions (in the office and after work) and the enjoyable working atmosphere.

Special thanks also go to my colleague Daniel Unverricht for the enlightening discussions during the coffee breaks and for taking me to the shores to calming down, relaxing and kitesurfing. He and his girlfriend Sarah are also thanked for having enjoyable evenings together and for always feeding my birds when I had been absent.

I would also like to thank to the master and crew of the RV 'Senckenberg', they made an excellent job and showed inexhaustible patience during the Ems surveys.

Also many thanks go to Arnulf Möller from the Senckenberg Institute for processing the MBES data.

Our student assistants, especially Stephanie Peters, are thanked for filtering the water samples and the excellent job she has always been doing in the laboratory.

Further, I would like to give special thanks Vera Tödt, Tebke Böschen and Julian Jess for proofreading the manuscript and English correction advices.

Last but not least, I would like to thank my family who were supporting me throughout my life and endured the moments of bad mood. I want especially to thank my mother who has always been believing in me and always encouraged me to go my way.

Finally, my friends and family, I want to apologize myself for being rarely available during the last months.

References

Adams Jr., C.E., Wells, J.T., Park, Y.A., 1990. Internal hydraulics of a sediment-stratified channel flow. Marine Geology 95, 131–145.

Apel, J.R., 1987. Principles of Ocean Physics. Academic Press.

Archie, G. E., 1942. The electrical resistivity log as an aid in determining some reservoir characteristics. Petroleum Technology , 54–62.

Baines, P.G., 1984. A unified description of two-layer flow over topography. Journal of Fluid Mechanics 146, 127–167.

Baines, P.G., 1995. Topographic effects in stratified flows. Cambridge University Press.

Baldock, T., Manoonvoravong, P., Pham, K.S., 2010. Sediment transport and beach morphodynamics induced by free long waves, bound long waves and wave groups. Coastal Engineering 57, 898–916.

Banner, M.L., Peregrine, D.H., 1993. Wave breaking in deep water. Annual Review of Fluid Mechanics 25, 373–397.

Becker, M., 2011. Suspended Sediment Transport and Fluid Mud Dynamics in Tidal Estuaries. PhD thesis. University of Bremen. Bremen.

Birch, D.A., Sundermeyer, M.A., 2011. Breaking internal wave groups: Mixing and momentum fluxes. Physics of Fluids 23, 096602–096602–13.

Bjørnø, L., 2003. Features of underwater acoustics from aristotle to our time. Acoustical Physics 49, 24–30.

Bouruet-Aubertot, P., Koudella, C., Staquet, C., Winters, K., 2001. Particle dispersion and mixing induced by breaking internal gravity waves. Dynamics of Atmospheres and Oceans 33, 95–134.

Bouruet-Aubertot, P., Thorpe, S., 1999. Numerical experiments on internal gravity waves in an accelerating shear flow. Dynamics of Atmospheres and Oceans 29, 41–63.

Brandt, P., Alpers, W., Backhaus, J.O., 1996. Study of the generation and propagation of internal waves in the strait of gibraltar using a numerical model and synthetic aperture radar images of the european ERS 1 satellite. Journal of Geophysical Research: Oceans 101, 14237–14252.

Brekhovskikh, L.M., Lysanov, I.P., 2003. Fundamentals of ocean acoustics. Springer.

Brown, E., Colling, A., Phillips, J., Rothery, D., Wright, J., 2006. Waves, tides and shallow water processes. Butterworth-Heinemann, Oxford.

Chen, C.T., Millero, F.J., 1977. Speed of sound in seawater at high pressures. The Journal of the Acoustical Society of America 62, 1129–1135.

Chernetsky, A.S., Schuttelaars, H.M., Talke, S.A., 2010. The effect of tidal asymmetry and temporal settling lag on sediment trapping in tidal estuaries. Ocean Dynamics 60, 1219–1241.

Dalziel, S.B., 1991. Two-layer hydraulics: A functional approach. Journal of Fluid Mechanics 223, 135–163.

D'Asaro, E., Lien, R.C., Henyey, F., 2007. High-frequency internal waves on the oregon continental shelf. Journal of Physical Oceanography 37, 1956–1967.

Dean, R.G., Dalrymple, R.A., 2001. Coastal Processes with Engineering Applications. Cambridge University Press, Cambridge.

Schneider von Deimling, J., Weinrebe, W., Tóth, Z., Fossing, H., Endler, R., Rehder, G., Spieß, V., 2013. A low frequency multibeam assessment: Spatial mapping of shallow gas by enhanced penetration and angular response anomaly. Marine and Petroleum Geology 44, 217–222.

Demtröder, W., 2013. Experimentalphysik 1 - Mechanik und Wärme. 6 ed.

Eiff, O., Huteau, F., Tolu, J., 2005. High reynolds-number orographic wave-breaking experiments. Dynamics of Atmospheres and Oceans 40, 71–89.

Eisma, D., 1986. Flocculation and de-flocculation of suspended matter in estuaries. Netherlands Journal of Sea Research 20, 183–199.

Frigo, M., Johnson, S.G., 2005. The design and implementation of FFTW3. Proceedings of the IEEE 93, 216–231.

Gabioux, M., Vinzon, S., Paiva, A., 2005. Tidal propagation over fluid mud layers on the amazon shelf. Continental Shelf Research 25, 113–125.

Gerold, S., 1963. On the in situ measurement of temperature and electrical conductivity of sea-water. Deep Sea Research and Oceanographic Abstracts 10, 269–277.

Gordon, R., 1996. Acoustic Doppler Current Profiler - principal and operation - a practical primer. Technical Report. RD instruments. San Diego.

Gratiot, N., Mory, M., Auchère, D., 2000. An acoustic doppler velocimeter (ADV) for the characterisation of turbulence in concentrated fluid mud. Continental Shelf Research 20, 1551–1567.

Groeskamp, S., Nauw, J.J., Maas, L.R.M., 2011. Observations of estuarine circulation and solitary internal waves in a highly energetic tidal channel. Ocean Dynamics 61, 1767–1782.

Guan, W., Kot, S., Wolanski, E., 2005. 3-d fluid-mud dynamics in the jiaojiang estuary, china. Estuarine, Coastal and Shelf Science 65, 747–762.

Hamilton, E.L., 1970. Sound velocity and related properties of marine sediments, north pacific. Journal of Geophysical Research 75, PP. 4423–4446.

Harker, A.H., Temple, J.A.G., 1988. Velocity and attenuation of ultrasound in suspensions of particles in fluids. Journal of Physics D: Applied Physics 21, 1576–1588.

Hayter, E., Mehta, A., 1986. Modelling cohesive sediment transport in estuarial waters. Applied Mathematical Modelling 10, 294–303.

Held, P., Schrottke, K., Bartholomä, A., 2013. Generation and evolution of high-frequency internal waves in the ems estuary, germany. Journal of Sea Research 78, 25–35.

Hoitink, A., Hoekstra, P., 2005. Observations of suspended sediment from ADCP and OBS measurements in a mud-dominated environment. Coastal Engineering 52, 103–118.

Huang, L., Fang, H., Chen, M., 2012. Experiment on surface charge distribution of fine sediment. SCIENCE CHINA Technological Sciences 55, 1146–1152.

Huthnance, J.M., 1989. Internal tides and waves near the continental shelf edge. Geophysical & Astrophysical Fluid Dynamics 48, 81–106.

James J. Faran, J., 1951. Sound scattering by solid cylinders and spheres. The Journal of the Acoustical Society of America 23, 405–418.

Jan Kowalski, S., 2004. Ultrasonic waves in diluted and densified suspensions. Ultrasonics 43, 101–111.

Jens Jürgens, Norbert Winkel, 2003. Ein beitrag zur tidedynamik der unterems. Mitteilungsblatt der Bundesanstalt für Wasserbau 86, 29–31.

de Jonge, V., 1992. Tidal flow and residual flow in the ems estuary. Estuarine, Coastal and Shelf Science 34, 1–22.

de Jonge, V.N., 1983. Relations between annual dredging activities, suspended matter concentrations, and the development of the tidal regime in the ems estuary. Canadian Journal of Fisheries and Aquatic Sciences 40, 289–300.

Kantha, L.H., 1979. On generation of internal waves by turbulence in the mixed layer. Dynamics of Atmospheres and Oceans 3, 39–46.

Kineke, G.C., Sternberg, R.W., 1995. Distribution of fluid muds on the amazon continental shelf. Marine Geology 125, 193–233.

Kineke, G.C., Sternberg, R.W., Trowbridge, J.H., Geyer, W.R., 1996. Fluid-mud processes on the amazon continental shelf. Continental Shelf Research 16, 667–696.

Kirby, R., 1988. High concentration suspension (fluid mud) layers in estuaries, in: Vol. Physical Processes in Estuaries. Springer-Verlag, Berlin, pp. 463–487.

Kirby, R., 2013. Managing industrialised coastal fine sediment systems. Ocean & Coastal Management 79, 2–9.

Konyaev, K., Sabinin, K., Serebryany, A., 1995. Large-amplitude internal waves at the mascarene ridge in the indian ocean. Deep Sea Research Part I: Oceanographic Research Papers 42, 2075–2091.

Kozaczka, E., Grelowska, G., Kozaczka, S., 2009. Sounding of the seabed of the gulf of gdansk by the means of the parametric sonar, in: The Sixteenth International Congress on Sound and Vibration, Krakow.

Kranenburg, C., 1994. The fractal structure of cohesive sediment aggregates. Estuarine, Coastal and Shelf Science 39, 451–460.

de Kreeke, J.V., Day, C., Mulder, H., 1997. Tidal variations in suspended sediment concentration in the ems estuary: origin and resulting sediment flux. Journal of Sea Research 38, 1–16.

Kuhlmann, H.C., 2007. Strömungsmechanik. Pearson Studium, München [u.a.].

Langlois, V., Gautherin, W., Laurent, J., Royon, L., Fournaison, L., Delahaye, A., Jia, X., 2011. Ultrasonic determination of the particle concentration in model suspensions and ice slurry. International Journal of Refrigeration-Revue Internationale Du Froid 34, 1972–1979.

Lavery, A.C., Ross, T., 2007. Acoustic scattering from double-diffusive microstructure. The Journal of the Acoustical Society of America 122, 1449.

Le Menn, M., 2011. About uncertainties in practical salinity calculations. Ocean Sci. 7, 651–659.

LeBlond, P., 2002. Ocean waves: Half-a-century of discovery. Journal of Oceanography 58, 3–9.

van der Lee, W.T., 2000. Temporal variation of floc size and settling velocity in the dollard estuary. Continental Shelf Research 20, 1495–1511.

Leichter, J.J., Deane, G.B., Stokes, M.D., 2005. Spatial and temporal variability of internal wave forcing on a coral reef. Journal of Physical Oceanography 35, 1945–1962.

van Leussen, W., 1999. The variability of settling velocities of suspended fine-grained sediment in the ems estuary. Journal of Sea Research 41, 109–118.

van Leussen, W., 2011. Macroflocs, fine-grained sediment transports, and their longitudinal variations in the ems estuary. Ocean Dynamics 61, 387–401.

Lott, F., Kelder, H., Teitelbaum, H., 1992. A transition from Kelvin–Helmholtz instabilities to propagating wave instabilities. Physics of Fluids A: Fluid Dynamics 4, 1990–1997.

Maa, J.P.Y., Sun, K.J., He, Q., 1997. Ultrasonic characterization of marine sediments: a preliminary study. Marine Geology 141, 183–192.

Maa, P.Y., Mehta, A., 1987. Mud erosion by waves: a laboratory study. Continental Shelf Research 7, 1269–1284.

Manning, A., Dyer, K., 2007. Mass settling flux of fine sediments in northern european estuaries: Measurements and predictions. Marine Geology 245, 107–122.

Manning, A., Langston, W., Jonas, P., 2010. A review of sediment dynamics in the severn estuary: Influence of flocculation. Marine Pollution Bulletin 61, 37–51.

Maxeiner, E., Dalrymple, R.A., 2011. Experimental observation of standing interfacial waves induced by surface waves in muddy water. Physics of Fluids 23, 096603–096603–9.

McAnally, W.H., Teeter, A., Schoellhamer, D., Friedrichs, C., Hamilton, D., Hayter, E., Shrestha, P., Rodriguez, H., Sheremet, A., Kirby, R., 2007. Management of fluid mud in estuaries, bays, and lakes. II: measurement, modeling, and management. Journal of Hydraulic Engineering 133, 23–38.

McClements, D.J., Povey, M.J.W., 1989. Scattering of ultrasound by emulsions. Journal of Physics D: Applied Physics 22, 38.

Mehta, A.J., 1989. On estuarine cohesive sediment suspension behavior. Journal of Geophysical Research: Oceans 94, 14303–14314.

Mietta, F., Chassagne, C., Manning, A., Winterwerp, J., 2009. Influence of shear rate, organic matter content, pH and salinity on mud flocculation. Ocean Dynamics 59, 751–763.

Mikeš, D., 2011. A simple floc-growth function for natural flocs in estuaries. Mathematical Geosciences 43, 593–606.

Miles, J.W., 1957. On the generation of surface waves by shear flows. Journal of Fluid Mechanics 3, 185–204.

Miles, J.W., 1961. On the stability of heterogeneous shear flows. Journal of Fluid Mechanics 10, 496–508.

Millero, F., 2010. History of the equation of state of seawater. Oceanography 23, 18–33.

Millero, F.J., Feistel, R., Wright, D.G., McDougall, T.J., 2008. The composition of standard seawater and the definition of the reference-composition salinity scale. Deep Sea Research Part I: Oceanographic Research Papers 55, 50–72.

Mobley, J., Waters, K.R., Hall, C.S., Marsh, J.N., Hughes, M.S., Brandenburger, G.H., Miller, J.G., 1999. Measurements and predictions of the phase velocity and attenuation coefficient in suspensions of elastic microspheres. The Journal of the Acoustical Society of America 106, 652–659.

Nagashima, H., 1971. Reflection and breaking of internal waves on a sloping beach. Journal of the Oceanographical Society of Japan 27, 1–6.

Nakamura, T., Awaji, T., 2001. A growth mechansim for topographic internal waves generated by an oscillatroy flow. Journal of Physical Oceanography 31, 2511–2524.

Nastrom, G.D., Fritts, D.C., 1992. Sources of mesoscale variability of gravity waves. part i: Topographic excitation. Journal of the Atmospheric Sciences 49, 101–110.

New, A., Dyer, K., Lewis, R., 1987. Internal waves and intense mixing periods in a partially stratified estuary. Estuarine, Coastal and Shelf Science 24, 15–33.

New, A., Dyer, K., Lewis, R., et al., 1986. Predictions of the generation and propagation of internal waves and mixing in a partially stratified estuary. Estuarine, Coastal and Shelf Science 22, 199–214.

Oh, S.H., Mizutani, N., Suh, K.D., Hashimoto, N., 2005. Experimental investigation of breaking criteria of deepwater wind waves under strong wind action. Applied Ocean Research 27, 235–250.

Ott, J.A., 1996. Meereskunde: Einführung in die Geographie und Biologie der Ozeane ; 13 Tabellen. Ulmer.

Otten, E.W., 2008. Repetitorium Experimentalphysik. Springer.

Papenmeier, S., Schrottke, K., Bartholomä, A., 2014. Over time and space changing characteristics of estuarine suspended particles in the german weser and elbe estuaries. Journal of Sea Research 85, 104–115.

Papenmeier, S., Schrottke, K., Bartholomä, A., Flemming, B.W., 2012. Sedimentological and rheological properties of the Water–Solid bed interface in the weser and ems estuaries, north sea, germany: Implications for fluid mud classification. Journal of Coastal Research , 797–808.

Pawlowicz, R., 2010. A model for predicting changes in the electrical conductivity, practical salinity, and absolute salinity of seawater due to variations in relative chemical composition. Ocean Science 6, 361–378.

Pawlowicz, R., Wright, D.G., Millero, F.J., 2011. The effects of biogeochemical processes on oceanic conductivity/salinity/density relationships and the characterization of real seawater. Ocean Science 7, 363–387.

Penrose, J., Beer, T., 1981. Acoustic reflection from estuarine pycnoclines. Estuarine, Coastal and Shelf Science 12, 237–249.

Peregrine, D.H., 1983. Breaking waves on beaches. Annual Review of Fluid Mechanics 15, 149–178.

Pomar, L., Morsilli, M., Hallock, P., Bádenas, B., 2012. Internal waves, an underexplored source of turbulence events in the sedimentary record. Earth-Science Reviews 111, 56–81.

Prandle, D., 2009. Estuaries: Dynamics, Mixing, Sedimentation and Morphology. Cambridge University Press, Cambridge.

Rao, A., Babu, S., Prasad, K., Murty, T.R., Sadhuram, Y., Mahapatra, D., 2010. Investigation of the generation and propagation of low frequency internal waves: A case study for the east coast of india. Estuarine, Coastal and Shelf Science 88, 143–152.

Robb, G.B.N., Leighton, T.G., Dix, J.K., Best, A.I., Humphrey, V.H., White, P.R., 2006. Measuring bubble populations in gassy marine sediments: a review, in: Futures in Acoustics: Today's Research - Tomorrow's Careers. Proceedings of the Institute of Acoustics Spring Conference. 2006. Institute of Acoustics, St. Albans, UK, pp. 60–68.

Ross, M.A., Mehta, A.J., 1989. On the mechanics of lutoclines and fluid mud. Journal of Coastal Research , 51–62.

Ross, T., Lavery, A.C., 2012. Acoustic scattering from density and sound speed gradients: Modeling of oceanic pycnoclines. The Journal of the Acoustical Society of America 131, EL54.

Safak, I., Allison, M., Sheremet, A., 2013. Floc variability under changing turbulent stresses and sediment availability on a wave energetic muddy shelf. Continental Shelf Research 53, 1–10.

Schrottke, K., Becker, M., Bartholomä, A., Flemming, B.W., Hebbeln, D., 2006. Fluid mud dynamics in the weser estuary turbidity zone tracked by high-resolution side-scan sonar and parametric sub-bottom profiler. Geo-Marine Letters 26, 185–198.

Schuchardt, B., Scholle, J., Schulze, S., Bildstein, T., 2007. Vergleichende bewertung der ökologischen situation der inneren Ästuare von eider, elbe, weser und ems: Was hat sich nach 20 jahren verändert? Coastline Reports 9, 15–26.

Seim, H.E., 1999. Acoustic backscatter from salinity microstructure. Journal of Atmospheric and Oceanic Technology 16, 1491–1498.

Silva, J.C.B.d., Helfrich, K.R., 2008. Synthetic aperture radar observations of resonantly generated internal solitary waves at race point channel (cape cod). Journal of Geophysical Research 113, 17 PP.

Sottolichio, A., Hurther, D., Gratiot, N., Bretel, P., 2011. Acoustic turbulence measurements of near-bed suspended sediment dynamics in highly turbid waters of a macrotidal estuary. Continental Shelf Research 31, S36–S49.

Spingat, F., Oumeraci, H., 2000. Schwebstoffdynamik in der trübungszone des ems-Ästuars. Die Küste 62, 159–219.

Stöcker, H., 2000. Taschenbuch der Physik: Formeln, Tabellen, Übersichten. 4., korr. aufl. ed., Harri Deutsch.

Sutherland, B., Hughes, G., Dalziel, S., Linden, P., 2000. Internal waves revisited. Dynamics of Atmospheres and Oceans 31, 209–232.

Talke, S., de Swart, H., Schuttelaars, H., 2009. Feedback between residual circulations and sediment distribution in highly turbid estuaries: An analytical model. Continental Shelf Research 29, 119–135.

Talke, S.A., de Swart, H.E., 2006. Hydrodynamics and morphology in the Ems / Dollard estuary : review of models, measurements, scientific literature and the effects of changing conditions. Technical Report. Institute for Marine and Atmospheric Research Utrecht, University of Utrecht, The Netherlands. Utrecht.

Tanaka, M., 1983. The stability of steep gravity waves. Journal of the Physical Society of Japan 52, 3047–3055.

Temkin, S., 1992. Sound speeds in suspensions in thermodynamic equilibrium. Physics of Fluids A: Fluid Dynamics 4, 2399–2409.

Temkin, S., 1998. Sound propagation in dilute suspensions of rigid particles. The Journal of the Acoustical Society of America 103, 838–849.

Thill, A., Moustier, S., Garnier, J.M., Estournel, C., Naudin, J.J., Bottero, J.Y., 2001. Evolution of particle size and concentration in the rhône river mixing zone:: influence of salt flocculation. Continental Shelf Research , 2127–2140.

Traykovski, P., Geyer, W., Irish, J., Lynch, J., 2000. The role of wave-induced density-driven fluid mud flows for cross-shelf transport on the eel river continental shelf. Continental Shelf Research 20, 2113–2140.

UNESCO, 1981. The practical salinity scale 1978 and the international equation of state of seawater 1980. Technical Papers in Marine Science 36, 25 pp.

Urgeles, R., Cattaneo, A., Puig, P., Liquete, C., Mol, B., Amblàs, D., Sultan, N., Trincardi, F., 2011. A review of undulated sediment features on mediterranean prodeltas: distinguishing sediment transport structures from sediment deformation. Marine Geophysical Research 32, 49–69.

Vilibić, I., Dadić, V., Mihanović, H., 2004. Large-amplitude internal kelvin waves trapped off split (middle adriatic sea). Estuarine, Coastal and Shelf Science 61, 623–630.

Vsemirnova, E.A., Hobbs, R.W., Hosegood, P., 2012. Mapping turbidity layers using seismic oceanography methods. Ocean Science 8, 11–18.

Wang, D.P., 2006. Tidally generated internal waves in partially mixed estuaries. Continental Shelf Research 26, 1469–1480.

Waterman, P.C., Truell, R., 1961. Multiple scattering of waves. Journal of Mathematical Physics 2, 512–537.

Wilkens, R., Richardson, M., 1998. The influence of gas bubbles on sediment acoustic properties: in situ, laboratory, and theoretical results from eckernförde bay, baltic sea. Continental Shelf Research 18, 1859–1892.

Wood, A.B., 1941. A textbook of sound; being an account of the physics of vibrations with special reference to recent theoretical and technical development. G. Bell and sons, ltd., London.

Wunderlich, J., Müller, S., 2003. High-resolution sub-bottom profiling using parametric acoustics. International Ocean Systems 7, 6–11.

Wunderlich, J., Wendt, G., Müller, S., 2005. High-resolution echo-sounding and detection of embedded archaeological objects with nonlinear sub-bottom profilers. Marine Geophysical Researches 26, 123–133.

Wurpts, R., 2005. 15 years experience with fluid mud: Definition of the nautical bottom with rheological parameters. Terra et Aqua 99, 22–32.